Insights into the solar wind conditions near Mars from data science techniques

Sofija Elanis Durward, MPhys

Department of Physics, Faculty of Science and Technology

Lancaster University

A thesis submitted for the degree of

Doctor of Philosophy

November, 2023

Declaration

I declare that the work presented in this thesis is, to the best of my knowledge and belief, original and my own work. The material has not been submitted, either in whole or in part, for a degree at this, or any other university. This thesis does not exceed the maximum permitted word length of 80,000 words including appendices and footnotes, but excluding the bibliography.

Sofija Elanis Durward

Insights into the solar wind conditions near Mars from data science techniques

Sofija Elanis Durward, MPhys.
Department of Physics, Faculty of Science and Technology, Lancaster University
A thesis submitted for the degree of *Doctor of Philosophy*. November, 2023

Abstract

Mars' plasma environment is strongly driven by its interaction with the solar wind, however the lack of an upstream solar wind monitor at Mars sometimes necessitates assumptions about the variability of solar wind and interplanetary magnetic field (IMF) conditions. This thesis investigates the variability in the solar wind. The first study finds the IMF to be notably steadier in field strength, clock angle and cone angle direction during the Mars Global Surveyor (MGS) mission than the Mars Atmosphere and Volatile Evolution (MAVEN) mission. Additionally, the variability of the field strength, clock angle and cone angle were all found to be dependant on the cone angle of the measurements, with periods of IMF oriented close to the ecliptic plane being considerably steadier than periods of IMF oriented approximately perpendicular to it. The second study presents a data-driven model to predict the upstream solar wind conditions for periods where MAVEN was inside the martian magnetosphere. The predictions of this model are compared with those from a solar wind propagation model commonly used at Mars, and the model presented in this thesis was found to better capture the velocity of the solar wind during periods of more variable solar wind. The final study of this thesis investigates orientation preferences in the interplanetary magnetic field (IMF) using clustering techniques to group IMF measurements by field strength and stability of the cone angle. It finds that periods of low strength and steady orientation are typically aligned in one of two orientations which correspond to 'towards' and 'away' sectors of the IMF. During periods of higher field strength, the cone angles are constrained out of the ecliptic plane.

Acknowledgements

I owe much thanks to my supervisors Jim and Sarah. Thank you for regularly dealing with my chaos and always being kind, calm and supportive.

Thank you to my wife Kim for being a source of joy during the most difficult period of my life.

Thank you also to my sister Annie, who has been understanding, patient, open and honest with me since we met.

I dedicate this thesis to the memory of my father, Andrew John Durward. The world is a bleaker place without you.

Contents

List of Figures

List of Tables

Chapter 1

Introduction

Of all of the known planets both within and outside of the solar system, Mars is one of the most unique. Frequent impacts from comets and asteroids produce an unusual planetary surface with two distinct regions. The southern hemisphere of Mars is heavily cratered and the surface is comprised of a range of rock types that have been revealed by impacts. The northern hemisphere however is much smoother and mainly made of the igneous rocks such as basalt and andesite that were likely deposited by lava flows during early periods in the planet's history (Carr & Head, 2010). Governed by its compact size, the planet's once molten core cooled much faster than that of Earth, and as such the strength of the intrinsic magnetic field associated with the electric current created by motion in the liquid core gradually decreased until today when it is accepted that Mars has no intrinsic magnetic field.

This chapter covers an introduction to the solar wind including sources of variability, the martian magnetic environment, the ionosphere and neutral atmosphere of Mars and a brief overview of past, current and future Mars missions.

1.1 The solar wind

The solar wind consists of the particles that leave the Sun's corona and move out into the solar system. Since the introduction of the solar wind theory in 1958 (Parker, 1958), it has long been accepted that the solar corona is hot enough to overcome the Sun's

gravity and escape into the solar system. As the particles from the Sun's atmosphere spread out into interplanetary space, they drag with them the solar magnetic field as the magnetic flux is 'frozen in' to the plasma. This expansion of the coronal magnetic field into the solar system is known as the interplanetary magnetic field (IMF).

Initially, the solar wind was thought to propagate only radially through the solar system, however recently it has been shown that there is a tangential flow of the solar wind (Němeček et al., 2020) during both low speed (300-400 km/s) and moderate speed (400-600 km/s) flow.

The solar wind encounters multiple obstacles within the solar system. Planets, comets and moons disrupt the flow of the plasma, producing a bow shock as the supersonic flow is abruptly stopped. Magnetospheres and thick atmospheres are impenetrable to the solar wind, producing magnetospheric and ionospheric obstacles to the solar wind flow. Mars is an ionospheric obstacle due to the lack of a global intrinsic magnetic field at the planet.

1.1.1 Ambient solar wind and transient solar events

During 'typical' solar conditions, the plasma that emanates from the Sun forms the ambient solar wind. Three distinct regimes of ambient solar wind exist; the fast (with speeds of 600-800 km/s), the slow (with speeds of 300-500 km/s) and streamers (Neugebauer & Snyder, 1966). Solar wind streamers occur at points of reversal of the IMF. Corotating interaction regions (CIRs) are the interaction between an earlier slow solar wind stream and a later fast solar wind stream (Heber et al., 1999).

Transient events disrupt the ambient solar wind flow. Unlike ambient solar wind which emanates from closed field structures within the Sun, energetic events are associated with either solar flares or coronal holes (Intriligator, 1980). Examples of transient events include solar flares, erupting solar prominences and interplanetary coronal mass ejections (ICMEs). ICMEs are energetic events which are made of expelled magnetic flux ropes from the Sun's corona. They often have a shockwave, sheath region and

ejecta region. Those with flux rope magnetic structures are dubbed 'magnetic clouds' (Burlaga et al., 2001).

As the Sun goes through a regular 22 year shift of its magnetic poles, the structure of the solar magnetic field changes also from a well ordered field with clear positive regions of outwards and inwards magnetic field, to times where the field is more erratic. During these periods of disordered solar magnetic field there is an increased occurrence of energetic solar wind streams which include coronal mass ejections.

1.1.2 Variability in the solar wind

Although our understanding of solar wind variability is not comprehensive, there are multiple sources that are well understood. Known periodicities in the solar wind are the result of the solar cycle and solar rotation as well as plasma oscillations, producing regular variations in the solar wind that range in timescale from minutes to tens of years. Changes in the uniformity of the Sun's magnetic field as a result of the solar dynamo produce the solar cycle; a 22 year change in the solar environment and consequently the solar wind. On longer timescales still, variations have been noted in the solar cycle activity, with later cycles tending to have higher maximum (the secular trend (Hathaway et al., 2002; Wilson, 1988)) and odd numbered cycles tending to have higher maximum sunspot numbers than the even cycles directly before them (Gnevyshev-Ohl rule (Gnevyshev & Ohl, 1948)). Shorter term variability in the solar output includes an 154 day periodicity that occurs near the solar cycle maximum (Ballester et al., 2002; Lean, 1990) and a variation with a timescale of around two years. This periodicity is most noticeable around solar maximum; producing double peaks in the sunspot number. The Sun's open magnetic flux and global magnetic field also show signs of quasi-periodicities of about 1.3 years (Ulrich & Tran, 2013; Wang & N. R. Sheeley, 2003). These are caused by the emergence of active regions, which take approximately a year to decay due to restraints from differential rotation, meridional flow, and supergranule diffusion. Additionally, the wind speed, field strength and density oscillate as the Parker spiral sectors change. At the boundary between two sectors, the solar wind speed decreases and the density and IMF strength increase.

Sudden changes in solar wind properties such as field strength, density and dynamic pressure can be the result of shocks, plasma boundary layers or discontinuities. Expected events that would cause a change in IMF conditions at Mars are the crossing of the current sheet as well as corotating interaction regions (CIRs) and interplanetary coronal mass ejections (ICMEs).

Beyond variability in the solar wind that originates at the Sun, there will also be differences in the solar wind as it moves through the solar system. It is expected that CIRs will be more prevalent at Mars than at Earth due to the increased opportunity for fast solar wind streams to catch up to slower streams of material emitted from the Sun at an earlier time. Additionally, interplanetary coronal mass ejections (ICMEs) evolve in all three dimensions between 1 and 1.5 AU so that their signatures are different from terrestrial observations.

1.1.3 Qualities of the solar wind near Mars

Previous studies of the solar wind near Mars have provided an important insight into the average solar wind conditions upstream of Mars. The IMF strength has been estimated to be between 2.5nT and 3nT and the median direction of the IMF in the x-y plane was found to be 52 degrees (Brain et al., 2003).

Study	Parameter	MPV	Mean	Median	Standard Deviation
Brain et al. (2003)	IMF strength	2.5-3 nT	-	-	-
Marquette et al. (2018)	IMF strength	-	3.486 nT	3.02 3nT	1.865 nT
Marquette et al. (2018)	IMF clock angle	-	162.3	129.7	100.7
Marquette et al. (2018)	IMF cone angle	-	94.33	93.35	33.99
Marquette et al. (2018)	SW dynamic pressure	-	0.9055 nPa	0.7059 nPa	0.7115 nPa
Marquette et al. (2018)	SW density	-	3.343 cm-3	2.418 cm-3	2.928 cm-3
Marquette et al. (2018)	SW speed	-	419.5 km/s	403.6 km/s	79.9 km/s
Liu et al. (2021)	IMF strength	1.87 nT	-	-	-
Liu et al. (2021)	IMF clock angle	89.6, 207.8	-	-	-
Liu et al. (2021)	IMF cone angle	115.9, 310.2	-	-	-
Liu et al. (2021)	SW dynamic pressure	0.39 nPa	-	-	-
Liu et al. (2021)	SW density	1.4 cm-3	-	-	-
Liu et al. (2021)	SW speed	368.9 km/s	-	-	-

Table 1.1: Summary of measurements of the solar wind properties upstream of Mars. MPV = most probable value

1.2 Mars and its magnetosphere

Early in the planet's history, the hot core of Mars exuded a strong dipole magnetic field. 4.1 billion years ago (Carr & Head, 2010) the field began to dissipate as the planet cooled, and today the remaining dipole field is negligibly weak. However, the planet does have a magnetic environment which can be split into two sections: an induced magnetosphere caused as the interplanetary magnetic field bends around the planet as it flows away from the Sun; and localised magnetic fields caused by magnetic material in the planet's crust.

1.2.0.1 Crustal magnetic fields

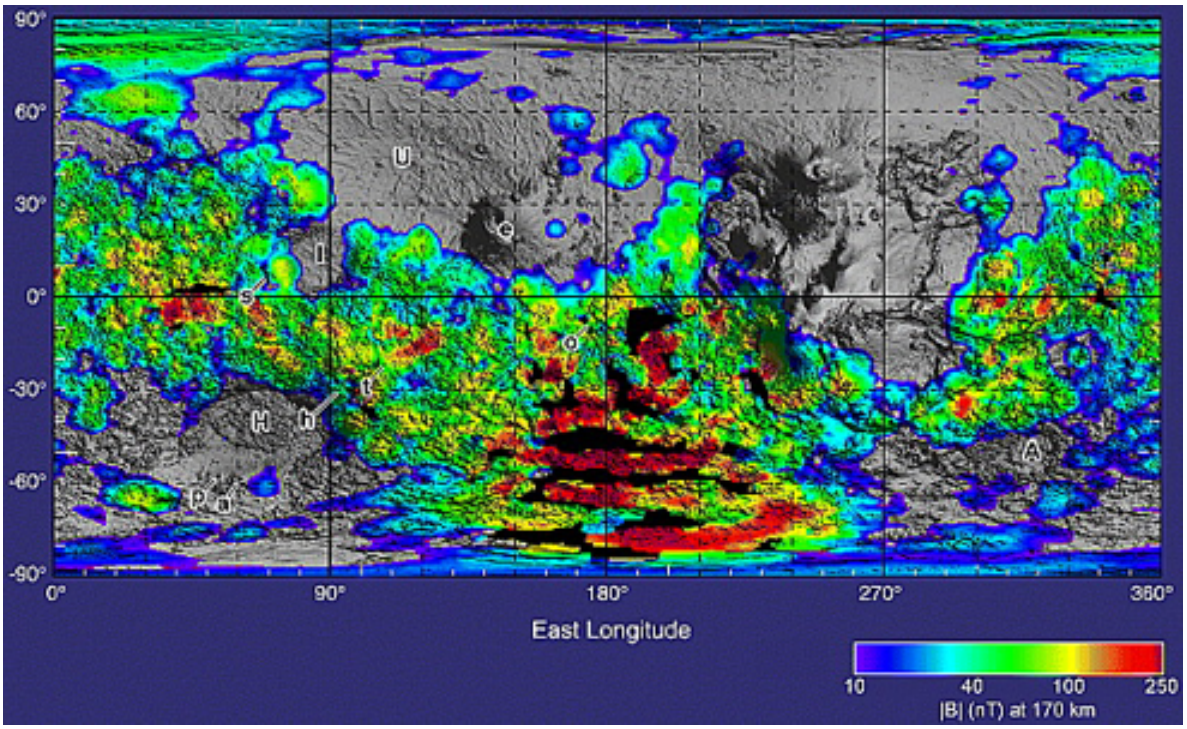

Figure 1.1: A map of the martian crustal field strength at 170 km altitude made using data from the Mars Global Surveyor magnetometer and electron reflectometer data (Mitchell et al., 2007). The letters on the map denote the Utopia (U), Hellas (H), Argyre (A), and Isidis (I) impact basins, and the volcanoes Elysium (e), Syrtis Major (Nili and Meroe) (s), Apollinaris (o), Tyrrhena (t), Hadriaca (h), Peneus (p), and Amphitrites (a).

Pockets of the Martian crust contain magnetic material that produces areas of high magnetic field strength that act as an obstacle to solar wind flow. These crustal magnetic fields are much stronger than the magnetic fields associated with the induced magnetosphere (around 200nT compared to $20 - 50$nT). It is thought that these magnetised areas of crust may have been formed by a process called thermoremanent magnetisation, which can occur when a material cools below its Curie temperature within a magnetic field (Connerney et al., 1999). This process magnetised the material in the crust as it cooled in the presence of the intrinsic magnetic field, with the degree of magnetisation depending upon the composition of the crust. The crustal fields are located almost exclusively in the planet's southern hemisphere (as seen in Figure 1.1), and are located less than 10 km under the planet's surface. Also, these field regions are regularly arranged in bands stretching along the planet from east to west. The distribution of the magnetic material is thought to be due to the planet's past tectonic activity (Connerney et al., 2015; Zuber, 2001), with in situ measurements putting the field strength at up to 150 nT at 400 km altitude (Connerney et al., 1999).

Because of the high altitude to which the crustal fields permeate, the magnetic pressure in these areas is much higher which makes the standoff distance, at which the dynamic pressure of the solar wind and the magnetic pressure of the planet balance, at a much higher altitude than in areas where the crustal fields are not present (Krymskii et al., 2003). This causes a magnetic obstacle to the solar wind, which differs as the planet rotates. However, these magnetic fields also disrupt ionospheric layers. Inside the closed crustal field lines, sometimes known as 'mini magnetospheres,' (Krymskii et al., 2003) there are increased electron temperatures which have been suggested to be due to the existence of trapped high energy photoelectrons. Around the closed field lines of the crustal fields are cusp regions, into which electrons precipitate causing excitation, emission and ionisation of the planetary plasma (Shane et al., 2016). This process can cause discrete aurora on the nightside of Mars that trace the locations of the crustal fields.

1.2.0.2 The induced magnetosphere

The induced magnetosphere refers to the magnetic characteristics that are caused by the solar wind interaction. As the IMF permeates through the solar system, it interacts with the planets. For bodies like Earth with an intrinsic magnetic field, the interplanetary magnetic field lines interact with the field lines at the object's magnetopause through a process called magnetic reconnection. Field lines from the magnetosphere are broken open and connect with lines from the interplanetary magnetic field. These lines that connect the sun to the planet then move through the planetary magnetosphere in a convection-like process governed by the Dungey cycle, and then reconnect on the night side of the planet and continue traveling through the solar system. However, for planets without an intrinsic magnetic field the process is quite different. The ionosphere and exosphere of Mars act as an obstacle around which the solar wind bends, creating areas of magnetic field pileup (Dubinin et al., 2006) which is separated from the low field strength magnetopause area by a thin, sharp boundary (Bertucci et al., 2005). The solar wind is stopped when it nears Mars at the point where the thermal pressure of the atmosphere equals the dynamic pressure of the wind, which creates a magnetosheath. Because the solar wind travels at supersonic speeds, this process also creates a separate bowshock upstream of the magnetosheath.

The main features of the induced Martian magnetosphere are the bowshock, the magnetosheath, the magnetic pile up boundary (also called the induced magnetospheric boundary or magnetopause), the magnetotail and the plasma sheet.

The bowshock is the outermost plasma boundary within the planetary magnetosphere. The bowshock occurs because the solar wind plasma is traveling supersonically, causing a curved shape around the dayside of the magnetosphere. This phenomena is observed at every planet in the solar system. The shape of the bow shock depends on the velocity of the solar wind, with faster wind bringing the bowshock closer to the planet's surface. The bowshock also contains very high numbers of planetary ions, which are thought to be ionised as the outermost part of the Martian exosphere undergoes impact ionisation while interacting with the solar wind plasma.

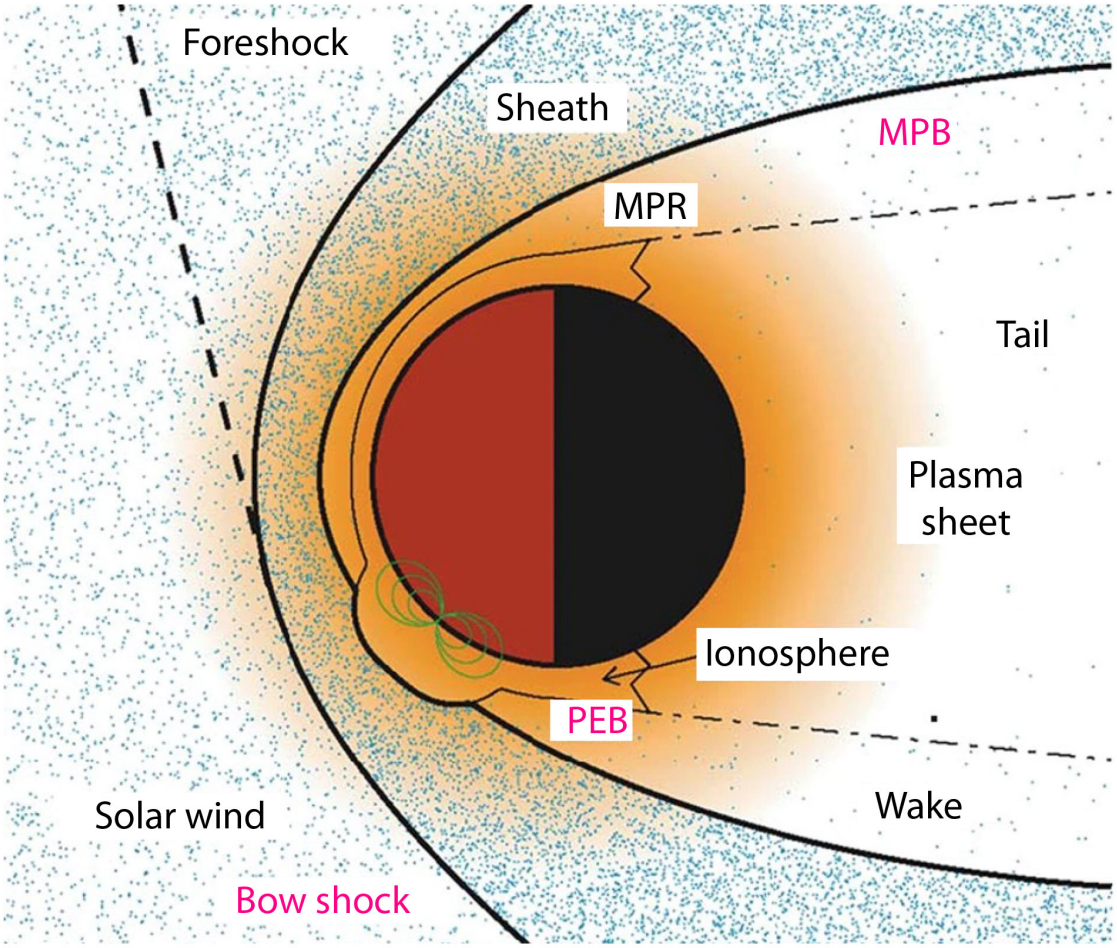

Figure 1.2: A schematic of the martian magnetosphere taken from (K. Liu et al., 2020). MPB = magnetic pileup boundary, MPR = magnetic pileup region, PEB = photoelectron boundary.

The magnetosheath is the area behind the bow shock. This cavity within the magnetosphere contains very low magnetic field strengths. The solar wind plasma in this section of the magnetosphere has been heated as it was shocked and is turbulent with little clear structure. However, because the region is thin (just under the gyroradius of a proton in the solar wind), there is not enough space for all the material in the region to reach thermal equilibrium through particle interactions. As such, there is a temperature gradient where the outermost shocked edge is hottest. At Mars, the exosphere extends into the magnetosheath region, which allows heavy ions from the

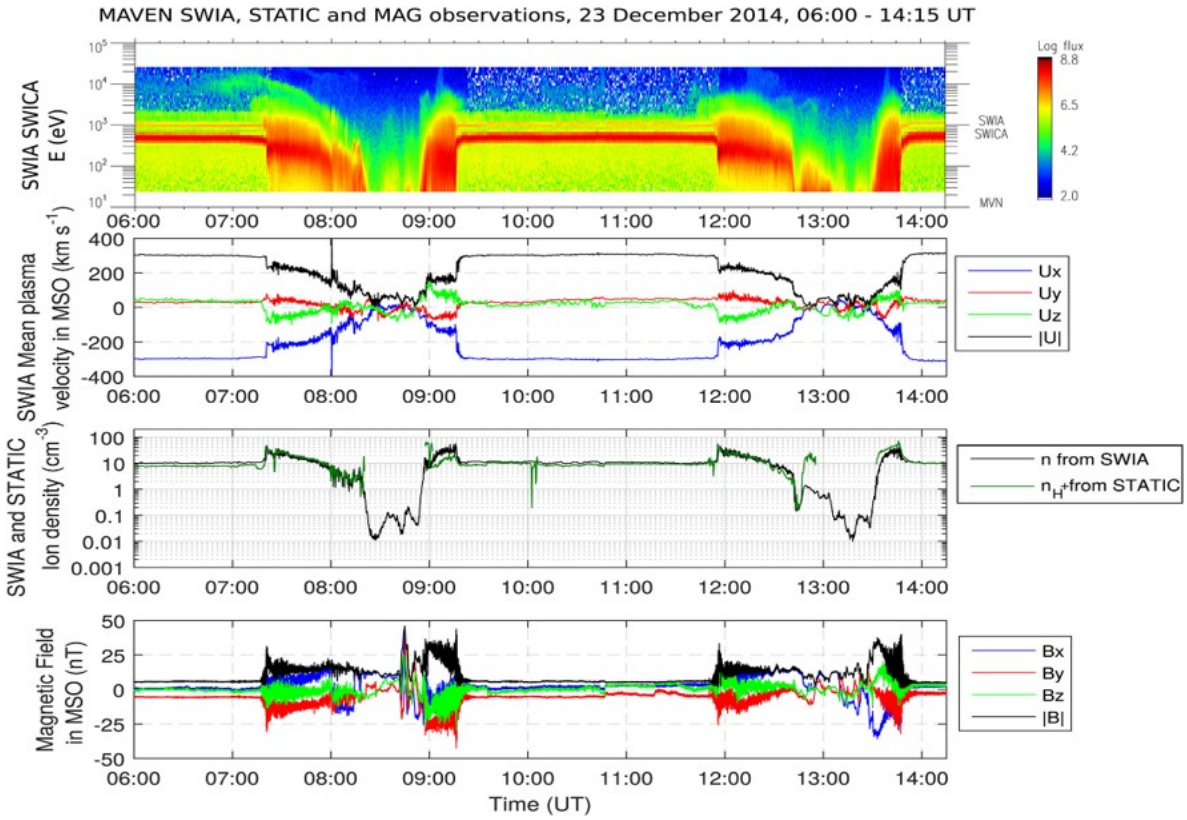

Figure 1.3: Data from the MAVEN spacecraft showing measurements both within the martian magnetosphere and out in the solar wind. Taken from (Romanelli et al., 2018).

planet's ionosphere to mix with the solar wind electrons and change their movements. The plasma in this region can be modelled as two interacting fluids: a proton fluid and a planetary heavy ion fluid. The interaction between the two fluids can create electric fields within the medium as the two types of ion move with different inertia due to their different masses. Bi-ion waves within the plasma can lead to the formation of 'shocklets', small shock waves inside the original shockwave. The heavy ions also limit the movement of protons and ions from the solar wind down towards Mars' surface.

The magnetic pileup boundary (MPB) separates the magnetosheath and the magnetic pile up regions (Acuna et al., 1998). This boundary is also known as the induced magnetospheric boundary or IMB, as this is the boundary below which there are sharply decreased suprathermal electron fluxes (Bertucci et al., 2003; Nagy et al., 2004). The

stark difference between the very low magnetic field strength within the magnetosheath and the high field within the magnetic pile up regions allows for clear identification of the boundary (Bertucci et al., 2005), which is typically found at an altitude of 600-1000km at the subsolar point (Brain et al., 2005). However, the boundary is typically found at a higher altitude in the southern hemisphere because of the higher magnetic pressure in the regions of crustal magnetic fields. It is not currently thought that the position of the boundary is dependent on the phase of the solar cycle (Vignes et al., 2000).

Due to the draping of the field lines around the magnetic obstacles of the planet, the pile up structured regions are characterised by very high magnetic field strengths(Bertucci et al., 2004). On the dayside, the lower boundary of the ionosphere is dependent on the solar wind conditions (Nagy et al., 2004). On the nightside, the pile up region is bounded by the magnetotail.

The magnetotail is the region of Mars' magnetosphere downstream of the planet, where nightside reconnection occurs. This region has been well explored by spacecraft such as the Mars Global Surveyor and Mars Express. The radius of the Martian tail is 2-2.5 times the radius of Mars (J. Luhmann et al., 1991). In the magnetotail, a current sheet separates the regions of differing magnetic field orientation. It is within this current sheet that acceleration of auroral particles occurs. Because of the high rate of magnetic reconnection events in this region, observations of the magnetotail show the acceleration of ions back towards the planet (Harada et al., 2017).

1.2.1 Mars' ionosphere and atmosphere

The composition of the Martian atmosphere is much more similar to Venus than it is to the terrestrial atmosphere. Although the composition of the atmosphere varies seasonally, on average the make up of the atmosphere is 95% carbon dioxide, 2.6% nitrogen, 2% argon, 0.16% oxygen and 0.06% carbon monoxide (Connerney et al., 2015; Trainer et al., 2019). As with the ionosphere, the density of atoms within the neutral atmosphere varies depending on the latitude, longitude and solar zenith angle.

The thermosphere is one of the most active regions of the neutral atmosphere, with the temperature and composition being strongly dependent on the solar radiation and solar wind conditions (Bougher et al., 2015). Additionally, the thermosphere is affected by the exosphere above and the low and middle atmosphere below. Mars Global Surveyor and Mars Odyssey spacecraft have both observed local mass density variations that are caused by tidal waves in the lower atmosphere propagating up into the thermosphere. Gravity waves thought to originate in the lower atmosphere have also been detected by the Mars Odyssey spacecraft in the lower altitudes of the thermosphere (Parish et al., 2009). Additionally, MAVEN detected gravity waves with vertical wavelengths between 10 km and 30 km on the dayside of Mars, with increasing amplitudes for larger solar zenith angles (Siddlea et al., 2019).

Most of the particles that are removed from the Martian atmosphere do so via processes that occur in the thermosphere and exosphere. Within the thermosphere, interactions between N and NO produce odd nitrogen which can more easily escape from the Martian atmosphere (Fox, 1993). The most important mechanism for the production of nitrogen atoms is disassociative recombination reactions, but this process also occurs for a significant amount of oxygen and carbon also. Neutrals may also leave through a process known as 'sputtering escape,' where charged particles from the solar wind or energetic ionospheric particles can directly impact with neutral species in the thermosphere and impart enough energy onto them that the neutral can reach the escape velocity and leave the atmosphere.

The Martian exosphere is composed mainly of a neutral oxygen corona that extends from 200 km far out above the planet's surface. Because of the large size of the exosphere, it overlaps with many areas that are involved with the Martian magnetic environment and affects the dynamics of these regions. The exosphere and thermosphere are the regions most affected by the interaction with the solar wind, and the number density of oxygen and carbon dioxide within the exosphere is thought to be significantly less today than it was in the ancient atmosphere, when the extreme ultraviolet radiation flux from the Sun was much higher (M. Zhang et al., 1993).

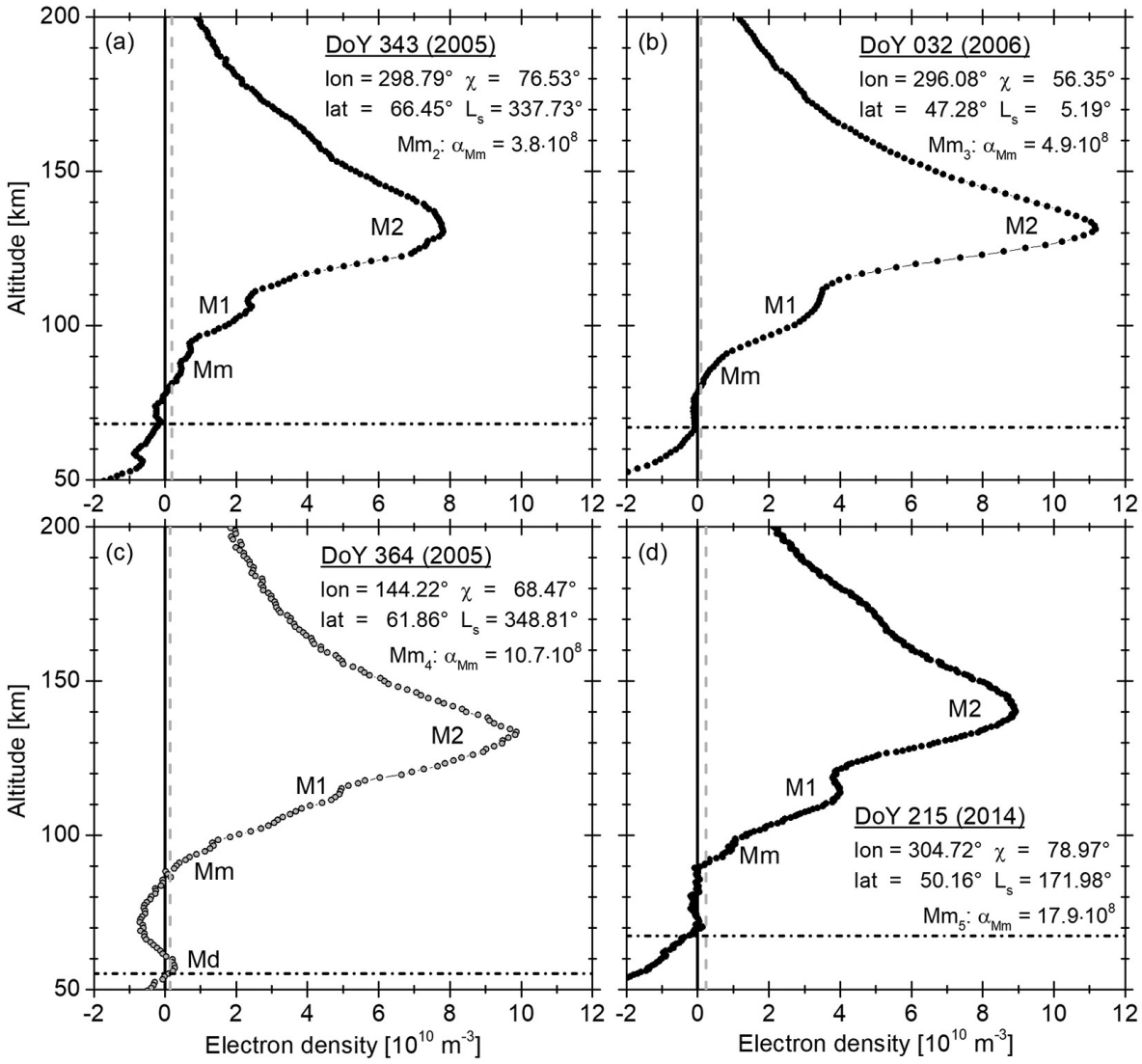

Figure 1.4: Diagram of Mars dayside electron density profiles from the Mars Radio Science experiment onboard Mars Express. Taken from Peter et al., 2021.

Like at Earth, many of Mars' ionospheric layers are well modelled as Chapman layers (i.e. characterised by a population of a single type of ion created by one particular wavelength of radiation and destroyed only by recombination). Mars has three dayside and three nightside layers.

The three dayside layers of the Marian ionosphere are the M1 and M2 layers and a

third ablation layer, as shown if Figure 1.4. The M1 and M2 layers are driven by photochemical reactions from x-ray and extreme ultraviolet radiation (Withers, 2009). In both the M1 and M2 layers 0_2^+ is the most common ion species, and is produced by the interaction of oxygen atoms with ionised carbon dioxide. Recently, it has been suggested that the movement of ions due to solar wind flow and diffusion of ions into different ionospheric layers may be the dominant processes in the M2 layer (Bougher et al., 2001).

The third dayside layer is situated at an altitude of 65-110km, much lower than the M1 and M2 layers (at 110km and 135km respectively). It is caused by the ablation of meteorites within the Martian atmosphere, and as such is densely populated with heavy, metallic, ionised atoms (Patzold et al., 2005). In particular, these layers contain high densities of ionised iron and magnesium, which are provided by the meteorites as gaseous atoms and then ionised via charge exchange. This third layer is not always present in the ionosphere, and was only seen in around 8% of the ion density profiles taken by the Mars Explorer spacecraft. Currently, it is not known what drivers cause the layer to appear.

The first detailed observations of Mars' nightside ionosphere were made in 2014 by the MAVEN spacecraft. In general, the density of charged species is much lower on the nightside of Mars (Kopf et al., 2017), however the nightside ionosphere does consist of three distinct layers found at approximately 70 km, 100 km and 130 km in altitude. The three nightside layers are associated with energetic particles from the solar wind, ions evaporated from the surface of meteorites and transport within the Martian atmosphere. O_2^+ and NO^+ are the most common ion at altitudes above and below 130km respectively (Girazian et al., 2017). Radar measurements of the ionosphere suggest that the nightside structure is very fragmented and non-uniform. Unlike the dayside ionosphere, which is structured in regular layers, the nightside ionsophere seems to have holes, bands and other more complex features (Gurnett et al., 2008). The most notable features are bulges in the ionospheric layers caused by strong radial magnetic fields originating from crustal sources.

1.2.2 Ionospheric losses

Due to its lack of intrinsic magnetic field, Mars' exosphere interacts directly with the solar wind through a variety of mechanisms. Ionisation of the exosphere through charge exchange, electron impact and solar radiation produces charged particles that are quickly picked up by the solar wind.

Once the ionisation has occurred, the presence of the ionised martian plasma within the changing IMF generates a strong electric field that facilitates ion outflow. Plumes of ions have been modelled escaping into the solar wind after being directed through the magnetosheath before being deflected into the solar wind (Brecht & Ledvina, 2006; Cloutier et al., 1974; Curry et al., 2015; Dong et al., 2015; Fang et al., 2008; Jarvinen et al., 2016; J. G. Luhmann & Schwingenschuh, 1990; Najib et al., 2011). Additionally, bulk loss of plasma from the martian ionosphere can occur when crustal fields are stretched by the solar wind and undergo magnetic reconnection to detach from the planet (Brain et al., 2010).

Oxygen is one of the atmospheric components for which solar wind interaction has significantly decreased its abundance in the martian atmosphere. As the oxygen is predominantly ionised by solar extreme ultraviolet (EUV) radiation, there is a strong seasonal dependence of the oxygen ion outflow as the EUV strength changes (Dong et al., 2017). As O^+, O_2^+ and CO_2^+ ions have gyroradii close to the radius of Mars, these ions are easily taken into the solar wind via ion pickup. In the energy range of 30 to 30000 eV/C, Mars Express (MEX) measured that approximately 4g of O^+ atoms, 8g of O_2^+ ions and 6g of CO_2^+ ions are lost to the solar wind on average every second (roughly 300 kg/day, 700kg/day and 500kg/day respectively) (Barabash et al., 2007). The deposition of lighter solar wind ions such as H^+ into the martian atmosphere and pickup of heavier planetary ions such as O^+, O_2^+ and CO_2^+ disrupts the flow of the solar wind downstream of the planet as the solar wind is suddenly slowed because of the heavier atoms in a process known as mass loading. The process of mass loading is also observed at other induced magnetospheres within the solar system including at mercury and passing comets (Benna et al., 2010; Huddleston et al., 1990; Volwerk et al., 2016).

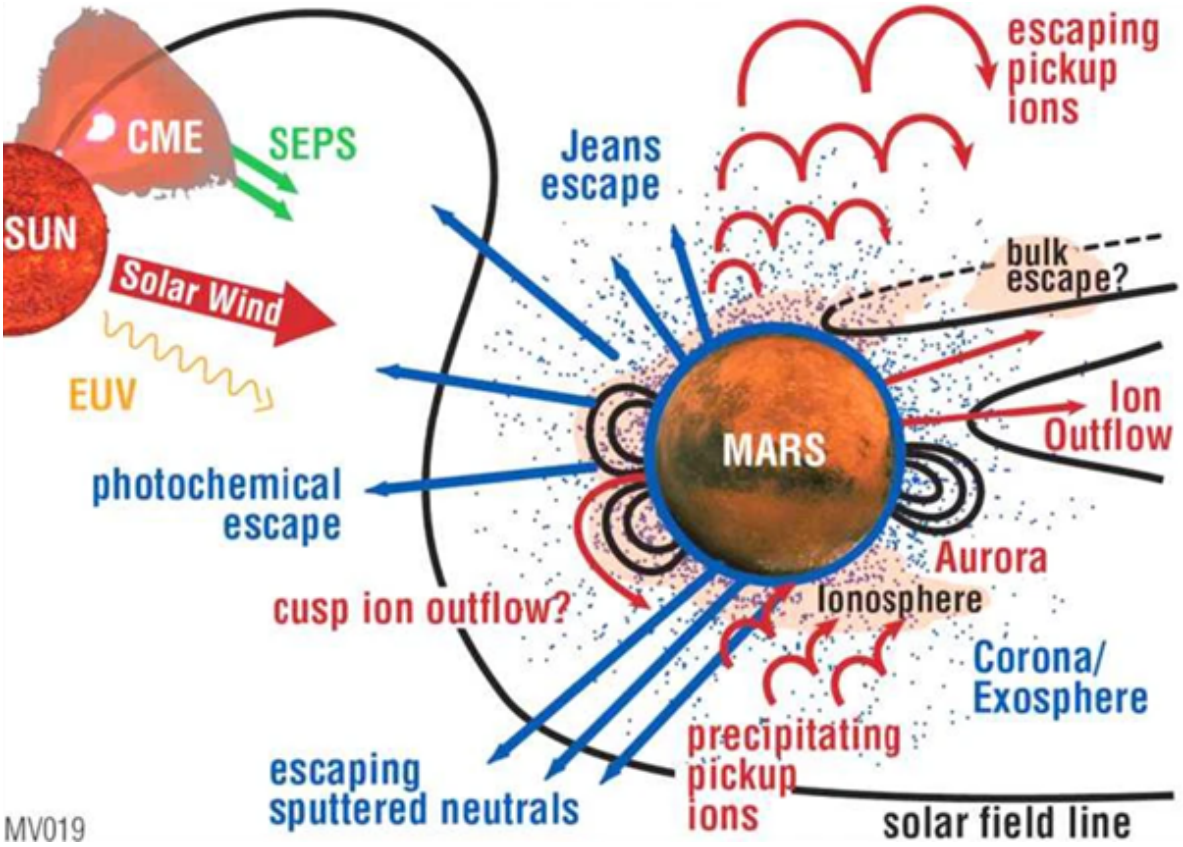

Figure 1.5: Schematic of loss mechanisms for ions and neutral atoms at Mars (Dandouras et al., 2020). Plasma processes are shown in red text, and escaping neutral processes are shown in blue text.

1.3 A brief history of Mars missions

Over the years, many probes and rovers have been sent to take measurements of the Martian environment. Recent developments have seen high quality observations of many aspects of the Martian planet and the surrounding space environment. Most notably, measurements of the magnetic field taken from underneath the planet's ionosphere by the Mars Global Surveyor revealed the existence of strong crustal fields. To date, 49 spacecraft have been launched towards Mars, but only 35 have been successful in achieving their missions.

The table below gives a brief overview of all of the spacecraft that have reached Mars.

More in depth information is provided on Mars Global Surveyor and Mars Atmosphere and Volatile EvolutioN, as data from these spacecraft were used in this thesis.

The space agency acronyms and names used in Tables 1.2 and 1.3 are defined below:

NASA = National Aeronautics and Space Administartion
SSP = Soviet Space Program
ROSCOSMOS = Russian State Space Corporation
JAXA = Japan Aerospace Exploration Agency
ESA = European Space Agency
ISRO = Indian Space Research Organisation
UAESA = United Arab Emirates Space Agency
CNSA = Chinese National Space Agency.

FIRST MARS PHOTO IS TRANSMITTED; MARINER SIGNALS INDICATE PLANET LACKS A LIQUID CORE LIKE EARTH'S

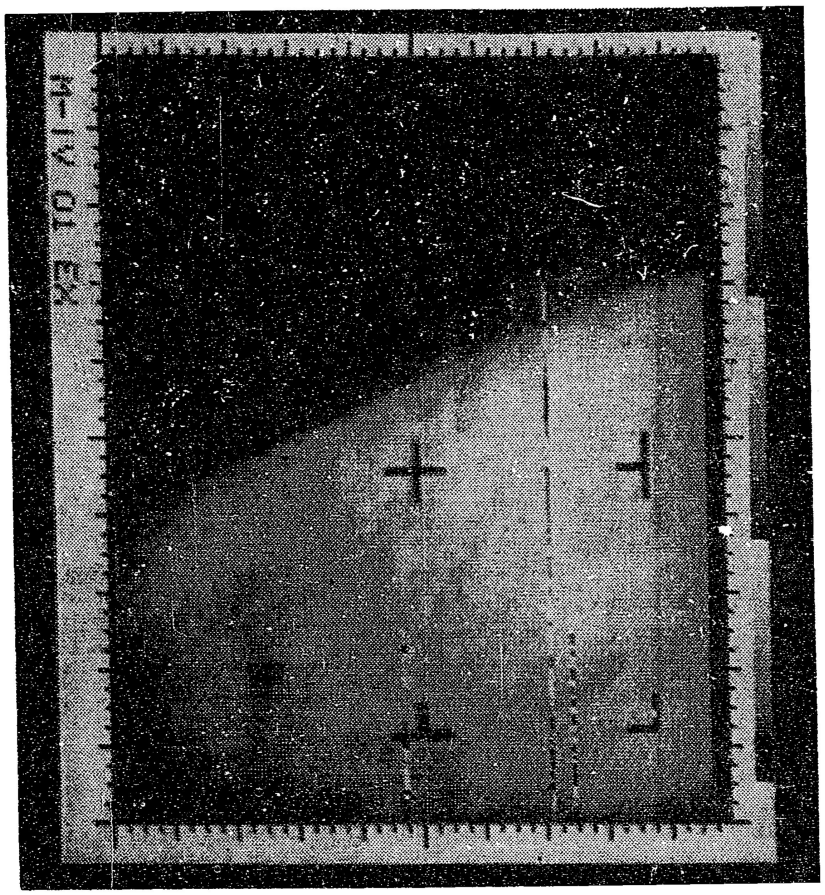

United Press International Telephoto

FIRST CLOSE-UP OF MARS: Photograph made by Mariner 4 of the planet and sent back to earth. The area covered along edge of planet is about 200 miles. Shot was taken at about 10,500 miles. It is expected to add greatly to scientists' knowledge of Mars.

OTHER DATA SENT

Sensors Find Scant Radiation Belt and Thin Atmosphere

By WALTER SULLIVAN
Special to The New York Times

PASADENA, July 15—Mariner 4 has sent to earth the first close-up photograph of Mars.

The picture, transmitted today in an eight-hour broadcast over a distance of 134 million miles, shows the "limb," or rounded edge of Mars, including a vast, desert-like region.

It does not show any of the controversial canals. But this is not necessarily significant, since the view is extremely oblique and covers a region under the noonday sun. Such lighting makes for little contrast.

The picture, the first ever taken of another planet at close range, covers a region between the areas of Mars known as Cebrenia, Arcadia and Amazonis.

Part of the second picture, which should overlap the first, has already been transmitted to earth and it is possible that as many as 22 pictures of the planet will be delivered in the next 10 days.

Figure 1.6: The first photograph of Mars taken from space. Taken by NASA's Mariner IV spacecraft on its flyby and shown here in an article from the front page of the New York Times on 16th July 1965 (Sullivan, 1965). Even from this first in situ measurement, it is beginning to become clear that the magnetic environment (and therefore the atmosphere and ionosphere) at Mars is much more different from Earth than previously thought.

Name	Space Agency	Launch date	Key achievements
Mariner 4	NASA	28 November 1964	First in situ image of Mars (see Fig. 1.6)
Mariner 6	NASA	25 February 1969	-
Mariner 7	NASA	27 March 1969	First in situ image of Phobos
Mars 3	SSP	28 May 1971	-
Mariner 9	NASA	30 May 1971	First artificial satellite of Mars
Mars 4	SSP	21 July 1973	First successful non-American mission
Mars 5	SSP	25 July 1973	-
Mars 6	SSP	5 August 1973	First direct measurements of Mars' atmospheric temperature and pressure
Mars 7	SSP	9 August 1973	-
Viking 1	NASA	20 August 1975	First probe to land on Mars
Viking 2	NASA	9 September 1975	First complete map of martian surface
Phobos 2	SSP	12 July 1988	-
Mars Observer	NASA	25 September 1992	Communications failed before reaching Mars orbit
Mars Global Surveyor	NASA	7 November 1996	See section 1.3.1 below
Mars 96	ROSCOSMOS	16 November 1996	Failed to leave Earth's orbit
Mars Pathfinder	NASA	4 December 1996	First wheeled vehicle on any other planet
Nozomi	JAXA	3 July 1998	Lost contact after Mars flyby
Mars Climate Orbiter	NASA	11 December 1998	Failed shortly after reaching Mars
Mars Polar Lander	NASA	3 January 1999	Communication lost after reaching Mars
Mars Odyssey	NASA	7 April 2001	Found evidence of ice below martian surface
Mars Express	ESA	2 June 2003	Included the failed Beagle 2 lander and the Mars Express orbiter, which made the first detection of a third ionospheric layer
Spirit Rover	NASA	10 June 2003	-
Opportunity Rover	NASA	8 July 2003	-

Table 1.2: Summary of Mars missions 1964-2004.

Name	Space Agency	Launch date	Key achievements
Mars Reconnaissance Orbiter	NASA	12 August 2005	Found evidence suggest liquid water flowed on Mars 2-2.5 billion years ago
Phoenix Lander	NASA	4 August 2007	-
Fobos-Grunt/Yinghuo-1	ROSCOSMOS/CNSA	26 November 2011	Failed to leave Earth's orbit
Mars Science Laboratory	NASA	26 November 2011	-
Mars Orbiter	ISRO	5 November 2013	-
MAVEN	NASA	18 November 2013	See section 1.3.2 below
ExoMars 2016	ESA	14 March 2016	Contained both the the trace gas orbiter and the failed Schiaparelli lander
InSight	NASA	15 May 2018	-
Hope Orbiter	UAESA	19 July 2020	-
Tianwen-1	CNSA	23 July 2020	Included the Tianwen-1 orbiter, lander and cameras as well as the Zhurong rover
Mars 2020	NASA	30 July 2020	Included the most recent Mars rover, Perseverance, as well as the Ingenuity helicopter which completed the first flight on another planet

Table 1.3: Summary of Mars missions 2005-Present.

1.3.1 Mars Global Surveyor

The Mars Global Surveyor is the longest running Mars mission in history. Operating for more than four times the planned period (Greicius, 2015), the mission was split into two phases: the aerobraking (AB) phase and the mapping phase. The AB phase in the initial part of the mission aimed to change the orbit of the spacecraft from an elliptical orbit to a close circular orbit via the process of aerobraking. The resistance that the spacecraft experienced whilst it dipped into Mars' atmosphere reduced its speed and caused the apoapsis of the spacecraft's orbit to decrease. This made the orbit more circular. This phase also allowed for scientific measurements to be made outside of the Martian magnetosphere, including measurements of the solar wind (Brain et al., 2003). The mapping phase provided high quality images of the planet's surface.

The Mars Global Surveyor spacecraft had five scientific instruments onboard: a magnetometer and electron reflectometer (MAG-ER), the Mars Orbiter Camera (MOC), the Mars Orbiter Laser Altimeter (MOLA) (Smith et al., 2001), The Thermal Emission Spectrometer (TES) (Christensen et al., 2001) and radio science (RS).

The mapping phase was where the main aim of the mission took place: high quality detailed mapping of the Martian surface. This phase did also allow for measurements at lower altitudes of approximately 100km, including the first measurements of the magnetic field from below the planet's ionosphere by the Magnetometer-Electron Reflectometer instrument (Mitchell et al., 2001). Measurements from the magnetometer provided a comprehensive survey of the vector magnetic field at altitudes between 108km and 120km (Acuna et al., 1998), which led to the discovery and detailed mapping of the crustal magnetic fields discussed in Section 1.2.0.1. However, these measurements were not precise enough to definitively rule out the possibility of a global dipole field of strength $\approx 2 \times 10^{17}\mathrm{Am}^{-3}$ or below (Acuna et al., 2001).

Other than the magnetometer-electron reflectometer the spacecraft was also equipped with a thermal emission spectrometer (which calculates the chemical composition of the Martian surface using images in the infrared and near infrared), a laser altimeter (which uses laser pulses to calculate the altitude of surface features), an ultrastable oscillator

(which takes measurements of the Doppler shift) and a camera, as well as a signal relay for communication with the Mars Exploration rovers Spirit and Opportunity.

1.3.2 Mars Atmosphere and Volatile EvolutioN (MAVEN)

MAVEN is a current NASA mission aiming to better explain the changing climate of Mars (Jakosky et al., 2015). It is expected that the measurements from this satellite will lead to a better understanding of the nightside ionosphere and of the planet's interaction with the solar wind. Instruments onboard the orbiter are categorised into three packages. The 'Particles & Field' package includes solar wind electron and ion analysers (Halekas et al., 2015; Mitchell et al., 2016), the SupraThermal And Thermal Ion Composition (STATIC) experiment (McFadden et al., 2015), the solar Energetic Particle (SEP) experiment (Larson et al., 2015), the Langmuir Probe and Waves (LPW) experiment (Andersson et al., 2015) and a magnetometer (Connerney et al., 2015). The remote sensing package contains an imaging ultraviolet spectrometer (McClintock et al., 2015), and the final package contains the Neutral Gas and Ion Mass Spectrometer (NGIMS) (Mahaffy, Benna, King, et al., 2015).

Already MAVEN has provided insight into the planet's thermosphere (Mahaffy, Benna, Elrod, et al., 2015; Stone et al., 2018), ionosphere (Benna et al., 2015; Girazian et al., 2017), magnetosphere and solar wind interaction (Halekas, Brain, et al., 2017) and rates of neutral (Chaffin et al., 2018; Lillis et al., 2017; Rahmati et al., 2018) and ion atmospheric escape (Dubinin et al., 2018; Dubinin et al., 2017). From SWIA's direct measurements of solar wind upstream of Mars, interaction with the solar wind was shown to be dependent on solar wind conditions and seasonal (Halekas, Ruhunusiri, et al., 2017). Additionally, the occurrence of proton cyclotron waves upstream of Mars has been found to vary temporally (Romanelli et al., 2016). With regards to atmospheric loss, escape rates of oxygen atom were found to scale linearly with solar activity (Cravens et al., 2017). Following form this work, escape rates of hot atomic oxygen due to disassociative recombination were modelled using in situ measurements of the ion densities and temperatures (Lillis et al., 2017). The escape rates of heavy ions have also been modelled and the total heavy ion escape rate was calculated to be 1.2×10^{25} ions/s, consistent with MAVEN measurements (Ledvina et al., 2017). Dong

et al. (2017) used MAVEN data to investigate ion escape rates in the magnetotail and plume, and found that the total ion escape rate is highly sensitive to the solar EUV flux.

1.4 Plasmas

Much of the material in the Sun is in the form of ionised gas, or plasma. There are three criteria that a material must show if it is to be considered a plasma: the plasma frequency must be considerably higher than the collision frequency between charged and neutral particle species; the physical size of the gas must be much larger than the typical shielding distance or Debye length; and the number of particles with a spherical volume with the radius of the Debye length must be large (Bittencourt, 2004). Due to the high temperatures and relatively large number density of particles within the Sun these criteria are easily met.

In a homogenous plasma, electrons and ions that form atoms become completely disassociated even though the total plasma is charge neutral. Plasmas behave in a grouped way because of the electromagnetic forces that the particles in the plasma exert on each other, and these type of forces are referred to as 'self-consistent'. The main parameter that determines the dynamics of a plasma is the plasma beta. This is a parameter that describes the relative strengths of the magnetic pressure and thermal pressure within a plasma and is defined as

$$\beta = \frac{nk_BT}{(\frac{B^2}{2\mu_0})} \tag{1.1}$$

where n is the number density of particles within the plasma, k_B is the Boltzmann constant, T is the temperature, B is the magnetic field strength and μ_0 is the permeability of free space. In low plasma beta regimes, where $\beta \ll 1$, the plasma can be considered to be near collisionless and its motion is governed by the magnetic field (Boldyrev et al., 2021). For plasmas where $\beta > 1$ the thermal pressure is higher than the magnetic pressure so the plasma will expand.

1.4.1 Magnetohydrodynamics & Modelling Solar System Plasmas

Space plasmas can be modelled using magnetohydrodynamics (MHD). These are modified equations of electromagnetism that account for the fluid nature of the plasma by taking into consideration the resistivity and compressibility of the medium, and that on average every particle in the plasma will have the same motion.

$$\frac{d\mathbf{B}}{dt} = \nabla \times (\mathbf{V} \times \mathbf{B}) + \frac{\eta}{\mu_0}\nabla^2\mathbf{B} \tag{1.2}$$

The equation above defines the magnetic flux of a plasma using magnetohydrodynamics for a plasma with constant resistivity, V is the velocity of the plasma, η is the resistivity of the plasma and $\frac{dB}{dt}$ is the magnetic flux. The $\nabla \times (\mathrm{V} \times \mathrm{B})$ term describes how the magnetic flux is carried by the plasma, and the $\frac{\eta}{\mu_0}\nabla^2 B$ term describes the diffusion of the magnetic field through the plasma as it resists the plasma's motion. The relation between these two terms is a useful parameter in determining the nature of the plasma-magnetic field interaction which is known as the magnetic Reynolds number S.

$$S = \frac{\nabla \times (\mathbf{V} \times \mathbf{B})}{\frac{\eta}{\mu_0}\nabla^2\mathbf{B}} \tag{1.3}$$

For a plasma with magnetic Reynolds number much larger than one, as is the case with space plasmas, the plasma convection dominates and the magnetic field can be considered 'frozen in' to the plasma. For a plasma with magnetic Reynolds number much smaller than one, the diffusion of the field through the plasma is the dominating process and the frozen in flow model is a poor approximation. Because of the large scales in the solar system, most plasmas have a large magnetic Reynolds number and so can be thought to have magnetic flux frozen into them. Through this behaviour, the Sun's interplanetary magnetic field is carried through the solar system by the solar wind plasma as it moves outwards from the Sun, and the particles within the plasma gyrate around their associated field line with gyroradius and gyrofrequency

$$r_g = \frac{mv_\perp}{qB} \tag{1.4}$$

$$\Omega_g = \frac{qB}{m} \tag{1.5}$$

where r_g is the gyroradius, Ω_g is the gyrofrequency, m and q are the mass and charge of the particle, $v_\perp$ is the velocity of the particle perpendicular to the magnetic field line and B is the magnetic field strength. At Mars, ions with larger gyroradii can be lost more easily as they are picked up by the solar wind. For example, an O_2^+ ion in a 10 nT magnetic field with a perpendicular velocity of 50 kms^{-1} would have a gyroradius of approximately 1700 km (Kallio & Barabash, 2012). Comparitively, a H^+ ion with the same perpendicular velocity in the same magnetic field would have a gyrroadius of approximately 50km. As the O_2^+ ion has a much larger gyroradius, it would be picked up into the solar wind much more easily.

1.4.2 Plasma wave modes

One of the most interesting features of plasmas is the large number of wave modes that they support. In a vacuum, only electromagnetic wave modes are supported, however within even relatively sparse plasmas such as the solar wind, a variety of other pressure and magnetic waves can propagate because of the compressible and magnetic nature of the fluid.

Within a magnetised, compressible fluid, one type of wave mode is Alfven waves. These are waves that propagate with a velocity

$$v_A = \sqrt{\frac{B^2}{\mu_0 \rho}} \tag{1.6}$$

where v_A is the Alfven velocity, B is the magnetic field strength and ρ is the mass density of the plasma (Bittencourt, 2004). The waves travel through the plasma without causing any density or field strength fluctuations. The particles in the fluid feel a magnetic tensile force towards the field line, and so the field lines oscillate due to this pressure in a direction perpendicular to the plasma propagation direction. Because Alfven waves do not cause any density changes or changes in magnetic field strength, they are called

'incompressible' waves.

Finally, magnetoacoustic waves can propagate through a plasma also. The plasma particles can sustain pressure waves, which can move through the plasma in the direction that the medium was propagating. Unlike the Alfven waves, magnetoacoustic waves are compressible and can result in a changing magnetic field strength.

Chapter 2

Instruments and methodology

This chapter covers the basics of some of the methods that are used throughout this thesis. It contains an introduction to time series analysis as well as the fundamentals of machine learning. Additionally it provides an overview of the scientific instruments onboard MAVEN, MGS, Geotail, IMP-8, Wind and ACE that were used for the research in this thesis.

2.1 Time series analysis

Time series analysis techniques are an essential part of gaining insight from spacecraft data. The (mostly) continuous measurements from onboard instruments provide an insight into the variability of the environments they sample. This analysis can be very straightforward for series that are stationary (i.e. with no net movement up or down) with regular time steps between points. However in reality it is rare to receive data of this kind in space physics settings. Every measurement device, be it terrestrial or out in the solar system, will inevitably have a period where it is not in operation and taking measurements. Also, some spacecraft will not take measurements for a long enough period of time that the time series will be stationary. For example, the far ultraviolet (FUV) flux from our Sun varies during the solar cycle. If a spacecraft were to measure only 5 years of FUV flux data, then this time series would be non-stationary as the trend of the series would be upwards or downwards, depending on what part of the solar cycle was measured.

Techniques for analysis on non stationary and/or incomplete time series exist in many forms. The choice of autocorrelation functions for the first study in this thesis was made as it provides information on any periodicities within the time series data as well showing any decay in the autocorrelation (Box et al., 2015). This method is ideal for investigating the timescale of variability within the solar wind, and with small adjustments can be suitable for time series that are inconsistent like those from orbiting spacecraft.

Forecasting a time series involves predicting future values based on a good model of previous measurements (i.e. one that captures the general trend of the time series as well as the seasonality). Common methods for forecasting include autoregression, exponential smoothing, moving average techniques and neural networks. In the next section I will discuss my choice to use a neural network model for forecasting of solar wind conditions.

2.2 Machine learning

Machine learning (ML) is is a branch of artificial intelligence (AI) wherein programs can infer the best choices for a model based on patterns within the data they are given (LeCun et al., 2015). The theory of machine learning (also known as statistical learning) was introduced in the late 1950s (Abramson et al., 1963; Friedberg, 1958; Samuel, 1959), but due to recent advances in computing power these methods are now more practical to apply to data analysis problems.

Machine learning models are already well established in everyday life, being used for recommendation systems (Song et al., 2011), speech recognition (Ganapathiraju et al., 2004), fraud detection (Bartoletti et al., 2018; Puh & Brkic, 2019), stock market predictions (Huang et al., 2005), image classification (Krizhevsky et al., 2017), medical diagnostics (Cruz & Wishart, 2006; Wernick et al., 2010), traffic forecasting (Kumar, 2020), natural disaster predictions (Choi et al., 2019; Choubin et al., 2019; Kwon et al., 2008) and many other fields. In space and astrophysics research, machine

learning has been applied to a variety of problems including space weather forecasting (Nishizuka et al., 2021), identifying exoplanets (Shallue & Vanderburg, 2018), and mapping spectral features in Saturn's gas clouds (Waldmann & Griffith, 2019). Multiple chapters within this thesis will detail research applying machine learning methods to datasets from Mars missions to shed light on the solar wind conditions at Mars, and so this section will cover a brief introduction to types of machine learning and discuss the advantages and disadvantages of this approach.

2.2.1 What types of machine learning models are there?

Today, there are an ever growing number of machine learning algorithms which are available to use. In general, these algorithms can be sorted into types based on either the type of data that they are used with (labelled or unlabelled) or the type of output they produce (classification or regression). Of course there are models that do not fit well into any of the groups, or that take characteristics of multiple groups and combine them, but in general these groups define the types of machine learning models fairly well.

Supervised algorithms require a set of training data which has already been assessed by a person and has been labelled. From this the machine can learn the relationship between the input variables and the output variable. On the other hand, unsupervised models use the unlabelled data alone to make their estimates. An example of unsupervised learning is the clustering used in Chapter 5. This technique sorts data into groups based only on the distribution of the data points. These models use the distribution of data within the feature space to identify trends and groups. A fusion of the two known as semi-supervised learning includes elements of both kinds, using both labelled and unlabelled data for its predictions.

Reinforcement learning is a facet of machine learning wherein an agent must be able to learn from its previous experience (Sutton & Barto, 2018). In this situation, like in unsupervised learning, there is no labelled data from which the agent can base its choices. However reinforcement learning differs form unsupervised learning in that whereas unsupervised learning aims to find the structure within a data set,

reinforcement learning aims to maximise a specific reward function.

2.2.2 Neural networks, deep learning & transfer learning

Of all of the methods of machine learning used today perhaps the most well known is the neural network; a machine learning model that is comprised of layers of nodes that are connected in a way similar to that of neurons in the brain. They consist of an input layer, an output layer and any number of layers in between. The more layers between the input and output, the more the original data has been abstracted and so the more complex the patterns that the model is capable of learning. Each node in a network consists of a function which is applied to the input values taken from the previous layer, along with weights for each parameter that are also unique to each node. The output of the function is a single value, which is passed into the activation function. After this the output of the activation function will determine which of the nodes of the next layer receive the data from this node. In the training process a set of training data is used to adjust the weights of each nodes to produce the most accurate results. To determine which outputs are the most accurate, a loss function is used to quantify the difference between the predicted outputs and the known data labels. The aim is to minimise the loss function, but gradients in the loss function are used to update the model weights with the hope of improving the output. In the testing phase, the chosen weights are used with new data to produce predictions. One of the reasons that neural networks are so frequently used for machine learning problems is that they are very customisable and can be applied to a large number of different problems. Both categorisation and regression problems can be tackled using neural networks, which will produce outputs of different kinds.

One glaring problem when applying machine learning algorithms to large data sets is the need for feature extraction and engineering to guarantee successful application. Feature extraction requires significant time to allow for tweaking and tinkering by hand, which is obviously not practical when working with large amounts of data (LeCun et al., 2015). A solution to this problem is implementing deep learning techniques; a category of neural networks that use multiple levels of abstraction to detect higher level features

within the data. These methods have a structure that is similar to the brain (Goldberg & Holland, 1988), and can be more suitable when using complex data sets with a high number of features.

An example of where deep learning is useful is in image classification. First level features of an image are the pixel values. The first level image features are the presence or absence of edges at specific locations in the image. The second level can detect small repeated patterns of edges within the image. At higher levels, larger patterns of edges that can be at bigger differences in the images can be detected. In theory, networks with higher levels of abstraction can be applied to less carefully curated data sets, which is preferable when there are large numbers of images such that formatting them all manually would take a considerable amount of time.

Another use of neural networks is for a method known as transfer learning, where the model is trained on one data set and then used on a separate, similar data set. This method is successful as it uses knowledge learned from the previous domain and applies it to a new related domain (Ye & Dai, 2018). These methods have been used to forecast the electric load on the power grid (Jung et al., 2020) and to forecast traffic (Kumar, 2020).

2.2.3 Choosing a machine learning model

Although high accuracy is of course a key factor of a suitable model, other characteristics that may help when choosing an appropriate ML algorithm may include interpretability, computational cost and generalisation (Ahmed et al., 2010). If you would like to apply your model to multiple datasets, then you may value a very general model. Additionally, if your model will be used for a situation where knowing the way in which the model makes its choice is important (for example, if you are using a model for diagnosing illnesses) then interpretability would be a crucial factor of your model and you may choose a self-explaining model or one with fewer layers of abstraction.

2.2.4 Criticisms of machine learning

With the rise in use of ML techniques to a range of problems there has also been an increase in the number of criticisms of this approach, both for academic research and broader social applications. Many have denounced the use of ML for a variety of reasons both due to the very nature of the models and their application to less than ideal datasets as a quick fix or substitute for human decision making.

Many novice ML practitioners have a tendency to overfit the model to the training data if they use only the training accuracy as the measure of determining the correct model. Overfitting a model sacrifices its suitability to be used on dataets other than the training data set in lieu of high accuracy in the training data set. Obviously, this is not ideal.

Many researchers are skeptical of the use of ML techniques due to their lack of transparency. These are 'black box' methods; it is impossible to tell exactly why the model produces the answers that it does. However, there are some ways to improve this with the use of more 'interpretable' models. Many of these methods are more applicable to categorisation problems than regression, and should be implemented at the beginning of the use of ML techniques; there is little to be done to illuminate the reasons behind a model's predictions after it has already been trained and fitted.

Recently there have been many examples of ML techniques applied in important social situations where the training dataset has not been representative of the population on which the model will be used, leading to a data bias. One practical example of this is outlined in an article in the Harvard Business Review (Gentile et al., 2022) that details the issues an american day care center had with a newly installed security system based on facial recognition technology. The system regularly classified women with darker skin tones as intruders as it failed to match their faces to the images kept on file. This system was test mainly on pale skinned men, and as such it exhibited a bias towards people who looked like the images it had been trained on. In a similar way, we cannot expect a solar wind model to predict accurately conditions during periods which are notably different from the periods it has been trained on.

2.3 Instruments

2.3.1 Mars Global Surveyor MAG/ER

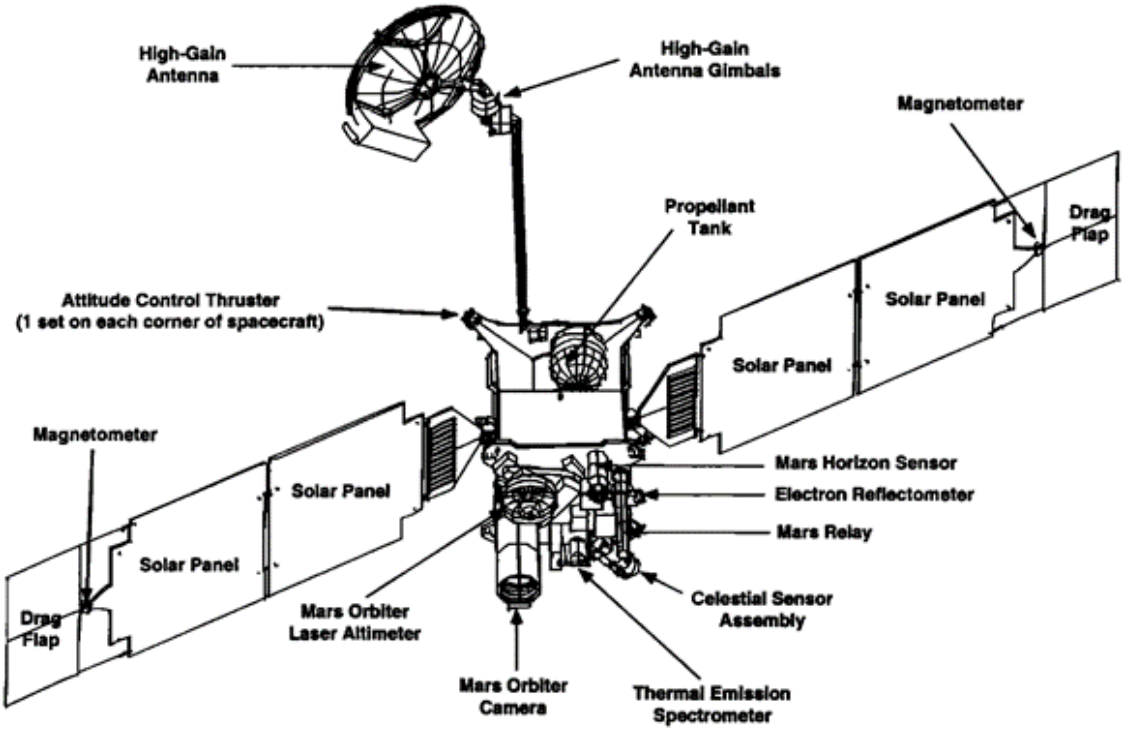

Figure 2.1: A schematic of the MGS spacecraft taken from (Albee et al., 2001).

The Mars Global Surveyor (MGS) spacecraft was launched on 7 November 1996, and arrived at the planet on 11 September 1997 (Albee et al., 1998). With a primary aim of mapping the complete surface of Mars for the first time, MGS mapped the magnetic field of Mars from its mapping orbit showing the crustal field magnetic structures embedded in the planet's crust (Acuna et al., 2001).

The electron reflectometer instrument measures the energy and angular distribution of electrons originating from both the solar wind plasma and the Martian atmosphere.

The instrument also includes two magnetometers which are affixed to the edges of the spacecraft's solar panels (as shown in Figure 2.1) to limit interference from the magnetic fields of the spacecraft's own instruments. The electron reflectometer utilises the magnetic mirror effect; an observable effect where particles are reflected in areas of strengthening magnetic field (Mitchell et al., 2001), and measures the ratio of the strength of the magnetic field at the altitude the electrons are absorbed at compared to that of the spacecraft.

The three-axis fluxgate magnetometer measures vector magnetic fields using a set of three cores that can be easily magnetised, each set up perpendicular to the other two and wrapped in two coiled wires. In each of the set ups the core is saturated with a magnetic field that varies with time sinusoidally. In the presence of an external magnetic field produces an output current on the surrounding wire that differs from the input current. The wire wrapped around the magnetometer detects the second harmonic of the core as this can be used to derive the magnetic field direction and amplitude (C. Zhang et al., 2020). The magnetometer onboard MGS provided the first map of the martian crustal magnetic fields (Mitchell et al., 2007). Additionally it took measurements of the solar wind during its aerobraking phase, during which the spacecraft dipped in and out of Mars' magnetosphere in its highly elliptical orbit (Brain, 2007).

2.3.2 MAVEN scientific instruments

The Mars Atmosphere and Volatile EvolutioN (MAVEN) spacecraft was launched on 18 November 2013 from Cape Canaveral.

Data used in this thesis came from two scientific instruments onboard MAVEN: the solar wind ion analyser (SWIA) (Halekas et al., 2015), and magnetometer (Connerney et al., 2015). Like MGS, the magnetometers onboard MAVEN are tri-axial fluxgate magnetometers and provide vector measurements of the magnetic field within and near the martian magnetosphere with a resolution of 0.008 nT (Connerney et al., 2015).

The MAVEN SWIA instrument (Halekas et al., 2015) includes a toroidal electrostatic analyser with electrostatic reflectors. The instrument has an angular resolution of 22.5

by 22.5 degrees for its entire field of view (a total of 360 by 90 degrees) and a much finer 4.5 by 3.75 degrees angular resolution for an area of 45 by 45 degrees close to the instrument's z-axis which typically points towards the Sun. SWIA does not provide information on specific ion species.

As the amount of data the instrument collects is too high to be sent regularly back to Earth, the data is changed into 'coarse' and 'fine' 3D data products. The coarse product averages the smaller angular resolution measurements to create an array with a uniform 22.2 by 22.5 degree angular resolution and a uniform 15% energy resolution but a maximum field of view. Alternately, the fine product uses only measurements from the area covered by the smaller anodes producing an array with 4.5 by 3.75 degree angular resolution and 7.5% energy resolution but a much smaller field of view. By summing over all bins to provide a 1D energy spectrum, the flight software (FSW) onboard MAVEN can compute additionaly information including the number density, vector velocity, pressure and vector heat flux (Halekas, Ruhunusiri, et al., 2017). Using the ratio of counts in the coarse and fine mode, the FSW can also determine whether the spacecraft is within the solar wind or magnetosheath.

Chapter 3

Solar cycle dependence of the interplanetary magnetic field variability at Mars

The solar wind is a strong driver for the martian ionosphere, and as such knowing the upstream conditions for in situ magnetospheric measurements would provide an insight into the dynamics of the coupling. At Mars, characterising the intricacies of the interaction between the solar wind and the martian plasma environment is particularly difficult due to the complex interplay between the induced magnetosphere and the embedded crustal magnetic fields creating a constantly changing obstacle to the solar wind flow. If both the upstream solar wind and IMF conditions and the magneto- and ionospheric dynamics of a specific moment were known, it would be much easier to understand exactly how specific upstream conditions affect the martian magnetosphere. Although in rare cases, two of the spacecraft currently orbiting Mars do happen to be in a configuration where one is inside the magnetosphere and one is outside, it is far more common that this is not the case and estimates of the upstream conditions are required instead.

Case studies at Mars commonly assume that the IMF is steady for the periods (of up to 3 hours) when upstream measurements are unavailable (DiBraccio et al., 2015; Dubinin et al., 2017; Romanelli et al., 2015), or rely on magnetosheath magnetic field

measurements as a proxy for IMF values (Dieval et al., 2014). Previously the variability of the IMF clock angle (the angle of the IMF in the y-z plane) at Mars has been estimated using magnetic field measurements from the magnetosheath, however this is only suitable for measurements taken at high altitudes and low solar zenith angles (Fang et al., 2018). Although at Mars towards and away sectors of the Parker spiral change on average every 13 days (Brain et al., 2005), Marquette et al. (2018) showed that the IMF is highly variable at timescales on the order of hours, so assumptions of a steady field are often unsuitable. Marquette's study is currently the only work investigating the steadiness of the IMF at Mars and quantifying variability in the IMF strength, clock angle and cone angle. Marquette and co-authors used almost three years of MAVEN magnetometer measurements from near solar maximum (from 2014-2017). It is unclear whether this variability is similar at all stages of the solar cycle, or how appropriate these steady field assumptions might be for measurements from other spacecraft. There are now almost three times as many magnetometer measurements available from MAVEN covering a wider range of the solar cycle phases including solar minimum. Additionally, the inter-relations between the different IMF parameters has not been investigated. For instance, do periods of higher field strengths correspond with steadier field orientation? By calculating the cross correlation between IMF parameters, this study aims to answer such questions.

Building upon this previous work by Marquette et al, magnetometer data taken by the Mars Global Surveyor spacecraft have been analyzed and compared with those of the later MAVEN mission. These results provide an insight into the solar cycle dependencies of the steadiness of the solar wind, and allow for more accurate estimation of IMF properties hours after the previous measurement.

3.1 Methodology

Data for this study were taken from the MGS mission aerobraking phase (spanning 1997-1999) magnetometer measurements, while the MAVEN magnetometer data was recorded during science phase orbits between 2014-2022 (Connerney et al., 2015) and has been split into three periods: the downswing period of solar cycle 24 lasting from

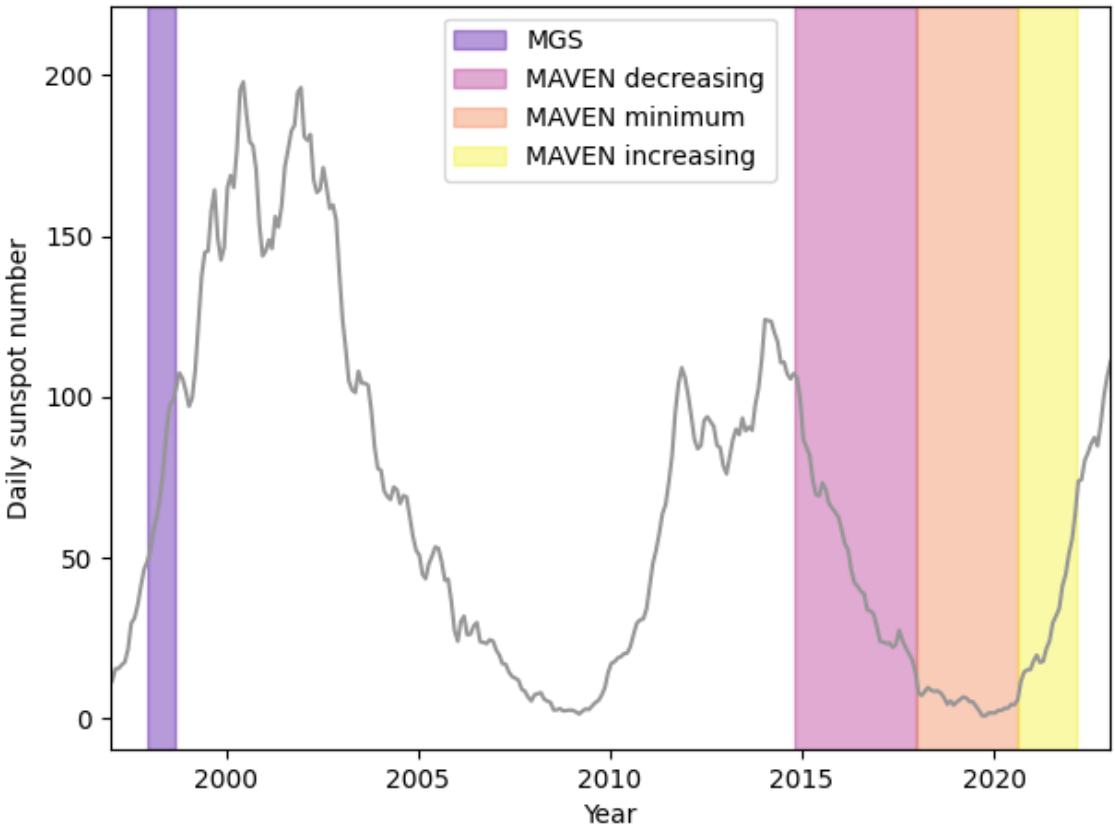

Figure 3.1: Graph of the sunspot number during the last three solar cycles, with the periods of measurement from MGS and MAVEN highlighted in the purple, orange and yellow regions. MGS measurements were taken during the rising phase or upswing of solar cycle 23, whilst MAVEN measurements were taken during a much longer period and have been separated into the declining phase or downswing of cycle 24, solar minimum and the rising phase of solar cycle 25.

September 2014 to December 2017; the minimum period of solar cycle 24 lasting January 2018 to July 2020 and the upswing period of solar cycle 25 spanning August 2020 to February 2022. Measurement periods are shown in Figure 3.1, along with the daily sunspot numbers. The Vignes et al. (2000) model of the martian bowshock location was used to identify times when the spacecraft was located in the IMF. To guarantee the use of only pristine IMF measurements (or as close as possible), an additional buffer was added to the Vignes model boundary of one Mars radii (RM or R_M). The effect of

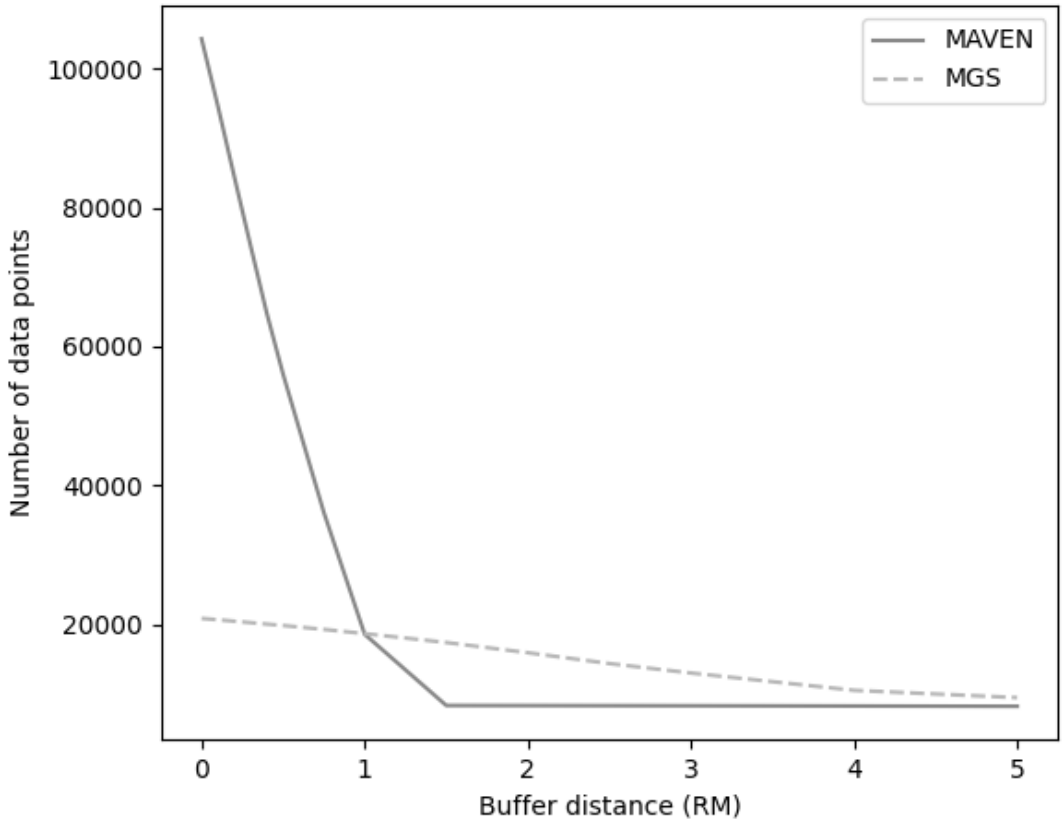

Figure 3.2: Graph showing the number of available solar wind measurements from the MGS and MAVEN spacecraft with the use of a range of buffer values onto the Vignes at al. (2000) magnetospheric shock boundary model.

the buffer on reducing available solar wind data points is shown in Figure 3.2.

For this study, the IMF was parameterised in spherical coordinates, and so is described by the field strength, clock angle and cone angle in Mars solar orbital (MSO) coordinates. In Cartesian MSO coordinates, x is defined as the direction towards the Sun from Mars, y is defined as antiparallel to the direction of the planet's orbital motion and z completes the right-handed set. In this system B_x, B_y and B_z are the components of the magnetic field in the x,y and z directions respectively. The clock angle is defined as $\Theta_{clock} = tan^{-1}(\frac{B_y}{B_z})$, and describes the orientation of the field in the plane perpendicular to the Mars-Sun line. This angle can range from -180 degrees to

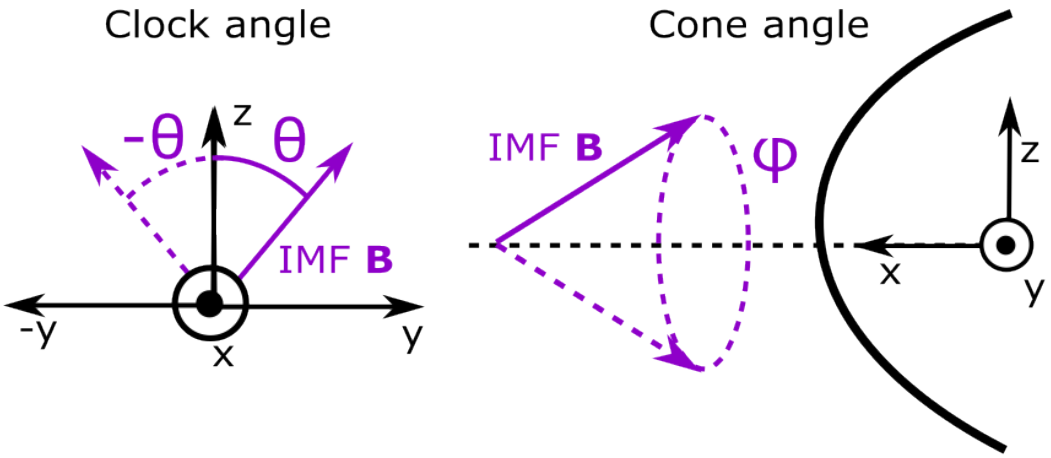

Figure 3.3: Diagram showing the clock and cone angles of the IMF.

plus 180 degrees, with 0 degrees referring to a northward field. The cone angle is the angle of the field out of the ecliptic plane, and is defined as $\Theta_{cone} = cos^{-1}(\frac{-B_x}{|\boldsymbol{B}|})$, where B_x is as defined above and $\boldsymbol{B}$ is the magnitude vector magnetic field of the IMF. This angle ranges from 0 to 180 degrees: 0 degrees referring to field pointing away from the Sun, 180 degrees referring to field pointing towards the Sun and 90 degrees referring to field perpendicular to the Mars-Sun line. Diagrams showing the clock and cone angles are found in Figure 3.3.

The autocorrelation functions of the field strength, clock and cone angles were calculated using the Pearson correlation coefficients for time lags with increasing intervals of 10 minutes. For measurements of parameter X; X_1, X_2, X_3 taken at times t_1, t_2, t_3, the autocorrelation coefficient r for a specific time lag Δt is given by

$$r_{\Delta t} = \frac{\Sigma_{i=1}^{N-\Delta t}(X_i - \overline{X})(X_{i+\Delta t} - \overline{X})}{\Sigma_{i=1}^{N}(X_i - \overline{X})^2} \tag{3.1}$$

where N is the number of measurements of parameter X and $\overline{X}$ is the mean value of

parameter X.

Because of the elliptical orbits of the MGS and MAVEN spacecraft at Mars, measurements of the IMF are intermittent. To remove any effects this might have on the autocorrelation results, data from both spacecraft were averaged and resampled at a frequency of one measurement per minute. The Mars Global Surveyor data coverage includes three large gaps within the data set of around one month each and so these periods were excluded from the analysis. Elsewhere, minutes during which there were no measurements were ignored when calculating the autocorrelation values. Using 1/e as a minimum value for the IMF to be considered autocorrelated, decorrelation times were calculated and compared to the previous Marquette et al. (2018) study. To investigate whether certain values of these properties had stronger correlation than others, subsets of the data were created by splitting measurements based on cone angle and field strength.

$$X_{estimate} = \bar{X} + r(X - \bar{X}) \tag{3.2}$$

Using this method, there is a clear periodicity in the autocorrelation functions that is due to the spacecraft orbit. As MAVEN has a consistent orbital period of approximately 4.5 hours, the periodicity in the MAVEN autocorrelation functions is very clear. To minimise effects of the orbital period on the autocorrelation function, a sixth order polynomial of the form

$$r(\Delta t) = a_0 + a_1\Delta t + a_2(\Delta t)^2 + a_3(\Delta t)^3 + a_4(\Delta t)^4 + a_5(\Delta t)^5 + a_6(\Delta t)^6 \tag{3.3}$$

where Δt is the time lag and a_0, a_1, a_2, a_3, a_4, a_5 and a_6 are coefficients, was fitted to the data with points weighted by the number of available measurements at that time lag. Particularly for MAVEN, as there are fewer periods of available measurements with time lags around half the period of the spacecraft's orbit, these measurements are less influential to the final polynomial. An example of the calculated autocorrelation values for each time lag and the polynomial best fit associated are shown in Figure 3.4.

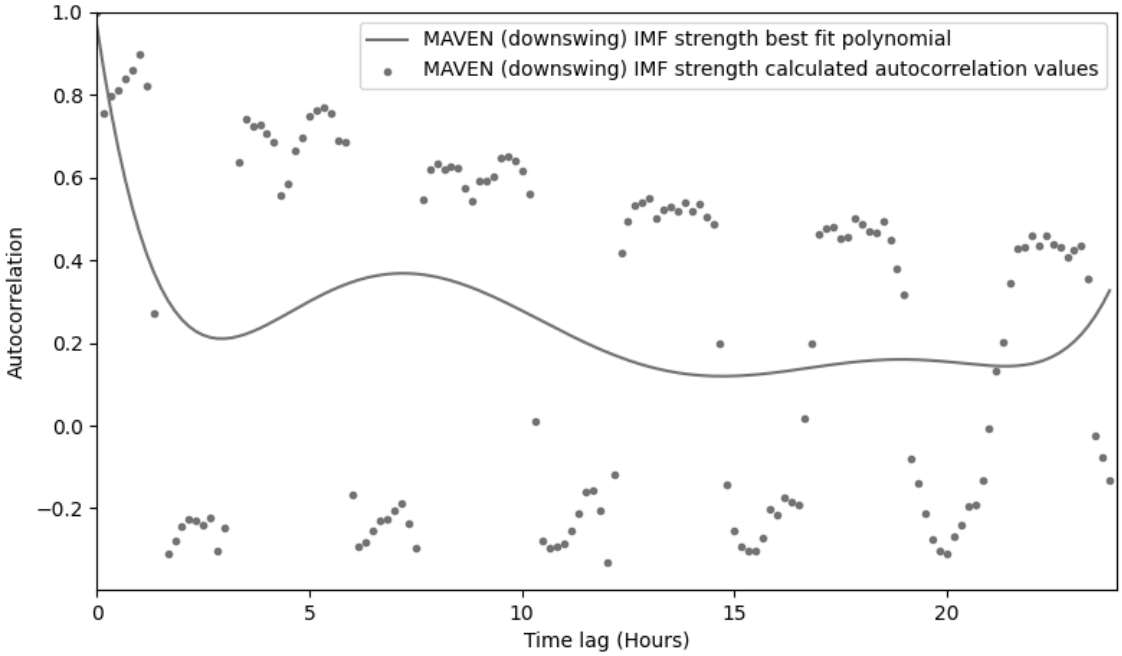

Figure 3.4: An example graph showing the calculated autocorrelation values for the MAVEN downswing field strength and the best fit sixth order polynomial. Polynomial fits for other time periods and IMF components can be found in the appendix.

Similar graphs for all other parameters can be found in the appendix of this thesis.

The error in estimating a component (e.g. the field strength) of the magnetic field at a time after previous measurement was calculated as

$$\sigma_{estimate} = \sigma_{data}\sqrt{1 - r^2} \tag{3.4}$$

where σ_{data} is the standard deviation of the component for the entire data set and r is the autocorrelation value at the given time lag.

3.2 Results

3.2.1 Distribution of IMF values

Figure 3.5 shows the relative distributions of IMF strength, clock angle and cone angle measurements during the MGS and MAVEN measurement periods. This plot shows that the distribution of measured IMF strength has a similar peak for the MGS and MAVEN datasets, except for the most recently measured dataset showing the increasing phase of solar cycle 25. This upswing section of MAVEN measurements shows higher IMF strengths to be much more common, with a peak strength of approximately 6 nT compared to 2.5 nT to 3 nT for all other datasets. Additionally, all MAVEN datasets measured a larger proportion of higher field strengths than the MGS dataset.

The central panel of Figure 3.5 presents the distribution of clock angles observed by MGS and MAVEN. Measurements from MGS show westward (negative) clock angles to be more frequently observed than eastward (positive) clock angles. The MAVEN measurements had a more pronounced eastward-westward asymmetry, however the peaks in the distribution remained at the same angles (approximately -160 and +160 degrees) for all sets of measurements except for the most recent MAVEN upswing dataset.

The distribution of measured cone angles for the two spacecraft is shown in the lower panel of Figure 3.5. MGS regularly measured a distinctly smaller range of cone angles, with a tighter distribution centred around 100 degrees. Data from MAVEN datasets (excluding the upswing dataset) shows a broader distribution, with angles close to parallel to the Sun-Mars line making up a larger proportion of the total measurements. The upswing MAVEN data shows a starkly different distribution, with angles near the ecliptic plane making up a much higher proportion of measurements than those far from the ecliptic plane. This distribution has peaks at angles of 25 and 155 degrees.

3.2.2 IMF Variability

The autocorrelation times of the MGS and MAVEN IMF strengths are presented in the upper panel of Figure 3.6. Measurements of the IMF properties are considered

decorrelated (i.e. no longer influenced by previous conditions) once their autocorrelation value is equal to or below 1/e (approximately 0.37), which is shown as a dotted line on the panels of the figure. The time taken for this to happen is referred to as the 'decorrelation time,' and is a useful measure in characterising and comparing the variability of different IMF characteristics. MGS was autocorrelated for significantly longer than that of the complete MAVEN dataset, with decorrelation times of 6 hours and 1.5 hours respectively. Of the MAVEN periods, both the downswing and minimum periods have decorrelation times similar to the complete MAVEN dataset. The upswing period of MAVEN was decorrelated much faster, with a decorrelation time of approximately 30 minutes.

The IMF clock angle autocorrelation functions are shown on the middle panel of Figure 3.6. All of the MGS and MAVEN datasets have very similar clock angle autocorrelation functions, which decorrelate at time lags between 30 minutes and one hour. The bottom panel of the figure shows the autocorrelation functions of the cone angles.

Similar to the IMF strength functions, the MGS cone autocorrelation function is correlated for much longer time periods than the MAVEN autocorrelation functions, with a decorrelation time of 6.5 hours. MAVEN autocorrelation functions for all periods other than the upswing have decorrelation times of 1.5 hours, with the upswing decorrelation time being around 20 minutes.

Panels on the left side of of Figure 3.7 present the autocorrelation functions of the field strength, clock angle and cone angle separated by IMF strength. The IMF strength has been split into 4 regimes: low (0-2.25 nT), mid (2.25-3.5 nT), high (3.5-4.75 nT) and extra high (4.75+ nT). Autocorrelation function in this figure are shown only up to 6 hour time lags to focus on time periods used in estimating these values during an orbit of MAVEN. For the IMF strength autocorrelation functions, shown in the upper left hand panel, the maximum decorrelation time for any data set was 2 hours for the low strength and high strength sub sets. This suggests that the IMF strength is highly variable even over these small time periods of a few hours and that estimating the upstream IMF to be constant is unsuitable even for only a few hours since the

last measurement. The clock angle autocorrelation functions, shown in the middle left panel, have an even shorter decorrelation times than the IMF strength with the mid strength subset having a decorrelation time of 1.5 hours and other subsets having times of 40 minutes. The low strength cone angles have the highest decorrelation time of 4 hours, with all other field strengths having cone angles that are decorrelated at time lags between 1 and 2 hours.

Panels on the right side of of Figure 3.7 present the autocorrelation functions of the field strength, clock angle and cone angle separated by cone angle. Cone angles are split into 3 regimes: parallel/anti-parallel (less than 30 degrees out from the Mars-Sun line), middle (between 30 and 60 degrees from the Mars-Sun line) and perpendicular angles (over 60 degrees from the Mars-Sun line) with respect to the ecliptic plane. Parallel and middle cone angles seem to be autocorrelated for longer periods, with perpendicular cone angles being the fastest to decorrelate. This might be expected, as under quiet solar conditions Parker spiral configurations suggest that the IMF should lie close to the ecliptic plane, and should only vary with regards to the change between towards and away sectors of the IMF every 13 days. The prime sources of IMF oriented out of the ecliptic plane are ICMEs and interacting streams, which would be associated with much more variability and would therefore be expected to have lower autocorrelation values.

3.2.3 Estimates and errors

Using the autocorrelation functions from the above graphs estimates of the IMF strength, clock ang cone angles are shown in Figure 3.8. They are calculated using equations 3.2 and 3.4 given in the methodology section of this chapter. As the autocorrelation function decreases, the estimates tend to the mean value measured for each component of the IMF, and the error of estimate tends to the standard deviation.

3.3 Discussion

The MAVEN mission measured IMF cone angles that were less variable and more commonly found close to perpendicular to the Mars-Sun line compared to the MGS measurements. This is consistent with faster, stronger wind which would be expected around solar maximum (Rickett & Coles, 1991). The steadier wind near solar maximum will be more easily propagated to later times to produce reliable estimates of upstream conditions. Alternately, this configuration of IMF is also expected in pile up regions (Bertucci et al., 2004). As the model of the Martian bowshock used in this study to remove measurements inside the planet's magnetosphere was based on bowshock crossings from Mars Global surveyor, it is possible that this model is less suited to MAVEN measurements and has classified sections of draped IMF as pristine IMF measurements. It is unlikely however that the model would be so unsuitable that it would cause such a stark difference between the MGS and MAVEN data sets, particularly as previous analysis of the bowshock terminator position during the period of MAVEN measurement found maximum variations of $0.5R_M$ during a complete solar cycle(Hall et al., 2019).

Field strength autocorrelation values show that the magnetic field measurements from MGS remain autocorrelated for distinctly longer than the measurements from MAVEN. The MGS data was taken during the upswing period of solar cycle 23, however Figure 3.1 shows that the solar activity levels during this period were higher than during the upswing period of cycle 25 which was measured by MAVEN. This could be explained as higher activity periods will have a higher proportion of fast ambient solar wind streams (which are associated with coronal holes). The slower ambient wind has a more intricate magnetic field structure, which could cause less autocorrelation and more variability (Cranmer, 2005). The upswing subset of MAVEN measurements had a much faster decorrelation time, but contained a higher proportion of measurements that were at a higher field strength and angles near the ecliptic plane. Higher field strengths would suggest energetic events, but these would typically have cone angles out of the ecliptic plane.

The clock angle autocorrelation function was decreased sharply for all MGS and

MAVEN measurement periods. When separated by field strength, clock angle decorrelation times were the same for all field strengths except for mid strength. This suggests that the orientation of the field in the x-y plane is not affected by the field strength or the solar cycle and is consistently variable. Outside of energetic events like CIRs and ICMEs, IMF clock angle is mostly dependent on the Parker spiral structure in the IMF. It might be expected that as energetic events occur more frequently during periods of higher solar activity, the clock angle should therefore decorrelate faster during these periods. However, this does not agree with our results, suggesting that these relatively rare events have only a small impact on the total autocorrelation functions during this time.

The cone angle is correlated for a much longer period for MGS measurements than MAVEN ones, and again the MAVEN upswing period is decorrelated much faster than other MAVEN datasets. In general, splitting the IMF measurements by cone angle has little effect on the decorrelation time. Periods where the cone angle is near perpendicular to the ecliptic plane are slightly faster to decorrelate, which is expected as these angles of IMF are associated with energetic events which will be inherently more variable.

Overall, these autocorrelation functions suggest that assumptions that the IMF is steady over the periods of one MAVEN orbit are highly unsuitable in all cases except predicting cone angles during low field strengths. However it may be suitable to assume the IMF strength and cone angle are constant between MGS orbits, depending on the configuration of the orbit and how long the spacecraft is within the magnetosphere. Differences in the variability occur between solar cycles, as we see in the comparison if data from MGS and MAVEN, as well as difference in the frequency of observed strengths, clock angles and cone angles between the upswing periods of solar cycles 23 and 25. Although the MAVEN measurements have likely been affected by the periodicity of the calculated autocorrelation functions, the polynomial fits capture accurately the general trend of the data, which is the most important aspect when comparing the function to determine differences in the variability between the field components. When comparing MAVEN measurements to other MAVEN measurements this should not be an issue, but it is unclear how much this affects the direct

comparison between the MAVEN measurements and those from MGS, where the changing orbit (and decreasing orbital period) has negated any obvious periodicity in the autocorrelation functions.

3.4 Conclusions

- The upswing period of MAVEN measurements contained higher field strengths and southward IMF orientations much more frequently than any other period of measurements
- Field strengths and cone angles measured by MGS were much steadier than those measured by MAVEN, even during similar stages of the solar cycle.
- The clock angle is decorrelated in approximately an hour irrespective of the measurement period, suggesting that the clock angle variability is unaffected by the solar cycle.
- Periods of lower field strengths have more stable IMF strength and cone angle conditions compared to periods of mid, high and extra high field strengths.
- Periods when the cone angle was perpendicular to the ecliptic plane were more variable in all three components of the IMF compared to periods when the cone angle was parallel to or up to 60 degrees out of the ecliptic plane.
- In general, assuming the IMF to be steady is unsuitable for periods of more than one hour since the last measurement for all MAVEN measurements or 6 hours since the last measurement for MGS strength and cone angle measurements.

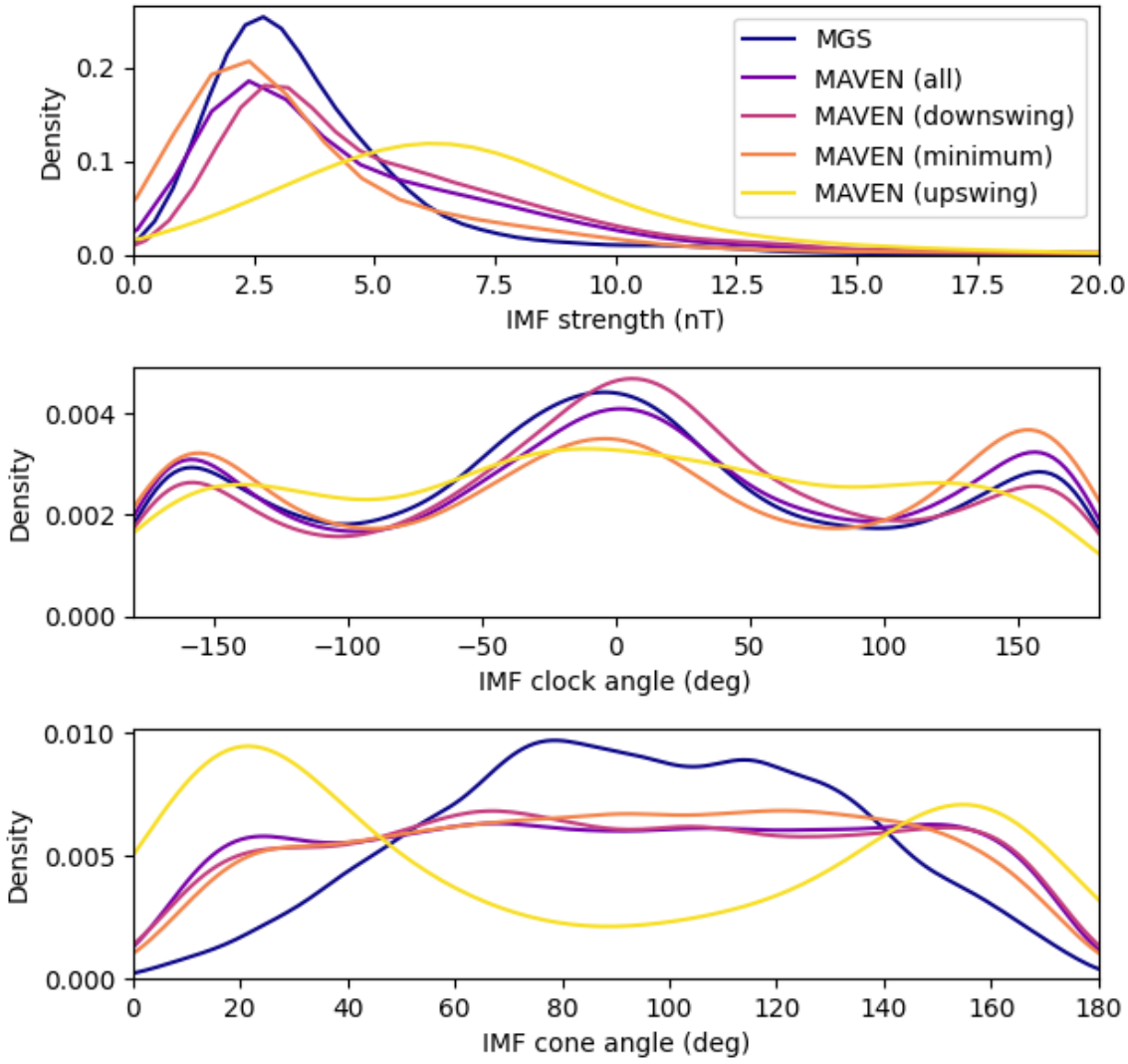

Figure 3.5: Kernel-smoothed probability density graph showing the distribution of ten minute averaged IMF field strength, clock angle and cone angle measurements taken by Mars Global Surveyor and MAVEN. The y-axis denotes the probability of the IMF measurements to be a given value at a random time (i.e. the probability that MGS measures the IMF strength to be 2.5 nT at a random time is approximately 0.22).

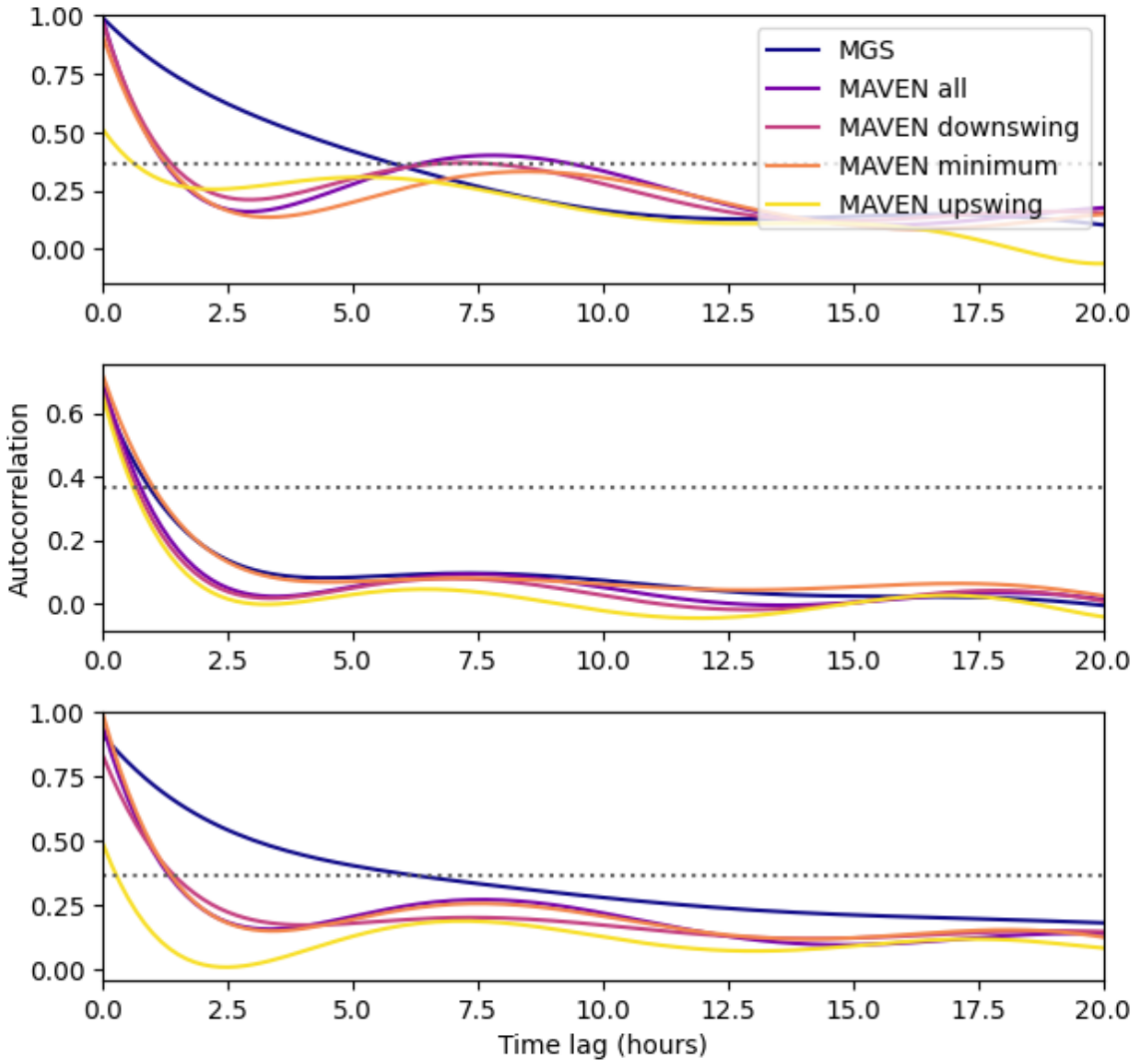

Figure 3.6: Graph showing the autocorrelation functions of the IMF strength, cone angle and clock angle for data from MGS and MAVEN.

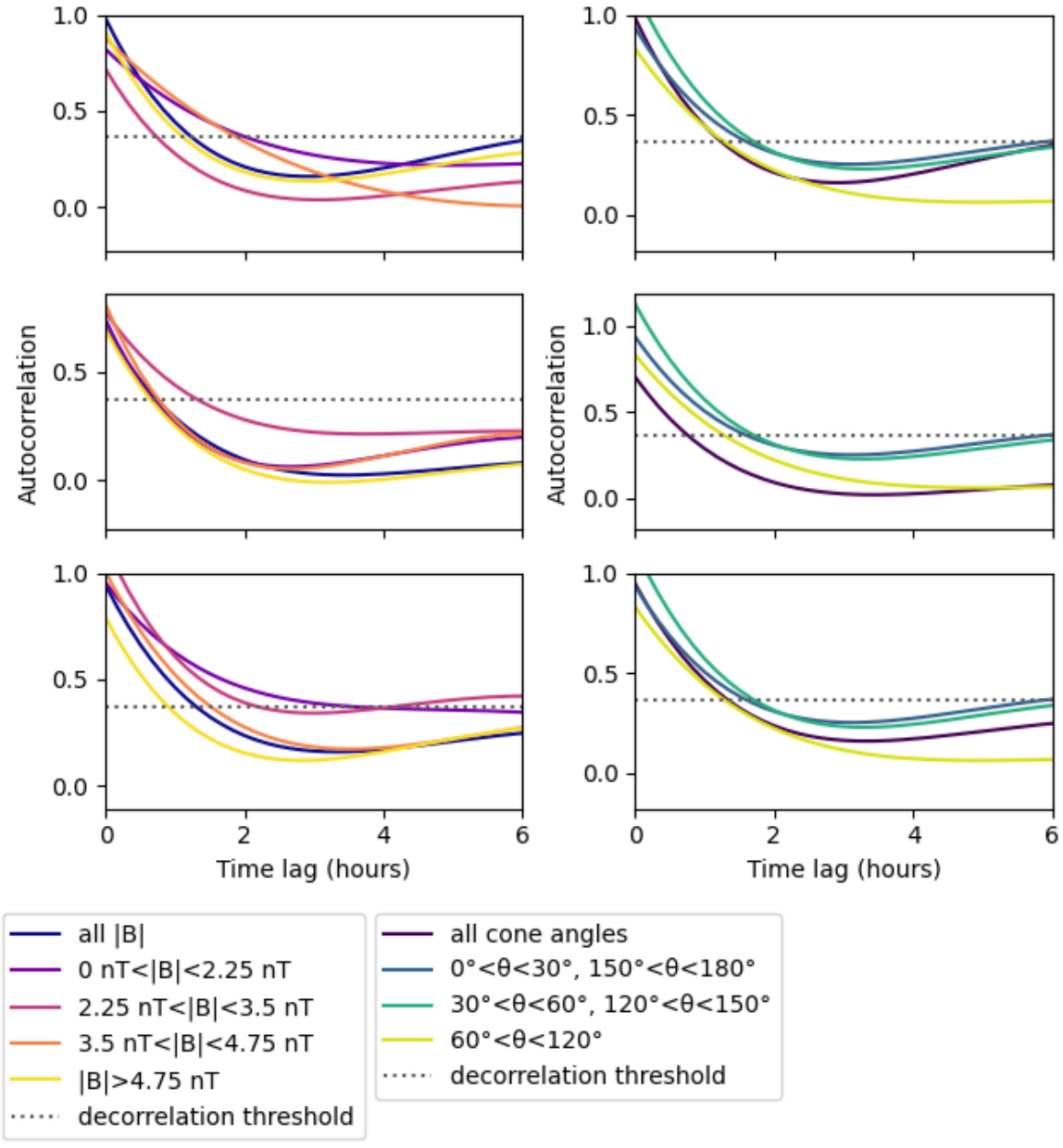

Figure 3.7: Graph showing the autocorrelation functions of IMF strength, clock angle and cone angle measurements at varying time lags taken by MAVEN and separated by strength and cone angle.

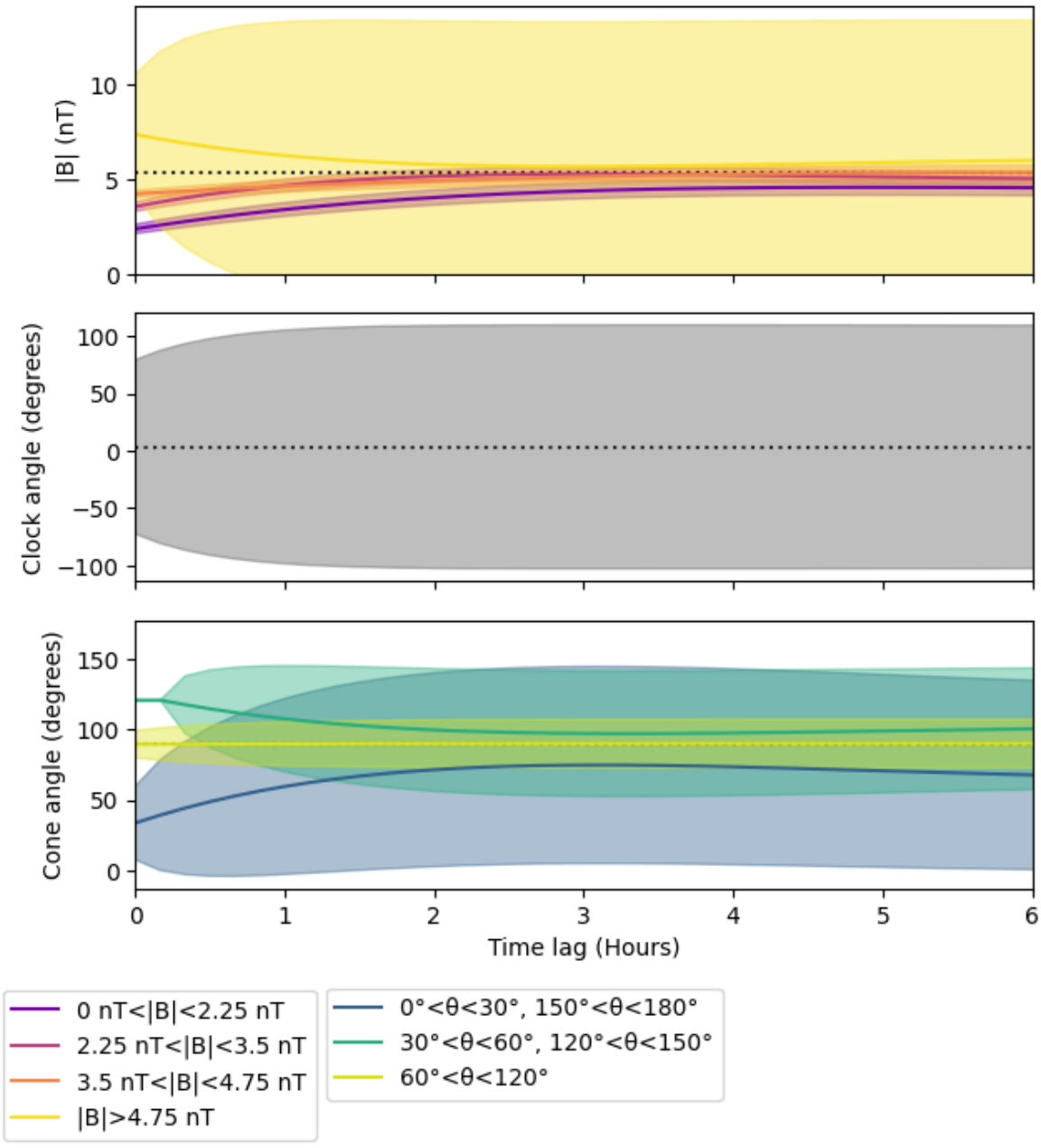

Figure 3.8: Graph showing estimates of the IMF strength, clock angle and cone angle at times up to 6 hours after the previous measurement. Different colours in the upper and lower panels show the estimates for different field strengths and cone angles. The dashed lines show the mean values of the IMF properties as observed by MAVEN. The shaded regions show the errors in the estimates.

Chapter 4

Predicting solar wind conditions using deep learning

The aim of this study is to produce a model suitable for hindcasting solar wind conditions at Mars during periods where no in situ measurements are available. During these periods, where spacecraft such as MAVEN will be inside the martian magnetosphere, additional estimates of the upstream solar wind conditions will improve our understanding of solar wind drivers on the martian plasma environment.

Previously, work using an artificial neural network (also referred to as simply a neural network or NN) has been used to predict average solar wind conditions based on measurements taken in the magnetosheath region (Ruhunusiri et al., 2018). Although the model in this study is successful, in order to provide training data of both the magnetosheath conditions which the model takes as input and solar wind conditions which it aims to predict, it assumes solar wind conditions to be relatively constant during an orbit of MAVEN. The work shown in Chapter 3 of this thesis shows that this is not a suitable assumption to make in most cases.

This study builds upon the concept of utilising machine learning (specifically a NN) to improve current abilities to estimate solar wind conditions upstream of Mars, whilst also providing higher time resolution in the predictions in attempt to capture the inherent variability within solar wind conditions.

4.1 Data & Methodology

Measurements for this study were taken from the MAVEN spacecraft. Measurements taken inside the magnetosphere were removed and the measurements were averaged over a period of 30 minutes. The period of over which the measurements were taken is from 21 September 2014 to 22 February 2022. Because the model requires periods of nine consecutive (30 minute averaged) measurements, only a small percentage of the total MAVEN measurements can be used. A period was deemed suitable if half-hour averaged values were available for the full four and a half hours for all of the properties measured. Of 130,167 possible four and a half hour periods of measurements, 48,758 periods were suitable for using in the model.

4.1.1 Model Specification

The deep learning model takes data from three time steps prior to the prediction period and two time steps after as inputs to predict the four time steps in between. Four measurements spaced 30 minutes apart were chosen for the prediction period as two hours is the time average period that MAVEN spends inside the magnetosphere on a typical orbit. This prediction period allows for our model to be trained on and applied to the most orbits possible. Although it would be preferable to have a higher temporal sampling frequency, the complexity of the neural network is proportional to the number of neurons squared, meaning that it can quickly become too large to be trained in a reasonable time frame. The model takes as both input and output the vector interplanetary magnetic field, vector velocity, proton density and temperature and dynamic pressure of the solar wind.

The input matrix of MAVEN observations $I = \begin{pmatrix} \boldsymbol{X_{t=1}} & \boldsymbol{X_{t=2}} & \boldsymbol{X_{t=3}} & \boldsymbol{X_{t=8}} & \boldsymbol{X_{t=9}} \end{pmatrix}$

The output matrix of values for the model to predict $O = \begin{pmatrix} \boldsymbol{X_{t=4}} & \boldsymbol{X_{t=5}} & \boldsymbol{X_{t=6}} & \boldsymbol{X_{t=7}} \end{pmatrix}$

where $\boldsymbol{X_t}$ is column vector containing the measurement of each of the nine solar wind

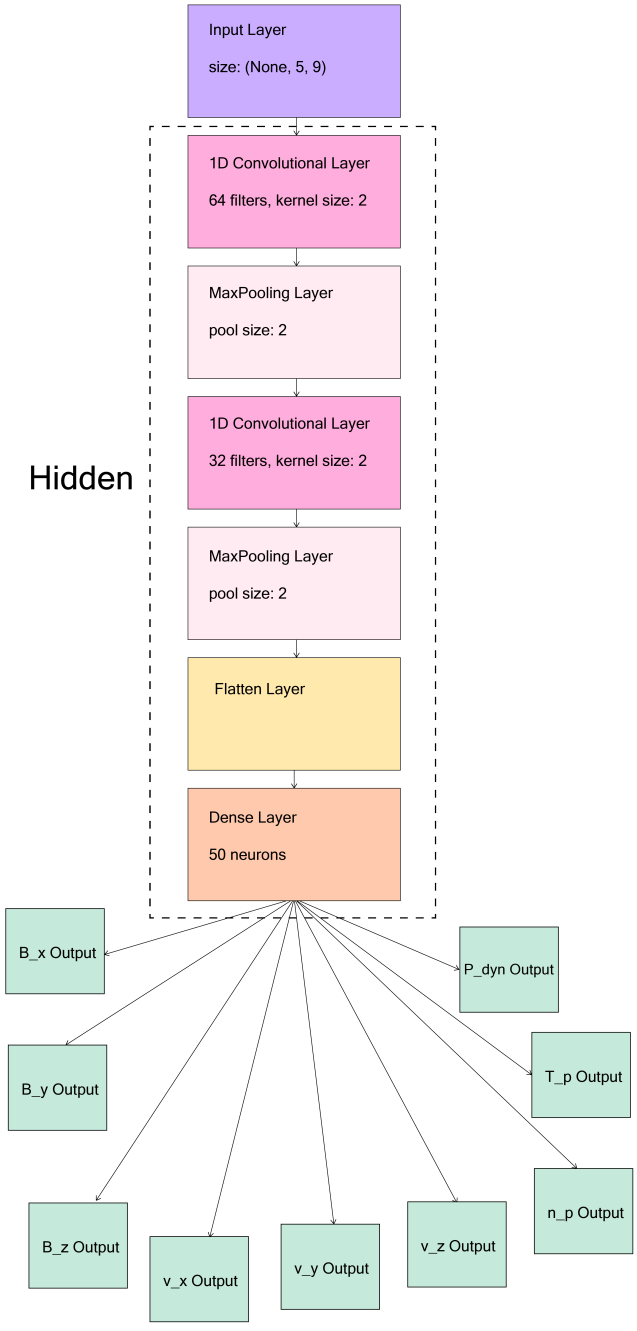

Figure 4.1: Diagram of the model structure.

properties in the model taken at time t such that $\boldsymbol{X_t} = \begin{pmatrix} B_{x,t} \\ B_{y,t} \\ B_{z,t} \\ v_{x,t} \\ v_{y,t} \\ v_{z,t} \\ n_{p,t} \\ T_{p,t} \\ P_t \end{pmatrix}$

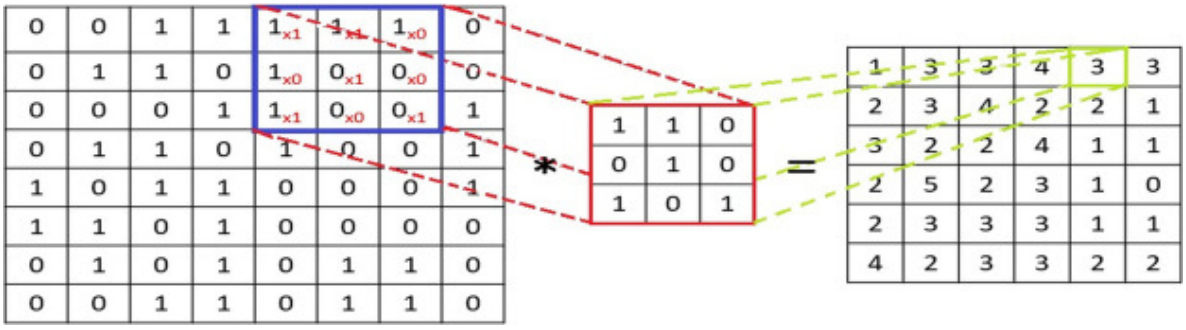

Figure 4.2: Example of how a convolutional layer transforms an input array. Taken from (Singh et al., 2020).

The choice of a convolutional neural network for this study was made as these networks are the most suitable at identifying and extracting high level features from input data. The structure of the neural network used in this study is shown in Figure 4.1. The convolutional layers convolve a one dimensional kernel (also called a filter) with the inputs to their layers. These layers change an original single tensor into a 'feature map' which is comprised of the dot products of the convolving kernel with portions of the original array. After each convolutional layer, there is a max pooling layer which decreases the size of the input array by taking the max value from each portion of the array and removing all other values from the section. Example transformations of convolutional and max pooling layers and shown in Figures 4.2 and 4.3.

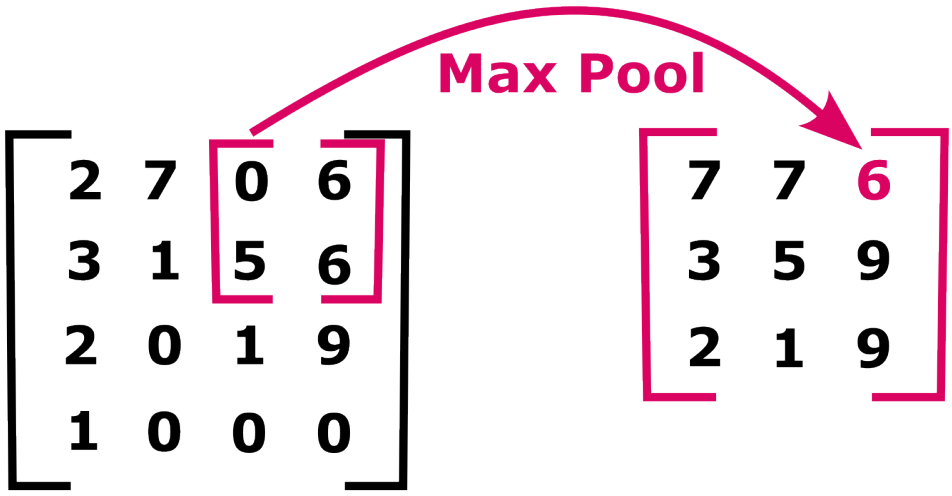

Figure 4.3: Example of how a max pooling layer transforms an input array.

The model uses a mean squared error loss (MSE) function, which is defined as

$$MSE = \frac{1}{N}\sum_{i=0}^{N}(y_i - \hat{y}_i)^2 \tag{4.1}$$

where y is the value of a parameter measured by MAVEN, ŷ is the value of the same parameter predicted by the model and N is the number of predictions. The MSE is a measure of how far away the model's predictions are from the measured values it was predicting. This loss function (also known as the objective function when talking about the optimising algorithm) is the function that the model aims to minimise during the training period to produce the most accurate model. The optimiser chosen for this model is the adaptive moment estimation (ADAM) algorithm. This method is a variation of the gradient descent method, which is used to choose the weights for the model to improve its accuracy. Unlike the traditional gradient descent methods, this method computes adaptive learning rates for each parameter, and this has been shown to be an effective algorithm for CNNs (Kingma & Ba, 2015).

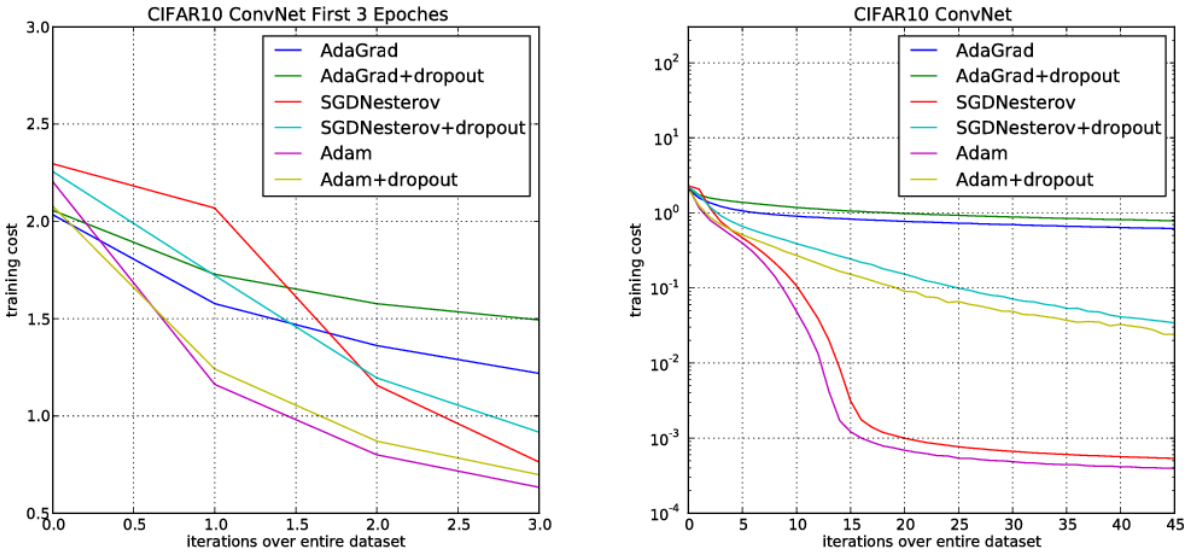

Figure 4.4: Graph showing the training cost of a CNN, run using various optimiser algorithms to predict the CIFAR-10 dataset. Taken from Kingma and Ba (2015)

The architecture of the network is fairly simple, with an input layer, a convolutional layer, a max pooling layer, another convolutional layer, another max pooling layer, a dense, fully connected layer and nine fully connected outputs, one for each SW property predicted, each with four neurons. Figure 4.1 shows a visual representation of the model architecture. The model uses the rectified linear unit (ReLU) activation function for the nodes, performing the function

$$ReLU(x) = max(0, x) \tag{4.2}$$

on input values. This function is preferred for deep neural networks over the more common tangential, sigmoid or linear transfer functions as it converges quickly and reliably (Dahl et al., 2013).

To quantify the benefit of using the transfer learning model, a separate model with the same structure was trained on only the available in situ data from MAVEN. Figure (enter figure reference here) shows the mean average error (MAE) for the predictions of each of the seven properties of the solar wind at each forecasted time step for both the model trained on OMNI Earth data and the model trained on MAVEN Mars data.

4.2 Results

4.2.1 Model accuracy

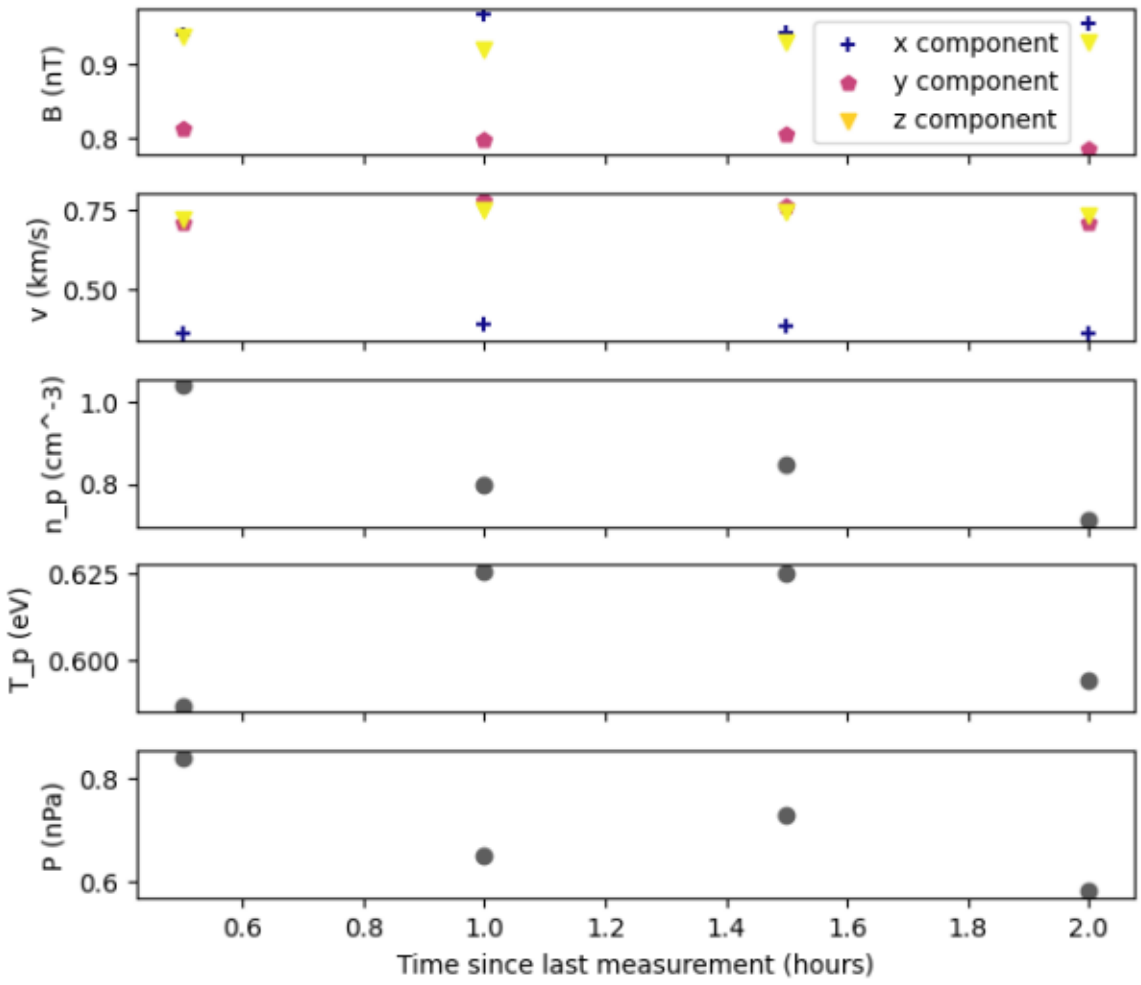

Figure 4.5: Graph showing the root mean squared error (RMSE) of the model's predictions for each parameter and time step.

Figure 4.5 shows the root mean squared error (RMSE) for the predictions of each of the nine properties of the solar wind at each time step for the model. These values are averaged over the entire test set and do not include errors associated with the original measurements by the spacecraft instruments. All properties have small RMSE values

for all time lags, Particularly, all three components of the velocity have RMSE values of less than 0.8km/s for all time lags, which is a small percentage of the velocities which range from -600 km/s to 10 km/s for the x component and and -100 km/s to 105 km/s for the y and z components.

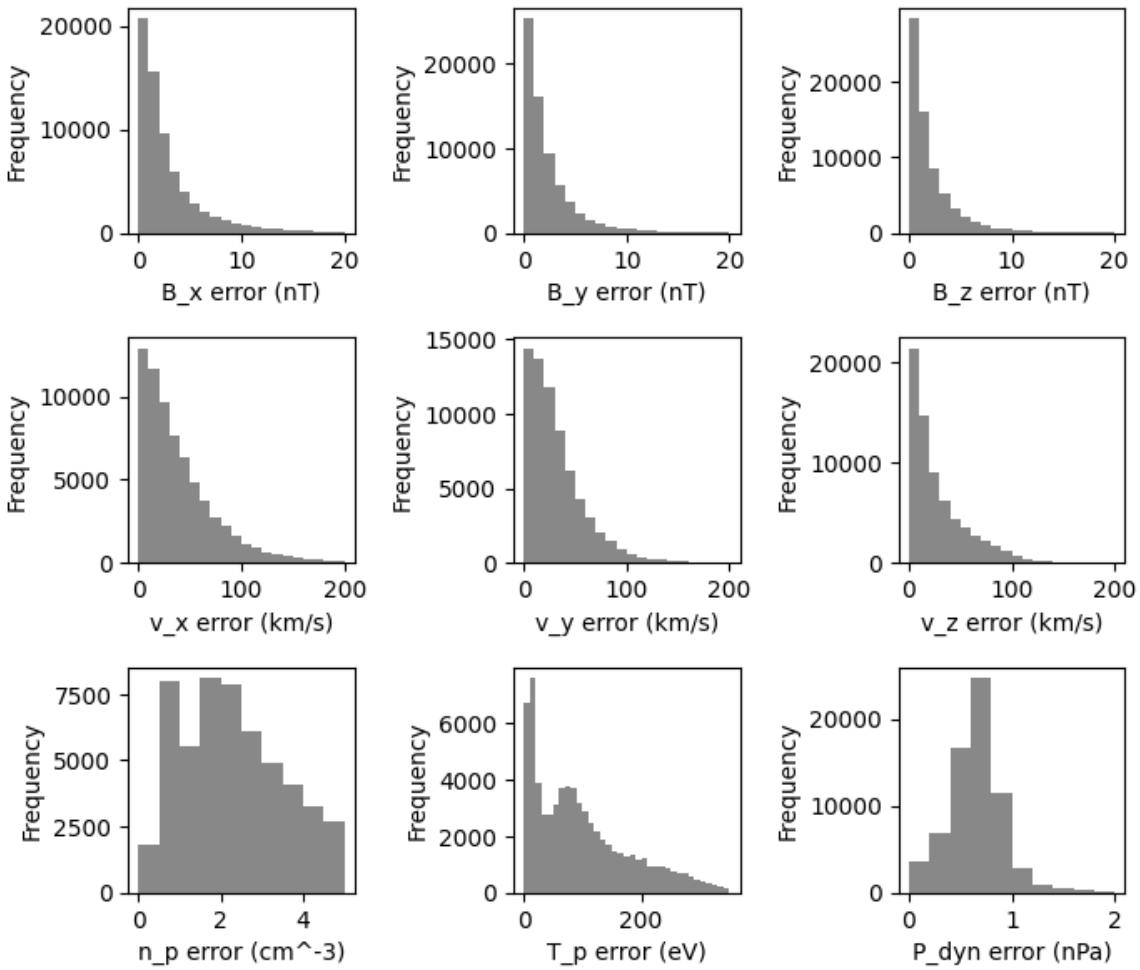

Figure 4.6: Histograms showing the distribution of differences between the model's predicted values and the measured values from MAVEN. The total number of measurements in each histogram N = 682654.

Figure 4.6 shows a histogram of how far each of the predictions was from the measured values in the test set. Approximately 29% of B_x predictions, 37% of B_y predictions

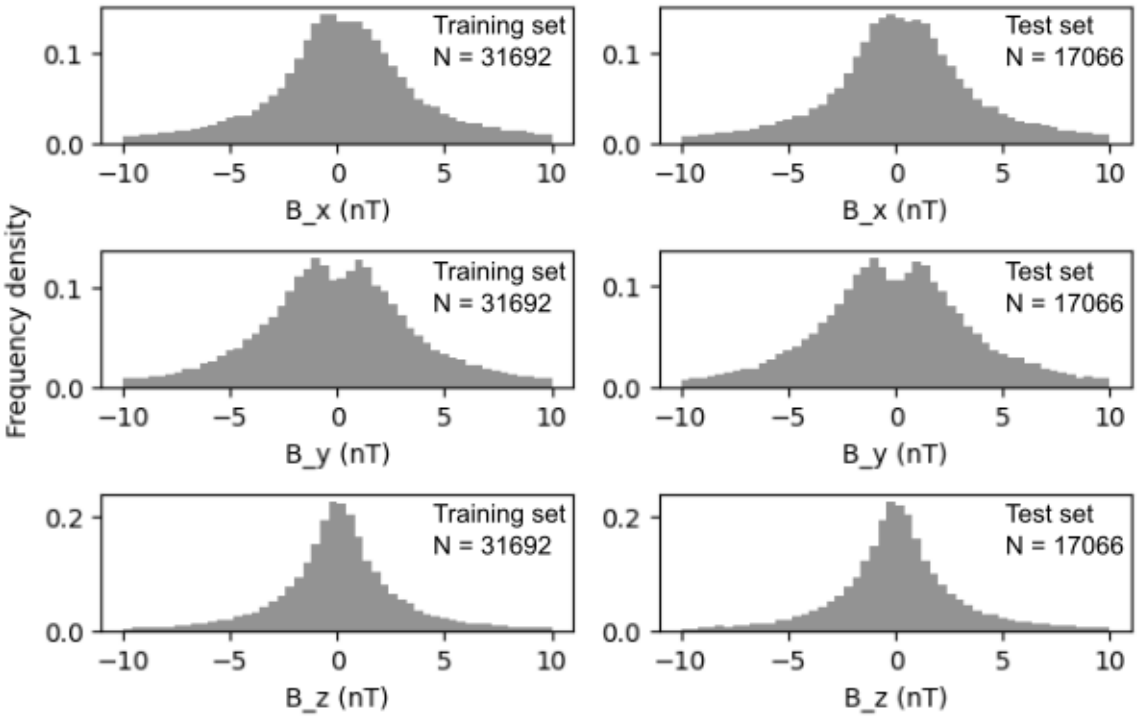

Figure 4.7: Graph showing the distribution of IMF values in both the training and test sets for the interplanetary magnetic field measurements.

and 42% of B_z predictions are less than 1 nT away from the measured values. For the velocity, 18% of v_x predictions, 21% of v_y predictions and 31% of v_z predictions were within 10kms^{-1} of the measured velocities. 15% of the proton density measurements were within 1cm^{-3}. 10% of the proton temperature measurements were within 1 eV. 70% of dynamic pressure measurements were within 1 nPa of the measured values. These results show that the model can accurately predict many of the input values but doesn't provide close predictions for all of the test data. Figures 4.7, 4.8 and 4.9 show the distribution of measured values in the training and test sets.

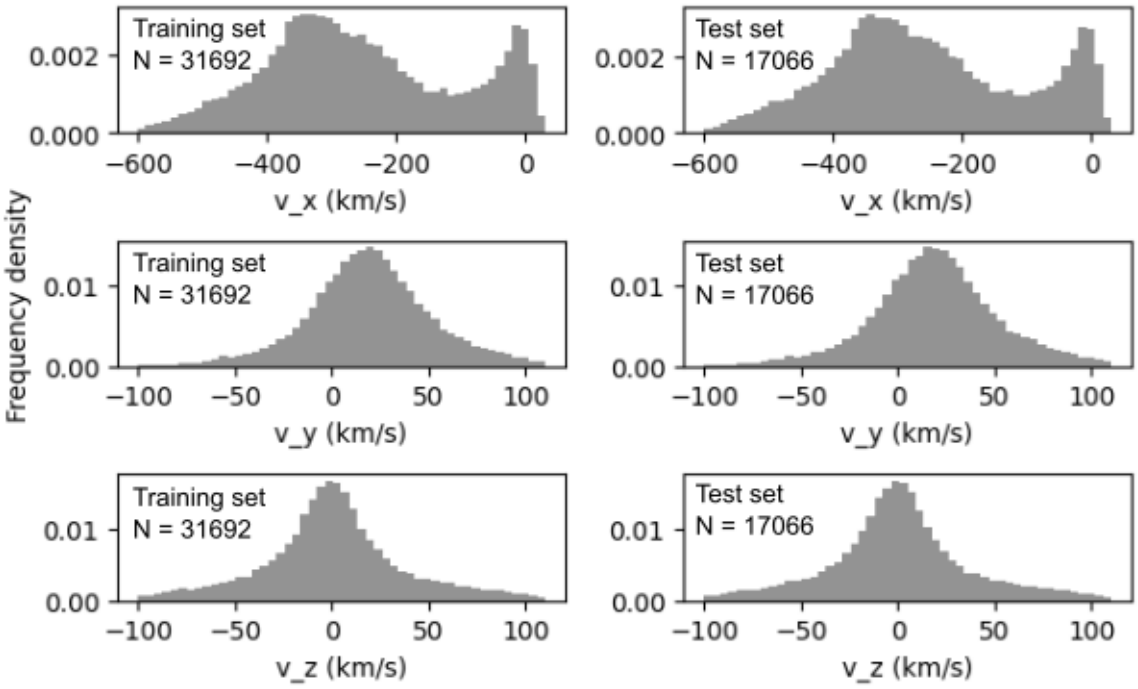

Figure 4.8: Graph showing the distribution of solar wind velocities values in both the training and test sets for the solar wind velocity measurements.

4.2.2 Model generalisability

To make sure that this model is suitable for using for a range of solar wind conditions and periods of the solar cycle, it should be trained well enough that it can approximate the behaviour of the solar wind components in the training set, but not so well that it has learned to reproduce exactly the training data and will be unable to predict new data it has not been trained on (known as overfitting). Methods of ensuring generalisabilty that are used in this study are limiting the amount of training data, such that the model will not have enough measurements to use to become overfitted, and simplifying the model by removing unnecessary layers and neurons.

The difference in mean squared errors of the models with one, two or three fully connected layers after the convolutions was minimal. By choosing to use the model with only one fully connected layer, we are keeping the model in a simpler form that

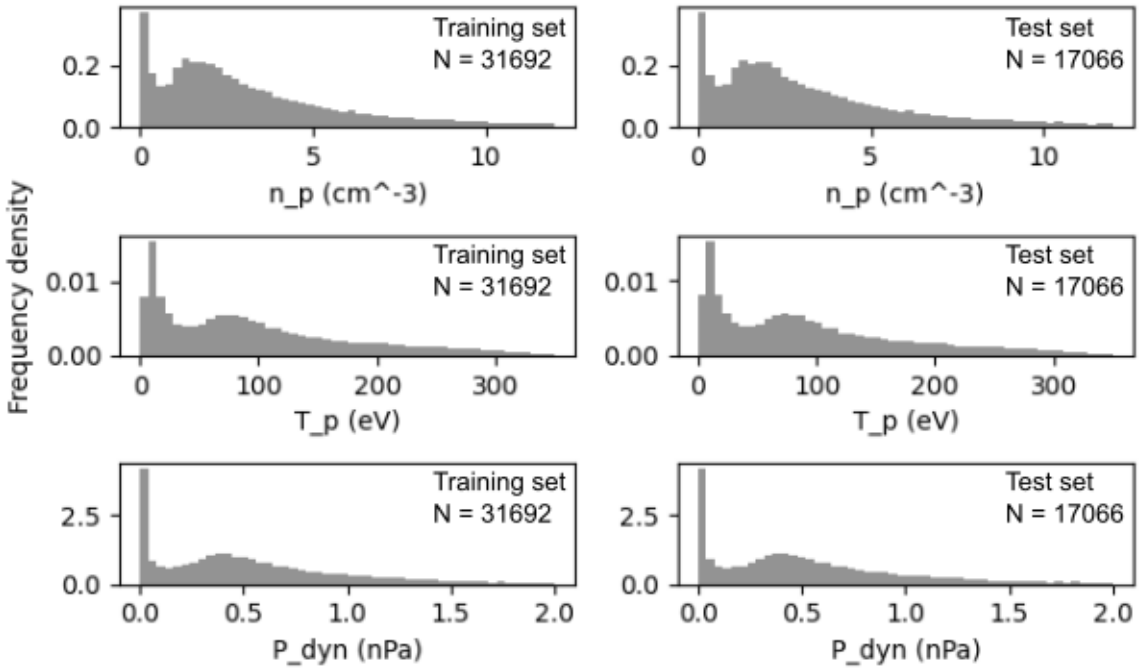

Figure 4.9: Graphs showing the distribution of values in both the training and test sets for the proton density, proton temperature and dynamic pressure measurements.

will make it inherently more general.

Figure 4.10 shows the loss values for the training and test sets for each of the predicted properties of the solar wind for models trained on different percentages of the total data. As the model is trained on larger percentages of data, the loss in its predictions decreases and the loss on the test data increases. This is indicative of the model being overfitted; it is learning to reproduce exactly the training data but will not be able to successfully predict any new data. To stop this, the model in this study was given a 65/35 train/test split (with no overlap between the training and testing data) to negate overfitting but allow for the model to learn a general view of the solar wind properties and how they evolve with time.

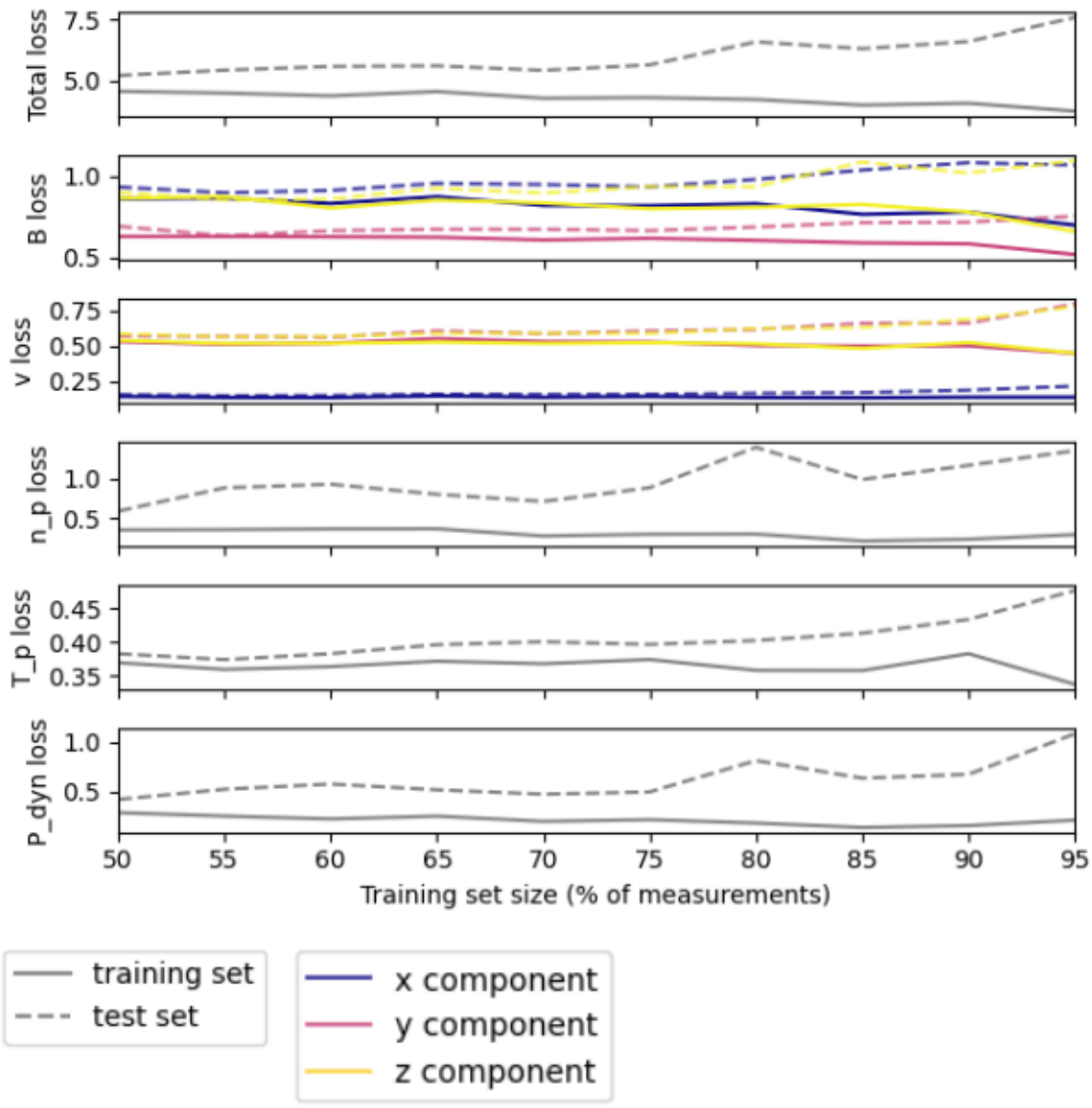

Figure 4.10: Graph showing the loss (both total and for each solar wind component).

4.2.3 Case studies

4.2.3.1 21 November 2018

To get a better understanding of how this model would be used in practice, two case studies taken from the test dataset are detailed in this section. The predicted values

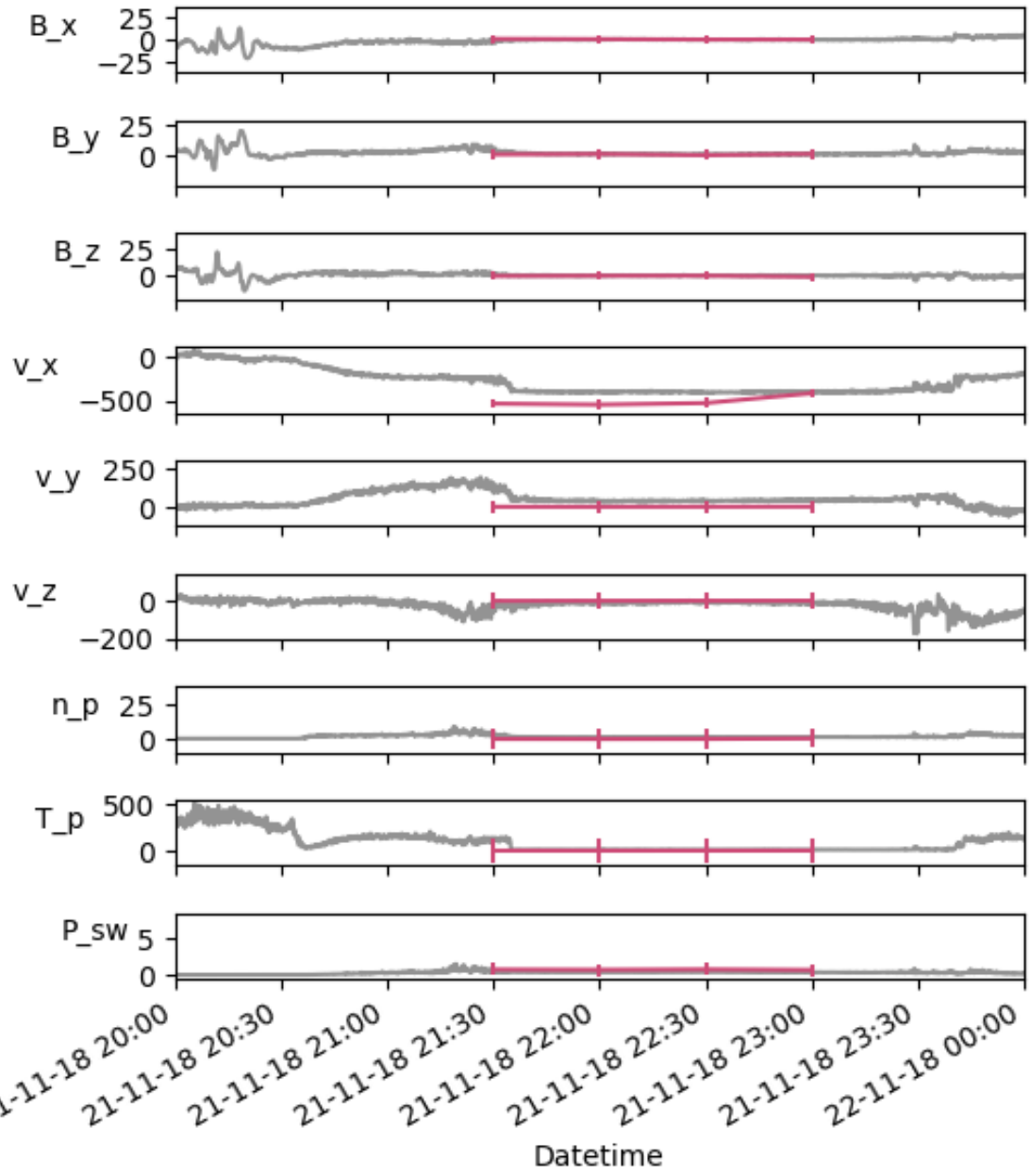

Figure 4.11: Graph showing the values of the magnetic field, velocity, proton density, temperature and dynamic pressure of the solar wind measured by MAVEN on 21 November 2018, shown in grey. Model prediction and errors are overlaid in pink.

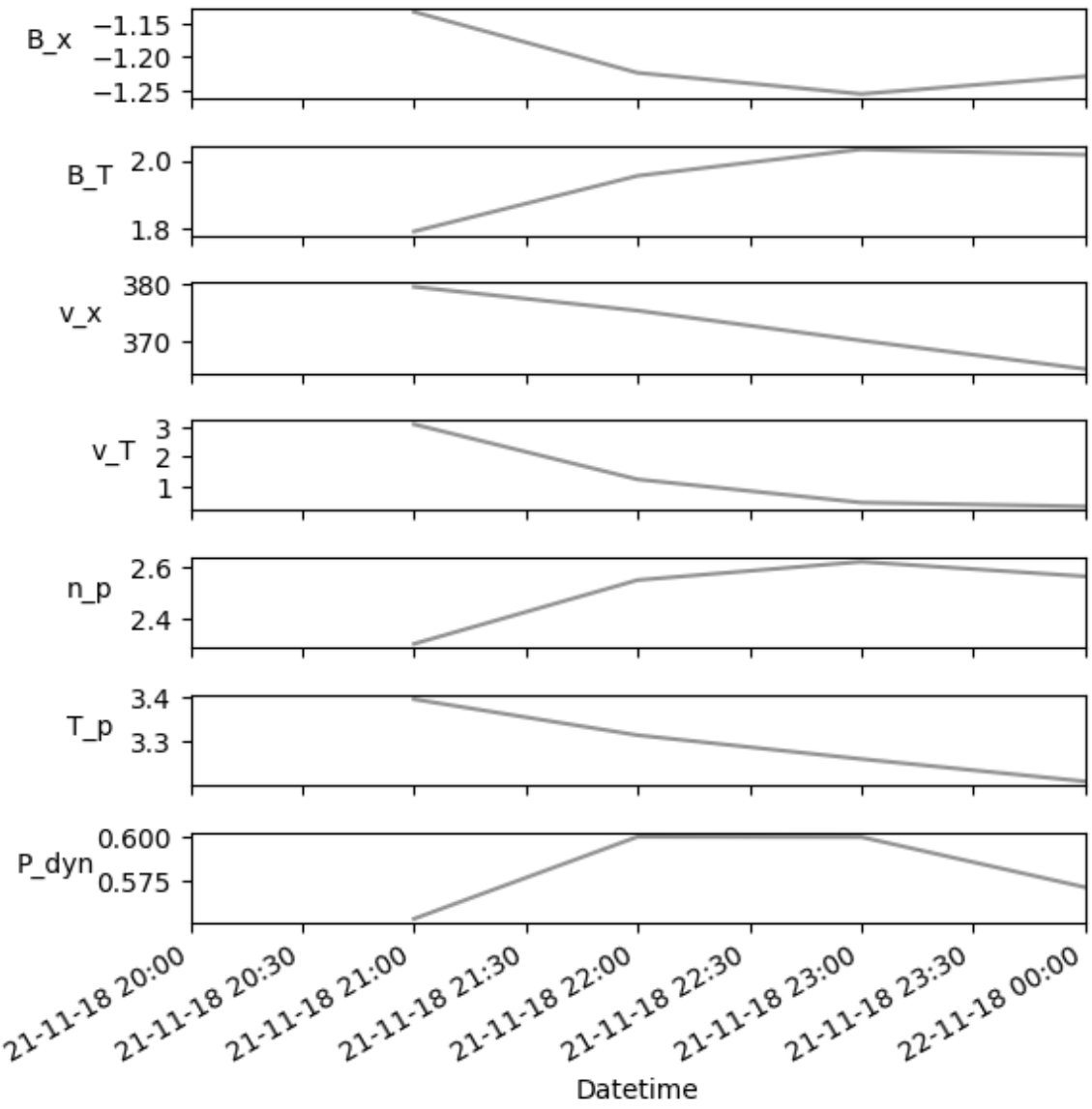

Figure 4.12: Graph showing the solar wind values predicted by the Tao et al model on 21 November 2018. $B_T = \mathrm{sqrt}(B_y^2 + B_z^2)$, $v_T = \mathrm{sqrt}(v_y^2 + v_z^2)$

from our model are also compared against the model specified in Tao et al., (2005). The first case study is taken from a period of ambient solar wind conditions, and shows predictions of the typically low values of each of the parameters. Measurements from MAVEN and the model predictions are shown in Figure 4.11. The error bars show the

RMSE of each parameter at each time step as shown in Figure 4.5. With the exception of the x velocity, all parameters are predicted accurately, with the measured values within the uncertainties on the predicted measurements. The model underestimates the velocity of the solar wind in the x direction, however the prediction from the Tao model shown in Figure 4.12 overestimates (underestimates) this component of the velocity to a similar degree.

4.2.3.2 21 February 2019

Measurements from MAVEN and the model predictions for this case study are shown in Figure 4.13. This case study shows a small period of rapidly undulating magnetic field measurements around 08:15 to 08:45 as well as increased x velocity and enhanced proton densities and temperatures. Unfortunately the model completely misses the period of variable field strength and orientation, however as this was during a short period of time it is questionable how visible this disturbance would be within a 30 minute averaged time series. The model captures well the general increase in the x component of the velocity, while the Tao model predicts the x velocity to be positive and fairly constant in the same period (as shown in Figure 4.14. Both this model and the Tao model predict near zero values for the temperature, density and dynamic pressure, however this model does predict negative dynamic pressure values at 09:00, which are not physically possible.

4.3 Transfer learning model

In an attempt to improve upon the model detailed above, a second model with the same architecture was trained on OMNI data measured at Earth. Utilising the process of transfer learning, where a ML model trained on data from an original domain is applied to data from another related domain, it was intended to increase the accuracy of the model above due to the many years of available in situ solar wind measurements available at Earth.

To determine whether there was a benefit to using the OMNI data would improve the model's predictions, the mean average errors were calculated for this model and the percentage decrease in the mean average error was calculated for each of the solar wind parameters compared with the results of predictions from the model trained only on MAVEN data. The results of this analysis are shown in Figure 4.15. The y and z components of the solar wind velocity and the density showed a small improvement in the accuracy of up to 2% and the dynamic pressure predictions had an accuracy that was increased by 8%. Unfortunately, all three components of the IMF and the x component of the solar wind velocity had a decreased accuracy (between 2% and 6% worse) when

trained on OMNI data, and the difference to the proton temperature predictions was negligible. As such, in this case it was deemed that there was no improvement on using OMNI data to train the model.

4.4 Discussion

This data-driven model has been successful in predicting properties of the solar wind at Mars with good accuracy compared to the physics-based Tao propagation model which is used currently. The Tao model assumes that the solar wind structure is conserved during solar rotation, and as such for periods of variable solar wind conditions the accuracy of this model is decreased. This is noticeable in the second case study presented in this chapter, where the velocity predictions from the Tao model were considerably different from the in situ measurements from MAVEN.

Obvious disadvantages of the model presented in this chapter are that it has no boundaries or restraints to predict only physically possible values, and its usability is limited by its sparse time sampling. Smaller time steps, such as ten minutes, five minutes, or even one minute, would allow the model to be able to produce more complex predictions of the solar wind. However, a more complex model will likely take much longer to train. The training of the main model for this study took 10 hours on a dual core computer, and we might expect that training a model with solar wind average every 10 minutes rather than every 30 would take at least three times as long and possibly over 100 hours. Using a computer cluster would greatly decrease the computational time. For example, the high energy cluster at Lancaster University contains 8,800 cores and so may be able to train this model in a matter of minutes rather than days.

As this model uses input data from both before and after the prediction period (which is not true of SW propagation models) it has the unique possibility to be able to predict the beginning of energetic solar events if only measurements of the end of the event are available and vice versa. However, there are still many amendments to the model which may improve its results. Some possible improvements are detailed in the section below.

4.4.1 Improving the model by integrating physics

In the past few years, models that are hybrids of data driven and physics based models have begun to appear in research in a variety of areas including climate modelling (Kashinath et al., 2021), physical chemistry (Noé et al., 2020) and fluid dynamics (Cai et al., 2021). These physics-informed ML models improve upon traditional ML when applied to physical problems by being more generalisable, and quantifying uncertainties. Methods to introduce physics into ML models include using customised loss functions that penalise unphysical predictions; using customised model architectures (particularly in NNs); embedding suitable symmetries, invariance and equivariance within model inputs outputs; and integrating the frameworks of existing physics-based models into the ML model. These are a range of 'soft' and 'hard' constraints, making the models either heavily biased against unphysical predictions (soft) or incapable of making them (hard).

With regards to this model, using a custom loss function would be a simple adjustment to our model to bias the prediction towards physically possible values. Penalising negative density, temperature and pressure predictions by weighting the loss functions heavily against them would be quick to implement. However, as this is a 'soft' constraint this does not guarantee that unphysical, negative values would never be predicted but rather that they would be less likely. With more effort, additional layers enforcing physical predictions could be added to our model.

The nature of CNNs means they are always equivariant with respect to shift (in this model this corresponds to a time shift of the measured parameters). In this sense, the model in this study already has a physical equivarance embedded within it. A regularly critiqued property of CNNs is that they are not translation invariant. In an image classifying task, this might mean that two similar pictures of the same subject might be differently classified if the subject is in a different portion of the image. For a regression task like the one in this study this is not an issue as the different rows within the input array represent different solar wind properties. For example, measurements of low velocity and measurements of low density would denote different conditions and so it would not be expected that they would produce the same predicted values.

Regarding uncertainty quantification, this study uses the root mean squared error of the test data separated by time step. In practical use of this model, there may not be a test data set and so this method would not be possible. Also, the mean RMSE provides an estimate of only the epistemic uncertainty (the uncertainty caused by the model, similar to the systematic uncertainty) and does not take into account the aleatoric uncertainty (the uncertainty due to the inherently stochastic underlying physical processes of the solar wind (Hüllermeier & Waegeman, 2021). To get a more reliable estimate of the uncertainties associated with this model, fitting multiple models trained on different, smaller portions of the same data would produce a group of models with different predictions for each time step. The epistemic uncertainty could then be estimated from the set of predictions for each parameter and time step. This process is know as bootstrap aggregating or 'bagging' (Caldeira & Nord, 2020), and would be straightforward, although time consuming, to implement. To estimate the aleatoric uncertainty, a similar method can be used adding poise to the input data and quantifying the difference to the predictions.

4.5 Conclusions

- This study acts as a proof-of-concept for the use of artificial neural networks to hindcast solar wind conditions.
- Case studies show that the model can predict solar wind conditions more accurately than the Tao propagation model in some cases.
- Training the model on in situ solar wind data from Earth decreased the accuracy of the model overall. In particular all components of the IMF had decreased prediction accuracy when trained on OMNI data, suggesting that the configuration of the IMF is notably different from Earth by the time it reaches Mars.
- The half hour averaging of the solar wind data causes the model to miss some of the faster periods of variability within the solar wind data. To improve this,

sampling frequency could be increased, however this would mean that the model took longer to train.

- This model could be made more accurate by restricting the predictions to physical values only (i.e. no density measurements below 0).

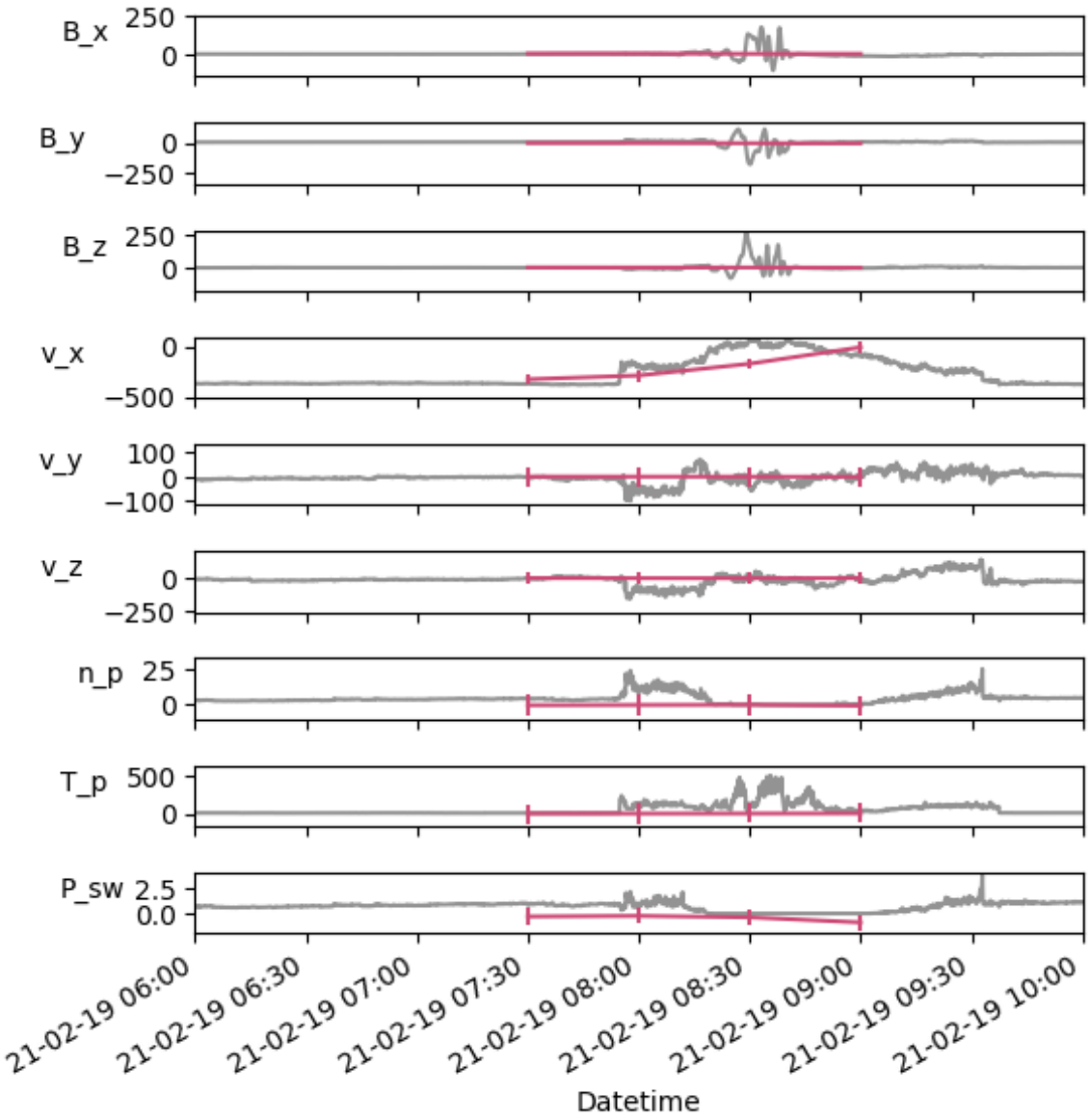

Figure 4.13: Graph showing the values of the magnetic field, velocity, proton density, temperature and dynamic pressure of the solar wind measured by MAVEN on 21 February 2019, shown in grey. Model prediction and errors are overlaid in pink.

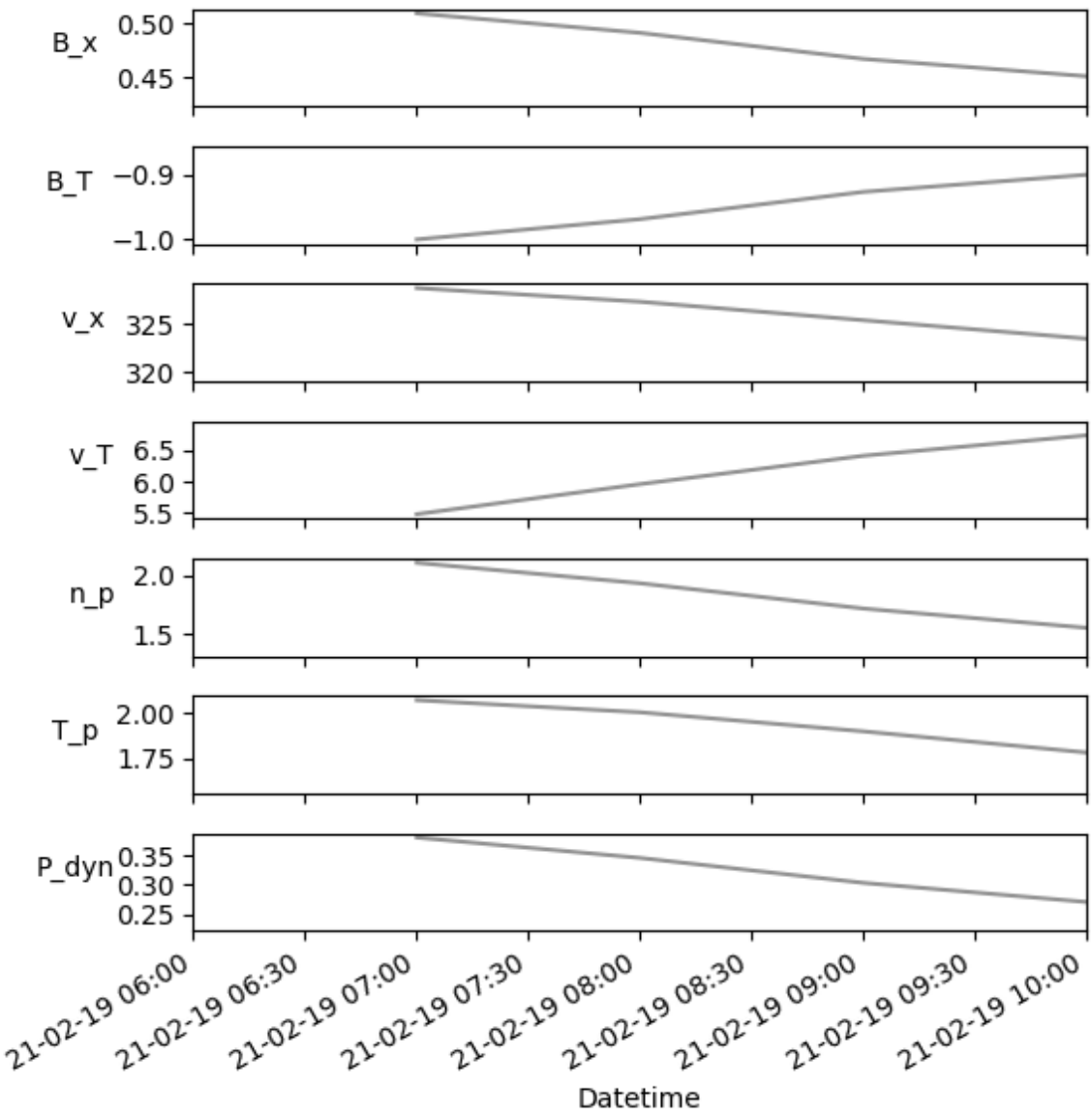

Figure 4.14: Graph showing the solar wind values predicted by the Tao model on 21 February 2019. $B_T = \mathrm{sqrt}(B_y^2 + B_z^2)$, $v_T = \mathrm{sqrt}(v_y^2 + v_z^2)$

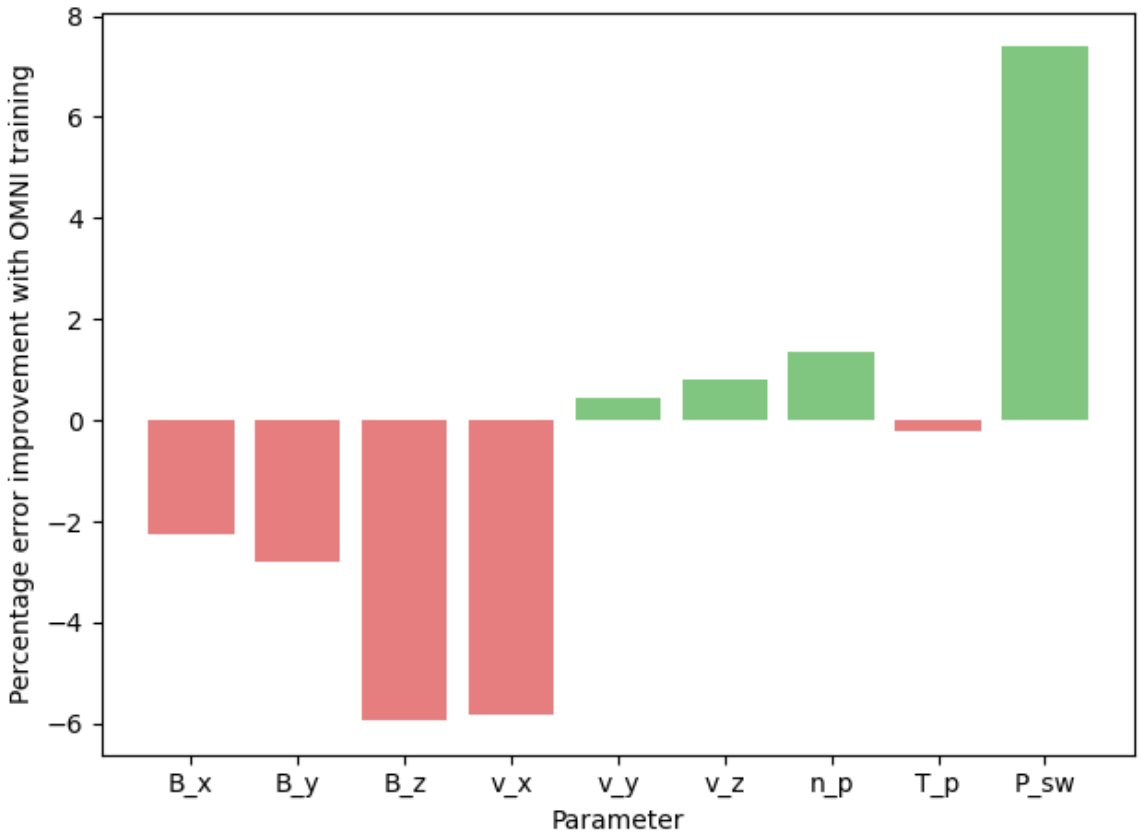

Figure 4.15: Bar graph showing the percentage improvement in the mean average error when training on OMNI data rather than MAVEN. Bars coloured green had a decreased error for the OMNI model compared to the MAVEN model, whereas red bars show parameters that had an increased error when trained on OMNI data compared to MAVEN.

Chapter 5

Interplanetary magnetic field orientation preferences observed by Mars Global Surveyor and MAVEN

The effect of the IMF orientation on the martian magnetosphere has been well researched. Rapid and maintained change of the IMF cone angle, the angle between the IMF orientation and the Sun-Mars line, has been shown to change the orientation of the magnetosphere resulting in large movements in the magnetotail (Romanelli et al., 2018). Changes in field orientation have also been shown to cause twisting of the magnetosphere due to the different reaction times of sections of the magnetosphere (Modolo et al., 2005). The IMF angle also controls the fluctuations of the foreshock. Density and magnetic field strength fluctuations are caused in areas where the IMF direction is normal to the bowshock surface as ions are reflected from or accelerated at the bowshock surface (J. Luhmann & Brace, 1991).

Clearly, the IMF orientation is an important factor in the interaction with the martian magnetosphere, but measurements of the field at this distance from the Sun are scarce. Current models of the IMF at this distance assume it to be steady and slow changing, with the main structure cause by the Parker spiral pattern of towards and away field sectors. These sectors change on average every 13 days (Brain et al., 2005). However, more complex structure within the magnetic field can be caused by energetic events such

as interplanetary coronal mass ejections (ICMEs) and corotating interaction regions (CIRs). In order to better understand how big a role these events play in the solar wind at Mars, a larger and more complete data set of IMF conditions would be needed. A statistical study by D. Liu et al. (2021) calculated the distributions of values of solar wind properties for high and low solar activity levels. Their study found differences between the most frequent values of the solar wind clock angle and cone angle for high and low solar activities. Unusually, this study has chosen to define the cone angle for the range of $0° \leq \theta_{\text{cone}} \leq 360°$ rather than the commonly used range of $0° \leq \theta_{\text{cone}} \leq 180°$.

This study searches for preferences in IMF orientation in measurements representing the typical, 'ambient' solar wind and rarer energetic events. Using Gaussian mixture modelling to group subsets of data with similar properties into clusters, this study investigates the orientations of these clusters to show the typical IMF structure of different data subsets.The interplanetary magnetic field measurements are used to determine the typical orientations of broad types of IMF, including low strength and steady direction, low strength and changing direction and high strength.

5.1 Methods and Data

5.1.1 Data Selection

Magnetometer and spacecraft location data from the Mars Global Surveyor and MAVEN missions have been used in this study. As in other chapters, the Vignes et al. (2000) model of the martian bowshock location was used to remove data collected inside the magnetosphere. Only measurements where all parameters were available are suitable for use in the clustering algorithm, so periods when one or more of the spacecraft's instruments are inactive were removed. This study uses data from September 1997 to March 1999 from the Mars Global Surveyor spacecraft and September 2014 to December 2017 from the MAVEN spacecraft.

5.1.2 Gaussian Mixture Modelling

This study utilises a machine learning technique known as Gaussian mixture modelling; an unsupervised machine learning method where similar data points are grouped together based on their distribution of the points and a number of user-specified parameters. In this study the aim was to find and group similar measurements within the solar wind magnetic field measurements upstream of Mars, to find patterns or similar characteristics within smaller data clusters that might be hidden in an analysis of the entire data set.

Although there are a range of clustering algorithms available, one of the most common is the expectation maximisation (EM) algorithm (Dempster et al., 1977). This is an iterative algorithm which cycles through two steps: expectation and maximisation. During the expectation step, the current model parameters are used to calculate the maximum likelihood estimation for the data (i.e. what is the likelihood that these clusters with given means and variances produced the data we have measured?). The likelihood estimate is similar to a probability density estimate, with a few notable differences. Unlike probability density functions, likelihood functions are not normalised. Also, a likelihood function shows the likeliness of different parameters in your distribution, whereas a probability density function which shows how likely a particular outcome is. In the maximisation step, the model parameters are adjusted to maximise the likelihood for the data. In this application, the speed and efficiency of the EM algorithm, as well as its ability to create clusters with similar centers and a range of shapes, make it a common choice for data clustering over the simpler but more limiting method of k-means clustering (Fraley & Raftery, 1998).

The measurements were clustered based on their cone angle changes and field strengths. Separating measurements by field strength will provide insight into differences in the orientation of the IMF during ambient solar wind conditions and more energetic transient events. Additionally, clustering by the change in the cone angle between two consecutive measurements will differentiate between periods of variable field orientation and steady field orientation. As mentioned in Chapter 3, the primary source of solar wind with cone angles out of the ecliptic plane is energetic events such as CIRs and

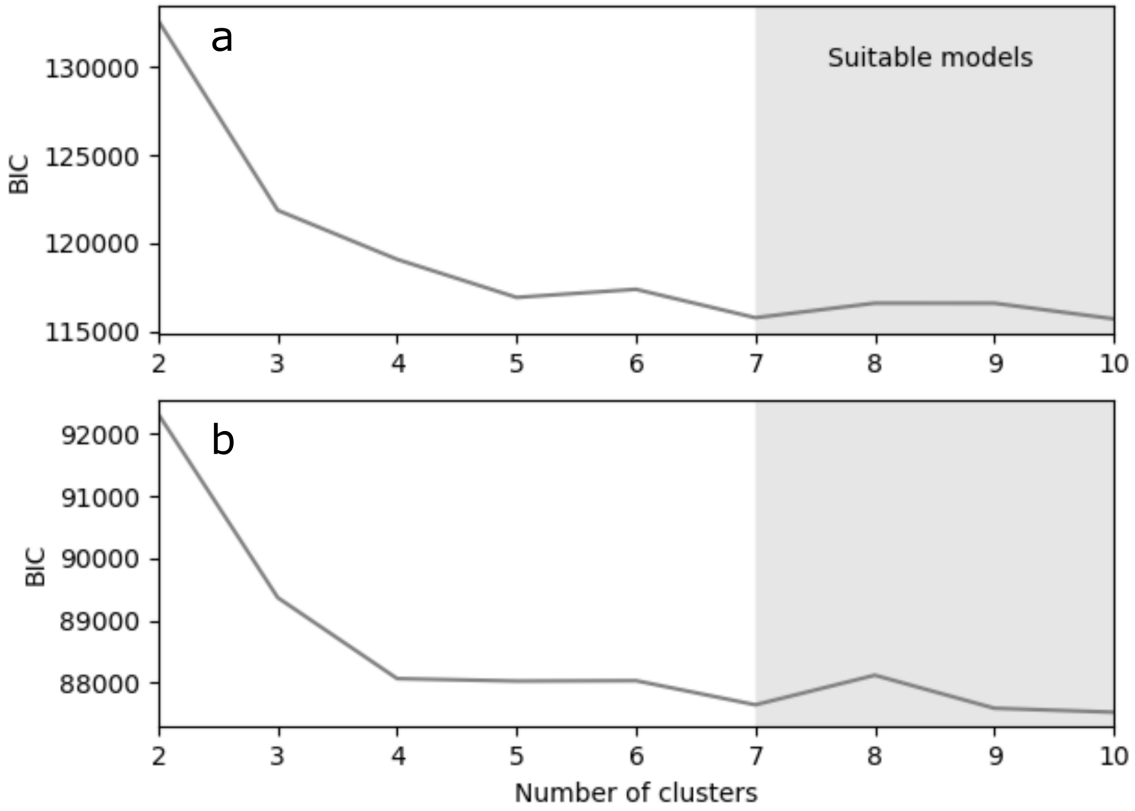

Figure 5.1: Using the Bayesian information criterion (also known as the Schwarz Bayesian information criterion or SBIC) scores of a range models including up to 10 clusters, 7-10 was chosen to be a suitable range to describe the Mars Global Surveyor (panel *a*) and MAVEN (panel *b*) data sets.

ICMEs and so this study will determine if there is a preference in the IMF orientation during these events.

As the Gaussian mixture models with between 2 and 10 components and based on the EM algorithm described above were fitted, and a range of suitable models were chosen. Figure 5.1 shows the Bayesian information criterion (BIC) for these models. In general the BIC is given by

$$BIC = kln(n) - 2ln(\hat{L}) \tag{5.1}$$

where k is the number of parameters estimated by the model, n is the number of data points and $\hat{L}$ is the maximised likelihood function. The BIC can be thought of as a balance between the deviance and the complexity of a model. The term kln(n) describes the complexity of the model, with models that have more estimated parameters having higher values and as such higher BIC scores. The term $2\ln(\hat{L})$ estimates the accuracy of the model, and penalises models that do not describe the observed data well. Low BIC scores suggest the estimated parameters well describe the observed data, and as such are the 'best fit' models for that specific problem. In this case, the BIC scores for models with different numbers of clusters are plotted to find how many clusters are needed to produce a model that describes the observed IMF data well.

The Gaussian mixture modelling technique was chosen because of its speed and simplicity, and because the assumption that each cluster can be well represented by a Gaussian distribution was considered to be well satisfied. Each component had its own general covariance matrix to allow for the maximum possible variation in cluster sizes and orientations. This model is useful in that as well as clustering the data, it also provides the probability that a data point might belong to any of the clusters, which is a useful test of the confidence of fit. Additionally, this model can infer the number of clusters that will provide the best fit given a maximum and prevent overfitting. In this study, the maximum was set to 10, but 7-10 clusters were found to fit both the MGS and MAVEN data sets best. A 7 cluster model was chosen as the best fit model for both data sets. A main issue with this method is the lack of reproducibility of results; because of the random start points of each cluster in this method, the clusters may be placed differently during different runs on the same data set. To improve the reproducibility of this study, the data was clustered three times and only data points that had been assigned to the same cluster on all three runs were used in the analysis. Once the clusters had been identified, subsets of magnetic field measurements were collated for each group, and the orientation of the clusters was investigated using two dimensional histograms showing clock and cone angle measurements. Five degree bins were used for both angles.

5.2 Results

5.2.1 Mars Global Surveyor observations

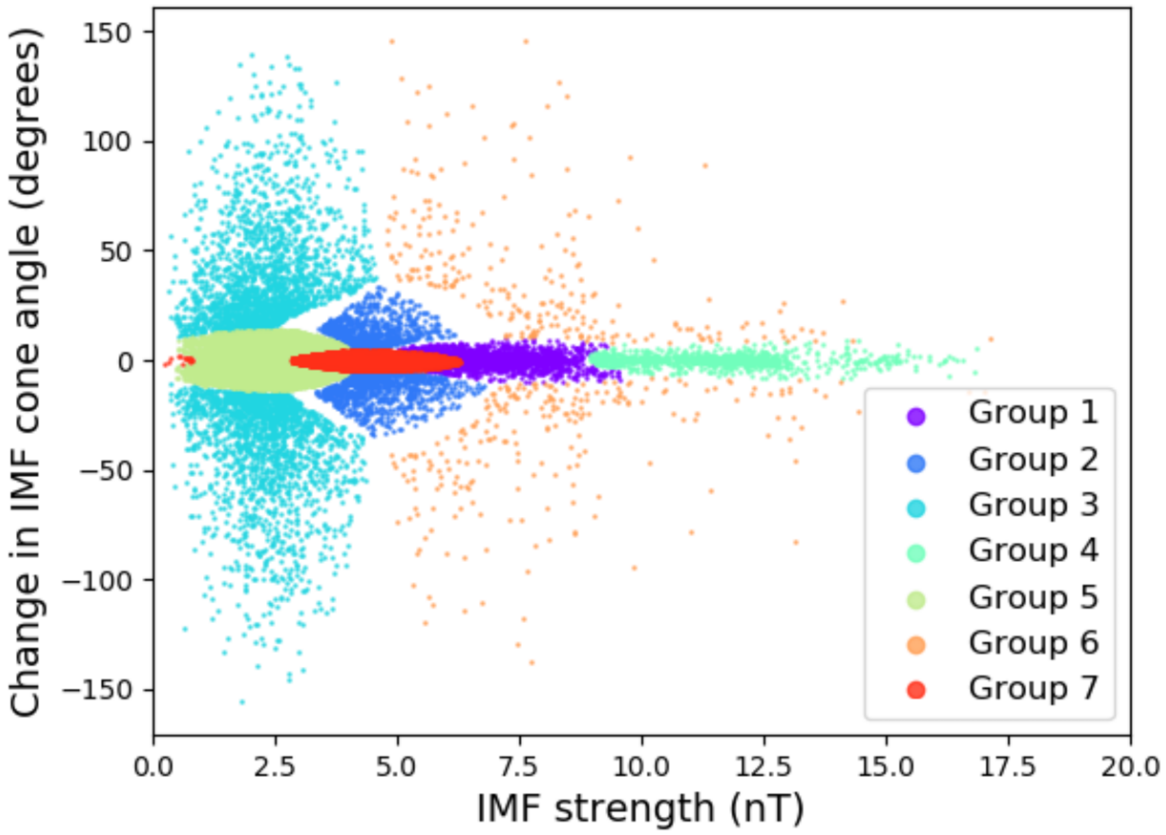

Figure 5.2: The seven clusters identified in the Mars Global Surveyor data based on field strength and cone angle change.

The seven groups in the MGS magnetometer data are shown in Figure 5.2, each shown in a different colour. 27,928 MGS data points were used in the seven clusters, and the number of data points in each cluster is detailed in Figure 5.3, where two dimensional histograms for each of the groups show the frequency of measurements with different IMF orientations in each group. These histograms also state the number of measurements each group is comprised of. The histograms have bin sizes of 10 degrees for both clock angles and cone angles.

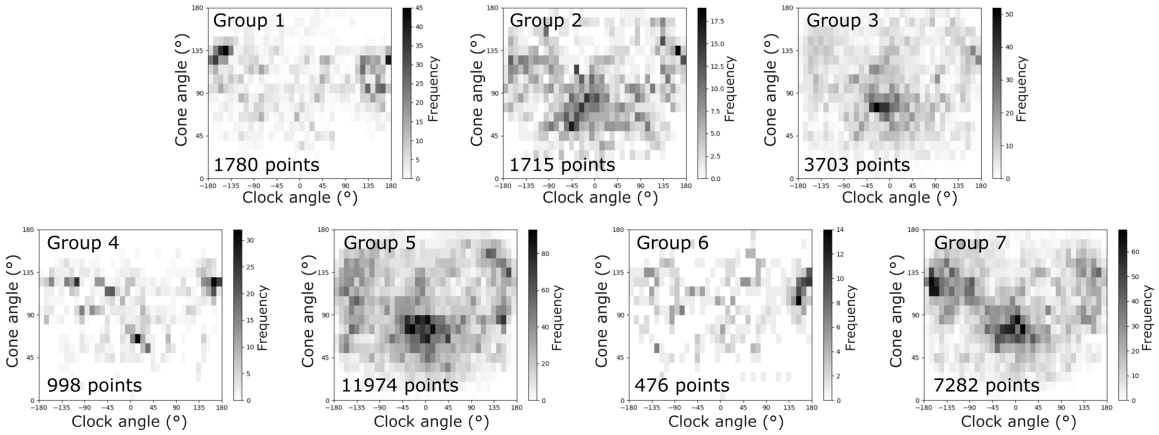

Figure 5.3: Histograms of the orientation of the IMF in the seven MGS clusters.

Groups 1 and 4 contain 6% and 4% of the total data respectively. These clusters both contain measurements with cone angle changes of up to 10 degrees. Group 1 includes measurements with field strengths of between 5 nT and 10 nT while group 4 contains measurements with field stengths between 9 nT and 18 nT. These groups show smaller cone angle ranges from 30 to 150 degrees and both show a peak in clock angle values around 180 degrees.

Group 2 comprises of 6% of the data points and includes measurements with field strengths between 3 and 7 nT and cone angle changes of up to 30 degrees. This group has peaks at clock angles of -20 degrees and 170 degrees and cone angles of 80 degrees and 140 degrees respectively.

Group 3 is comprised of 13% of the data points and has lower field strength values which from 0.3 nT to 4.5 nT. These measurements have cone angles confined between 45 and 135 degrees.

Group 5 is the largest cluster, containing approximately 43% of the total measurements. This cluster is characterised by small cone angle velocities and field strengths of up to 4 nT and can be considered a good representation of the ambient solar wind stream. The

mean IMF orientation of this group has two peaks, one at a cone angle of 70 degrees and a clock angle around 0 degrees, and one with a 110 degree cone angle and a clock angle of 180 degrees. These likely correspond to the towards and away IMF sectors characterised in Brain et al. (2006).

Group 6 is the cluster with the highest cone angle velocities, and magnetic field strengths from 5 nT to 18 nT. This is the smallest of the MGS clusters containing less than 2% of the total measurements. Like group 4, this group shows a smaller distribution of cone angles, with very few measurements taken within 30 degrees of the Mars-Sun line. There is a strong preference for southwards clock angles with a peak in the clock angle values between 160 and 180 degrees and a corresponding peak in cone angle values between 100 degrees and 140 degrees.

Group 7 is the second largest group containing 26% of the total measurements. It contain measurements with field strengths up to 7 nT and very small changes in cone angle of up 10 nT. The IMF orientation histogram for group 7 is similar to group 5, with peaks at a -170 degree clock angle and 120 degree cone angle, and 0 degrees clock angle and 70 degrees cone angle.

5.2.2 MAVEN observations

The seven groups in the MAVEN magnetometer data are shown in Figure 5.4. The MAVEN data totalled 11,232 data points, and the number of data points in each group is shown in Figure 5.5. Unlike the MGS groups, the lower IMF strength measurements have split into separate clusters for positive and negative cone angle changes.

Group 1 contains 16% of the data points and is characterised by low, positive cone angle changes and field strengths of up 5 nT. This group has a strong preference for northwards IMF that is facing towards the Sun at a peak cone angle of 70 degrees.

Group 2 contains 9% of the total measurements. It contains a similar field strenth range of up to 5 nT and cone angle changes between 0 and -15 degrees. The IMF orientations for this group are also very similar to group 1. The main peak in the distribution is

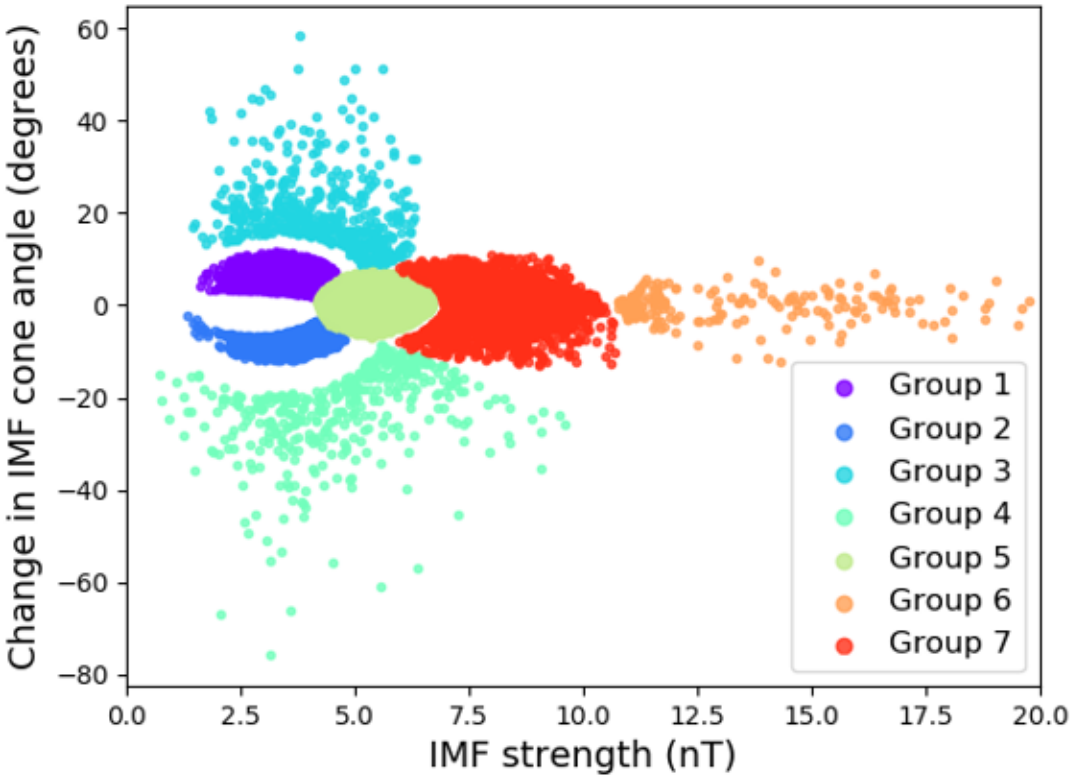

Figure 5.4: The seven clusters identified in the MAVEN data based on field strength and cone angle velocity.

located at a clock angle of 0 degrees and a cone angle of 50 degrees. There is a smaller second peak at -180 degrees clock angle 100 degrees cone angle.

Group 3 contains 4% of the measurements. It is comprised of data points with large cone angle changes, with values reaching up to 60 degrees. This is the most obvious difference between the MGS and MAVEN clusters; the highest cone angle changes for the MGS data reach more than double the highest MAVEN cone angle changes.

Group 4, like group 3, contains points with large cone angle changes. It contains fewer data points (402 compared to 503 for group 3). For this group the changes are negative,

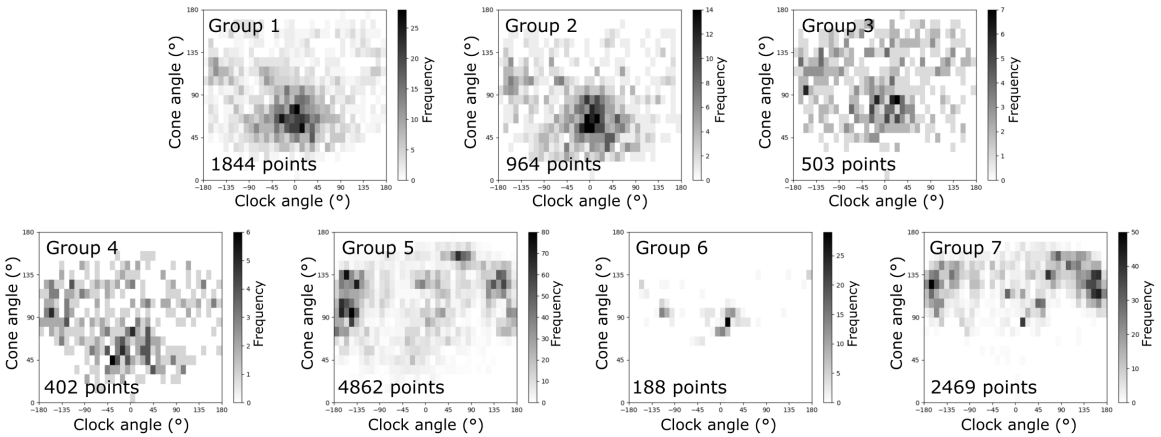

Figure 5.5: Histograms of the orientation of the IMF in the seven MAVEN clusters.

ranging from -75 degrees to -10 degrees and including field strengths between 0 nT and 10 nT. The most frequent IMF orientations have similar clock angles to group 3, however the cone angle values for these peaks seem to be shifted to cone angles approximately 20 degrees lower.

Group 5 is the group containing the largest number of measurements. It contains field strengths between 3.5 nT and cone angle changes of up to 8 degrees. The IMF orientations of this cluster are predominantly southward, with the peak around a clock angle of 0 degrees much less prominent than in groups 1-4. The most common orientation is a clock angle of around -150 degrees and cone angles of 90 degrees and 130 degrees.

Group 6 contains data with the highest field strengths peaking at 18 nT. The cone angle changes for this group are very small, reaching angle changes of only 8 degrees. It is also the smallest group containing less than 2% of the total data. The IMF orientations for this cluster are starkly different to the other groups. All of the measurements have cone angles ranging between 60 degrees and 140 degrees. The most frequent IMF orientation for this group has a clock angle of 20 degrees and a cone angle of 80 degrees. The peak of this distribution is much sharper than those of the other distributions.

Group 7 contains 22% of the available measurements. It contains field strengths between 6 nT and 11 nT, and cone angle changes between -10 degrees and 10 degrees. The data in this cluster have higher cone angles, with very few measurements having cone angles less than 70 degrees. Additionally there is a strong preference for southwards IMF with most of the measurements containing clock angles between -180 degrees and -150 degrees and 140 degrees and 180 degrees.

5.3 Discussion

The clustering method was very effective at identifying measurements with unusually high field strengths and cone angle velocities. In the MGS analysis groups 3, 4 and 5 in particular, which represent the ambient solar wind, periods of high field strength and periods of large cone angle changes respectively, show strong differences in the orientation of the IMF as shown in Figure 5.3. The high field strength measurements in group 4 showed a tighter variation of cone angles near perpendicular to the Sun-Mars line, which is logical as these measurements are likely to correspond to shocks from ICMEs or CIRs and so would be expected to be oriented normal to their direction of movement. However, a comparison of Figures 5.2 and 5.4 shows that the groups with largest changes in cone angle have much higher changes in the MGS data compared to MAVEN. This is the most noticeable change in the cluster distributions. Very little difference is seen in the distribution of the other clusters, which shows that the ambient field does not change significantly with solar season. The difference in the distribution of clusters for MAVEN and MGS mayeb be due to their measurements corresponding to different stages of the solar cycle. As the MGS data covers an increasing period near solar minimum, the solar wind may be comprised proportionally of more 'slow' solar wind which consists of intricate magnetic structures and thus would correspond to a larger proportion of measurements having larger cone angle changes.

5.4 Conclusions

- Both MGS and MAVEN measurements show 7 distinct clusters within the data.
- MAVEN measurements have much smaller cone angle changes than MGS

measurements

- The largest group for the MGS dataset contains low field strengths (up to approximately 4 nT) and small changes in cone angle (up to 10 degrees in either direction).
- The MAVEN dataset's largest group showed similarly small cone angle changes, but higher field strengths between 4 nT and 7 nT.
- Higher field strength clusters are typically associated with periods where the IMF is perpendicular to the Sun-Mars line

Chapter 6

Conclusions

This thesis has presented three studies all providing insight into the upstream solar wind conditions at Mars using modern data science techniques. In this final chapter, the original work from this thesis is summarised and its contribution to the field is discussed. Additionally further work is suggested regarding open questions.

Chapter 3 presented a study that investigated the steadiness of the IMF via autocorrelation analysis of in situ magnetic field measurements in the solar wind. Decorrelation times of IMF observations are calculated and results are compared for measurements taken near solar maximum and minimum to provide some insight into how the steadiness of the field is affected by the solar cycle. The IMF measurements taken by the MGS spacecraft show consistently lower autocorrelation values than the MAVEN spacecraft at the same time lags, showing that the solar wind was steadier during the period of MAVEN measurements for all components of the IMF. This implies that that during solar minimum, the field strength and cone angle of the IMF were much less steady than during solar maximum. It should be noted that these two data sets were taken during different solar cycles; MGS covered the period near the minimum of cycle 23 and MAVEN near the maximum of the much milder cycle 24. Subsets of data based on field strength and cone angle showed noticeable differences in the field strength and clock angle autocorrelation functions, however the cone angle decorrelation time was not affected by field strength or cone angle. This shows that the IMF clock angle is highly variable irrespective of the solar cycle. Especially high field strengths had longer field

strength decorrelation times than mid field strengths, suggesting that during space weather disturbances the field strength is more steady (and therefore more suitable for propagating forward in time during periods where no upstream measurements are available) than during the more common periods of mid field strength. However even then these measurements are decorrelated in less than 2 hours, which does not cover the entire period of an event such as an ICME which could affect the planet for one or multiple days. This result sheds some doubt on how appropriate the commonly used assumption of steady IMF conditions really is in many cases, in contrast to Earth where the steady IMF assumption in more suitable as previous studies have found the decorrelation time to be as long as 25 hours (Borovsky, 2012). All of the decorrelation periods calculated from MAVEN data are shorter than the spacecraft's orbital period, which suggests that it is never suitable to assume that the IMF conditions are steady for case studies using MAVEN data. It seems that very high solar activities are associated with highly variable solar wind, but quiter solar conditions are still found to be notably variable.

The study presented in Chapter 4 described the development of a new data-driven model to estimate solar wind conditions upstream of Mars using direct measurements taken before and after the prediction period. The accuracy of the model was evaluated, and two case studies were presented, showing the actual MAVEN measurements; the predictions of the Tao solar wind propagation model and the predictions of the model introduced in this thesis. For the model in this study to be capable of being compiled in a matter of days rather than weeks or months, the temporal spacing for the measurements was increased to 30 minutes. This was significantly lower than the measurement frequency provided in the MAVEN data, and averaging the data over such long periods loses some of the intricate structure in the solar wind, particularly in the IMF. The use of data with which has a higher temporal frequency would improve the ability of the model to accurately reflect the solar wind conditions. For this significantly more complicated model to be trained in a reasonable amount of time we would advocate for the use of a high end computing cluster, however the relationship between complexity of a model and its training time is not currently clear (Shah & Bhavsar, 2022). Despite the temporal limitations, the case studies presented show that this model can more

accurately predict the solar wind conditions than solar wind propagation models due to the CNN's use of in situ data. This is particularly useful for studies involving ICMEs, where propagation models may not accurately predict the arrival time of these events and so may predict quiet solar wind conditions during these energetic periods.

In Chapter 5, a study investigating the directional preferences of different clusters of IMF measurements using the Gaussian mixture modelling technique was presented. The interplanetary magnetic field was found to be on average steady and with low field strengths around 3 nT, in line with previous studies by Brain et al. (2006) and the work presented in Chapter 3. These measurements show clearly two orientational preferences which correspond with the towards and away sectors of magnetic field consistent with a Parker spiral field configuration, as is observed at Earth. However, measured field strengths stretch up to 18 nT near solar minimum and 20 nT near solar maximum, suggesting that energetic solar events can change the IMF conditions upstream of Mars considerably. High field strengths above 7 nT are confined to cone angles between 45 and 135 degrees. Measurements with large cone angle velocities are observed in both data sets to show a strong preference for 45 degrees for both clock and cone angles.

Limitations of our study stem primarily from the lack of available data. The MGS data set spans only 14 months, and MAVEN only 27 months. Significantly more data would be needed to determine how the IMF behaves over longer timescales, such as how it changes from solar cycle to solar cycle. Another possible issue with this method is that the small and incomplete time window of measurements makes it difficult to generalise the higher field strength measurements. At first look, it may seem reasonable to suggest that the field strengths can double during solar maximum, however, although the number of individual measurements is large the number of events that provide these measurements are unknown. It may be that MGS happened to be inside the magnetosphere during higher field strength events, making the IMF strengths observed during this period look weaker. The longer the observation window and the higher the number of measurements the less likely this situation is.

With MAVEN, the number of possible features to apply this clustering method to is

huge. This method might be used on plasma data to distinguish between interplanetary coronal mass ejections and corotating interaction regions. Magnetic field data that have been shifted into minimum variance coordinates might be used to find flux ropes in the magnetospheric data to allow for more study of the interaction between these structures and crustal fields. Should proxy methods become a more reliable technique for producing estimated IMF measurements, then repeating this analysis with a larger data set would improve confidence in the results of this study.

Limitations aside, the work presented in this thesis has cemented that the view of Mars' plasma environment as static or slow-changing is clearly untrue. The martian magnetosphere is heavily influenced by upstream solar wind conditions, and the results presented in Chapter 3 show that the upstream IMF is highly variable even during quiet solar conditions. The highest IMF strengths observed by MAVEN have the shortest cone angle decorrelation times, showing energetic solar wind events to have highly variable magnetic fields as might be expected in structures such as magnetic clouds. These high field strengths are known to allow the IMF to push into the magnetosphere and allow direct interactions between the IMF and crustal fields, which can result in bulk loss of atmospheric plasma. These results show that the upstream conditions during periods of extremely high field strengths are ideal for facilitating this type of bulk ionospheric loss. The data-driven model presented in Chapter 4 demonstrates the application of CNN models to predicting solar wind conditions. It performed better than a popular solar wind propagation model during a period of turbulent solar wind conditions. The case studies demonstrate that Sudden and sustained changes in the clock angle direction can result in dramatic changes the magnetosphere, displacing the magnetopause as much as $1R_E$ (Dušík et al., 2010), and the clusters found in Chapter 5 show that these large angular changes are regularly observed, with consecutive measurements having an angular difference of more than ten degrees in 15% of MGS measurements (4179 out of 27928 total) and 8% of MAVEN measurements (905 out of 11232 total) used in this study. At the very least, this thesis has demonstrated that the assumption that the solar wind conditions are constant on a timescale of hours is unsuitable and should not be used when analysing data for future Mars missions. Instead, future researchers may want to utilise a ML model of some sort, such as the

one presented in Chapter 4.

6.1 Future Work

One of the most obvious areas for future work will be to repeat these studies once MAVEN has taken measurements spanning a complete solar cycle. This will provide a more accurate analysis of the solar cycle's effect on the IMF variability and remove the uncertainty of comparing measurements from different solar cycles and spacecrafts. Additionally, expanding the study presented in Chapter 3 to investigate the variability of other solar wind parameters including density and speed would be insightful.

Using measurements that cover the entirety of the solar cycle to train and test the CNN model presented in Chapter 4 would provide (in theory) more accurate model predictions, as well as testing results that better reflect how the model would perform whilst predicting measurements during a wide range of solar conditions.

The clustering study presented in Chapter 5 presents results on the IMF orientation preferences during steady and fast-changing cone angles. However, it would be interesting to see how the clustering method could be used to group solar wind measurements based on more measured properties of the solar wind such as dynamic pressure and proton density. This could be investigated using dimensionality reduction techniques such as principle component analysis or using an autoencoder.

Beyond the work suggested above, all of the techniques used within this thesis could be applied to other planets in the solar system without the luxury of upstream solar wind monitors. In particular, the hindcasting model presented in Chapter 4 could be used not only to provide more context in case studies at other planets but also for studies of comet 67P/Churyumov–Gerasimenko where the Rosetta spacecraft is in orbit and passes through the comet's induced magnetosphere.

Appendix A

Additional figures showing polynomial fits of autocorrelation values

This appendix contains additional figures for Chapter 3, showing the calculated autocorrelation values and the polynomial lines of best fit for each measurement period and component of the IMF.

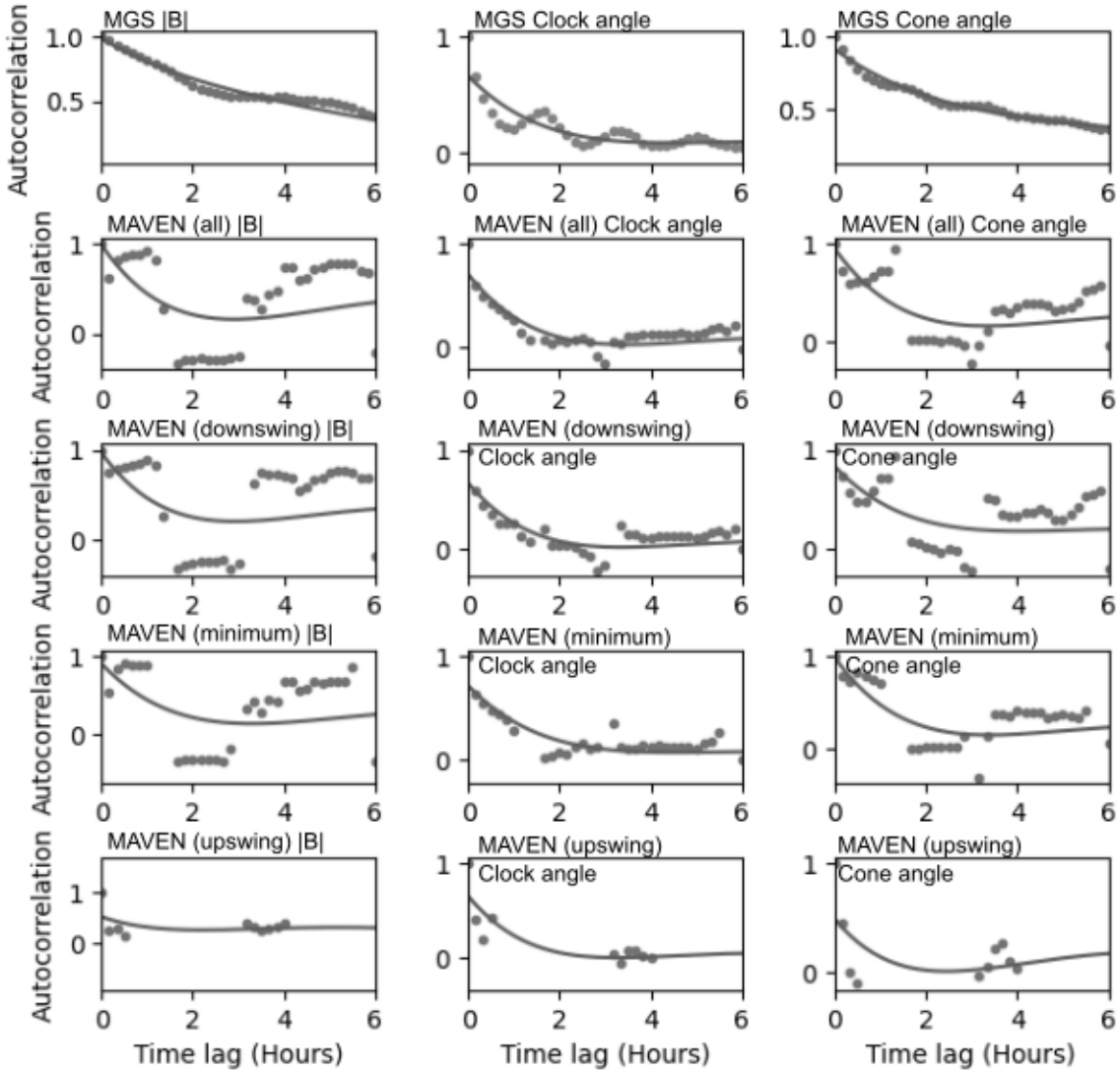

Figure A.1: Graph showing the autocorrelation functions of IMF strength, clock angle and cone angle measurements at varying time lags taken by MGS and MAVEN for the total MAVEN data set and for periods of decreasing, minimum and increasing solar activity. Calculated autocorrelation values are shown as individual points. The polynomial line of best fit is also plotted.

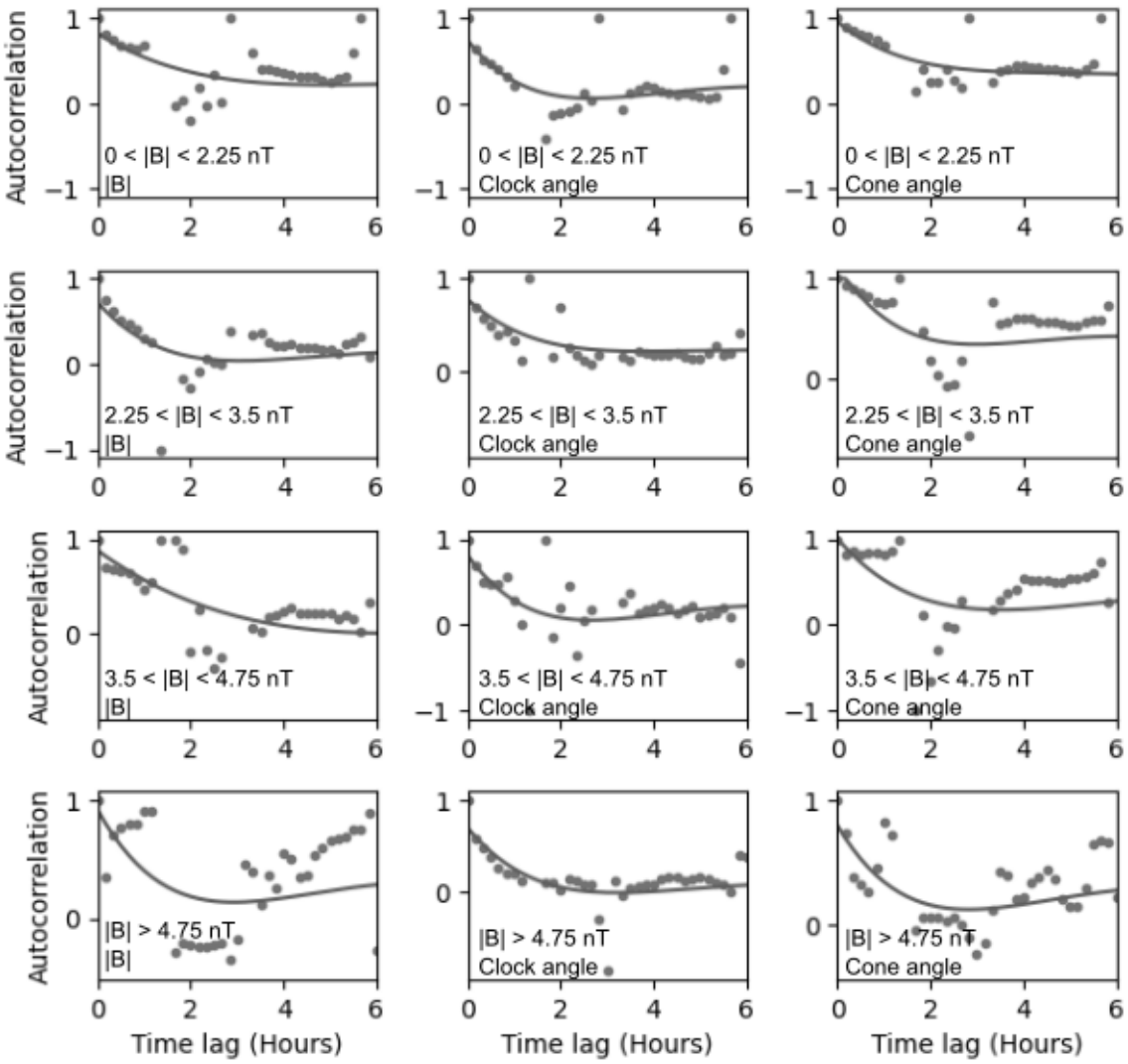

Figure A.2: Graph showing the autocorrelation functions of IMF strength, clock angle and cone angle measurements at varying time lags taken by MAVEN for periods of low, medium, high and extra high field strengths. Calculated autocorrelation values are shown as individual points. The polynomial line of best fit is also plotted.

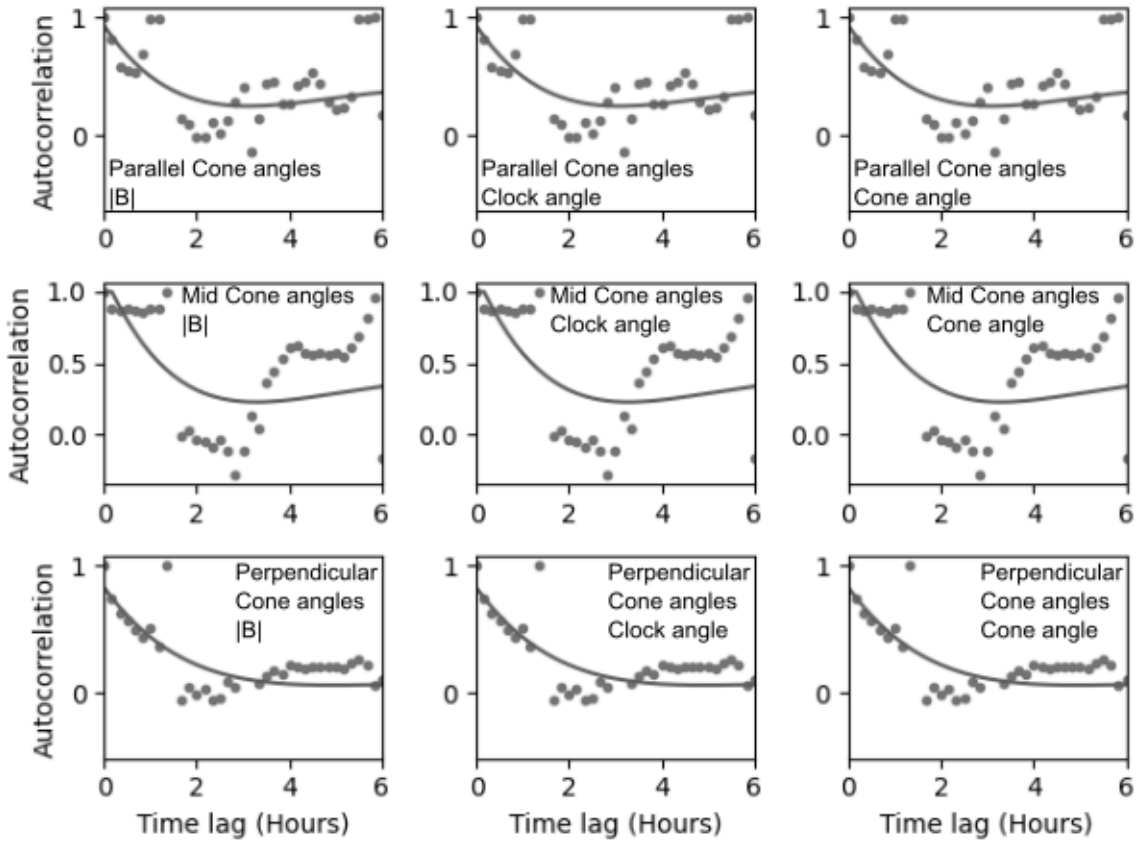

Figure A.3: Graph showing the autocorrelation functions of IMF strength, clock angle and cone angle measurements at varying time lags taken by MAVEN for periods of IMF orientation in, near and out of the ecliptic plane. Calculated autocorrelation values are shown as individual points. The polynomial line of best fit is also plotted.

Bibliography

Abramson, N., Braverman, D., & Sebestyen, G. (1963). Pattern recognition and machine learning [Conference Name: IEEE Transactions on Information Theory]. *IEEE Transactions on Information Theory*, *9*(4), 257–261. https://doi.org/10.1109/TIT.1963.1057854

Acuna, M. H., Connerney, J. E. P., Wasilewski, P., Lin, R. P., Anderson, K. A., Carlson, C. W., McFadden, J., Curtis, D. W., Mitchell, D., Reme, H., Mazelle, C., Sauvaud, J. A., d'Uston, C., Cros, A., Medale, J. L., Bauer, S. J., Cloutier, P., Mayhew, M., Winterhalter, D., & Ness, N. F. (1998). Magnetic field and plasma observations at Mars: Initial results of the Mars global surveyor mission [WOS:000072490000044]. *Science*, *279*(5357), 1676–1680. https://doi.org/10.1126/science.279.5357.1676

Acuna, M. H., Connerney, J. E. P., Wasilewski, P., Lin, R. P., Mitchell, D., Anderson, K. A., Carlson, C. W., McFadden, J., Reme, H. R., Mazelle, C., Vignes, D., Bauer, S. J., Cloutier, P., & Ness, N. F. (2001). Magnetic field of Mars: Summary of results from the aerobraking and mapping orbits [WOS:000171925900015]. *Journal of Geophysical Research-Planets*, *106*(E10), 23403–23417. https://doi.org/10.1029/2000JE001404

Ahmed, N. K., Atiya, A. F., Gayar, N. E., & El-Shishiny, H. (2010). An Empirical Comparison of Machine Learning Models for Time Series Forecasting [Publisher: Taylor & Francis _eprint: https://doi.org/10.1080/07474938.2010.481556]. *Econometric Reviews*, *29*(5-6), 594–621. https://doi.org/10.1080/07474938.2010.481556

Albee, A. L., Arvidson, R. E., Palluconi, F., & Thorpe, T. (2001). Overview of the Mars Global Surveyor mission [Place: Washington Publisher: Amer Geophysical Union

WOS:000171925900009]. *Journal of Geophysical Research-Planets*, *106*(E10), 23291–23316. https://doi.org/10.1029/2000JE001306

Albee, A. L., Palluconi, F. D., & Arvidson, R. E. (1998). Mars global surveyor mission: Overview and status. *Science (New York, N.Y.)*, *279*(5357), 1671–1672. https://doi.org/10.1126/science.279.5357.1671

Andersson, L., Ergun, R. E., Delory, G. T., Eriksson, A., Westfall, J., Reed, H., McCauly, J., Summers, D., & Meyers, D. (2015). The Langmuir Probe and Waves (LPW) Instrument for MAVEN [Place: Dordrecht Publisher: Springer WOS:000365729700007]. *Space Science Reviews*, *195*(1-4), 173–198. https://doi.org/10.1007/s11214-015-0194-3

Ballester, J. L., Oliver, R., & Carbonell, M. (2002). The Near 160 Day Periodicity in the Photospheric Magnetic Flux [Publisher: IOP Publishing]. *The Astrophysical Journal*, *566*(1), 505. https://doi.org/10.1086/338075

Barabash, S., Fedorov, A., Lundin, R., & Sauvaud, J.-A. (2007). Martian atmospheric erosion rates. *Science (New York, N.Y.)*, *315*(5811), 501–503. https://doi.org/10.1126/science.1134358

Bartoletti, M., Pes, B., & Serusi, S. (2018). *Data mining for detecting Bitcoin Ponzi schemes* [Pages: 75-84 Publication Title: 2018 Crypto Valley Conference on Blockchain Technology (cvcbt) WOS:000466595100009]. Ieee. https://doi.org/10.1109/CVCBT.2018.00014

Benna, M., Mahaffy, P. R., Grebowsky, J. M., Fox, J. L., Yelle, R. V., & Jakosky, B. M. (2015). First measurements of composition and dynamics of the Martian ionosphere by MAVEN's Neutral Gas and Ion Mass Spectrometer [_eprint: https://agupubs.onlinelibrary.wiley.com/doi/pdf/10.1002/2015GL066146]. *Geophysical Research Letters*, *42*(21), 8958–8965. https://doi.org/10.1002/2015GL066146

Benna, M., Anderson, B. J., Baker, D. N., Boardsen, S. A., Gloeckler, G., Gold, R. E., Ho, G. C., Killen, R. M., Korth, H., Krimigis, S. M., Purucker, M. E., McNutt, R. L., Raines, J. M., McClintock, W. E., Sarantos, M., Slavin, J. A., Solomon, S. C., & Zurbuchen, T. H. (2010). Modeling of the Magnetosphere of Mercury at the Time of the First MESSENGER Flyby [NTRS Author Affiliations: NASA Goddard Space Flight Center, Johns Hopkins Univ., Colorado Univ., Michigan

Univ., Carnegie Institution of Washington NTRS Report/Patent Number: GSFC.JA.4602.2011 NTRS Document ID: 20110013540 NTRS Research Center: Goddard Space Flight Center (GSFC)]. *Icarus*, *209*. https://doi.org/10.1016/j.icarus.2009.11.036

Bertucci, C., Mazelle, C., & Acuna, M. (2005). Structure and variability of the Martian magnetic pileup boundary and bow shock from MGS MAG/ER observations [Conference Name: 35th COSPAR Scientific Assembly ISSN: 0273-1177 Issue: 11 Num Pages: 11 Series Title: ADVANCES IN SPACE RESEARCH-SERIES Web of Science ID: WOS:000235252300006]. In O. Witasse & M. A. Shea (Eds.), *PLANETARY ATMOSPHERES, IONOSPHERES, AND MAGNETOSPHERES* (pp. 2066–2076). Elsevier Science Ltd. https://doi.org/10.1016/j.asr.2005.05.096

Bertucci, C., Mazelle, C., Crider, D. H., Mitchell, D. L., Sauer, K., Acuña, M. H., Connerney, J. E. P., Lin, R. P., Ness, N. F., & Winterhalter, D. (2004). MGS MAG/ER observations at the magnetic pileup boundary of Mars: Draping enhancement and low frequency waves. *Advances in Space Research*, *33*(11), 1938–1944. https://doi.org/10.1016/j.asr.2003.04.054

Bertucci, C., Mazelle, C., Crider, D. H., Vignes, D., Acuña, M. H., Mitchell, D. L., Lin, R. P., Connerney, J. E. P., Rème, H., Cloutier, P. A., Ness, N. F., & Winterhalter, D. (2003). Magnetic field draping enhancement at the Martian magnetic pileup boundary from Mars global surveyor observations [_eprint: https://onlinelibrary.wiley.com/doi/pdf/10.1029/2002GL015713]. *Geophysical Research Letters*, *30*(2). https://doi.org/10.1029/2002GL015713

Bittencourt, J. A. (2004). *Fundamentals of Plasma Physics*. Springer Science & Business Media.

Boldyrev, S., Loureiro, N. F., & Roytershteyn, V. (2021). Plasma Dynamics in Low-Electron-Beta Environments. *Frontiers in Astronomy and Space Sciences*, *8*. https://doi.org/10.3389/fspas.2021.621040

Borovsky, J. E. (2012). The velocity and magnetic field fluctuations of the solar wind at 1 AU: Statistical analysis of Fourier spectra and correlations with plasma properties. *Journal of Geophysical Research: Space Physics*, *117*(A5). https://doi.org/10.1029/2011JA017499

Bougher, S. W., Engel, S., Hinson, D. P., & Forbes, J. M. (2001). Mars Global Surveyor Radio Science electron density profiles: Neutral atmosphere implications [WOS:000170348100008]. *Geophysical Research Letters*, *28*(16), 3091–3094. https://doi.org/10.1029/2001GL012884

Bougher, S. W., Pawlowski, D., Bell, J. M., Nelli, S., McDunn, T., Murphy, J. R., Chizek, M., & Ridley, A. (2015). Mars Global Ionosphere-Thermosphere Model: Solar cycle, seasonal, and diurnal variations of the Mars upper atmosphere [WOS:000351363300010]. *Journal of Geophysical Research-Planets*, *120*(2), 311–342. https://doi.org/10.1002/2014JE004715

Box, G. E. P., Jenkins, G. M., Reinsel, G. C., & Ljung, G. M. (2015). *Time Series Analysis: Forecasting and Control* [Google-Books-ID: rNt5CgAAQBAJ]. John Wiley & Sons.

Brain, D. A. (2007). Mars Global Surveyor Measurements of the Martian Solar Wind Interaction. In C. T. Russell (Ed.), *The Mars Plasma Environment* (pp. 77–112). Springer. https://doi.org/10.1007/978-0-387-70943-7_5

Brain, D. A., Bagenal, F., Acuña, M. H., & Connerney, J. E. P. (2003). Martian magnetic morphology: Contributions from the solar wind and crust. *Journal of Geophysical Research: Space Physics*, *108*(A12), 1424. https://doi.org/10.1029/2002JA009482

Brain, D. A., Baker, A. H., Briggs, J., Eastwood, J. P., Halekas, J. S., & Phan, T.-D. (2010). Episodic detachment of Martian crustal magnetic fields leading to bulk atmospheric plasma escape. *Geophysical Research Letters*, *37*(14). https://doi.org/10.1029/2010GL043916

Brain, D. A., Halekas, J. S., Lillis, R., Mitchell, D. L., Lin, R. P., & Crider, D. H. (2005). Variability of the altitude of the Martian sheath [WOS:000232177700001]. *Geophysical Research Letters*, *32*(18), L18203. https://doi.org/10.1029/2005GL023126

Brain, D. A., Mitchell, D. L., & Halekas, J. S. (2006). The magnetic field draping direction at Mars from April 1999 through August 2004. *Icarus*, *182*(2), 464–473. https://doi.org/10.1016/j.icarus.2005.09.023

Brecht, S. H., & Ledvina, S. A. (2006). The Solar Wind Interaction With the Martian Ionosphere/Atmosphere. *Space Science Reviews*, *126*(1), 15–38. https://doi.org/10.1007/s11214-006-9084-z

Burlaga, L. F., Skoug, R. M., Smith, C. W., Webb, D. F., Zurbuchen, T. H., & Reinard, A. (2001). Fast ejecta during the ascending phase of solar cycle 23: ACE observations, 1998–1999 [_eprint: https://onlinelibrary.wiley.com/doi/pdf/10.1029/2000JA000214]. *Journal of Geophysical Research: Space Physics*, *106*(A10), 20957–20977. https://doi.org/10.1029/2000JA000214

Cai, S., Wang, Z., Wang, S., Perdikaris, P., & Karniadakis, G. E. (2021). Physics-Informed Neural Networks for Heat Transfer Problems. *Journal of Heat Transfer*, *143*(060801). https://doi.org/10.1115/1.4050542

Caldeira, J., & Nord, B. (2020). Deeply uncertain: Comparing methods of uncertainty quantification in deep learning algorithms [Publisher: IOP Publishing]. *Machine Learning: Science and Technology*, *2*(1), 015002. https://doi.org/10.1088/2632-2153/aba6f3

Carr, M. H., & Head, J. W. (2010). Geologic history of Mars. *Earth and Planetary Science Letters*, *294*(3), 185–203. https://doi.org/10.1016/j.epsl.2009.06.042

Chaffin, M. S., Chaufray, J. Y., Deighan, J., Schneider, N. M., Mayyasi, M., Clarke, J. T., Thiemann, E., Jain, S. K., Crismani, M. M. J., Stiepen, A., Eparvier, F. G., McClintock, W. E., Stewart, A. I. F., Holsclaw, G. M., Montmessin, F., & Jakosky, B. M. (2018). Mars H Escape Rates Derived From MAVEN/IUVS Lyman Alpha Brightness Measurements and Their Dependence on Model Assumptions. *Journal of Geophysical Research: Planets*, *123*(8), 2192–2210. https://doi.org/10.1029/2018JE005574

Choi, C., Kim, J., Kim, J., & Kim, H. S. (2019). Development of Combined Heavy Rain Damage Prediction Models with Machine Learning [Place: Basel Publisher: Mdpi WOS:000507378600089]. *Water*, *11*(12), 2516. https://doi.org/10.3390/w11122516

Choubin, B., Borji, M., Mosavi, A., Sajedi-Hosseini, F., Singh, V. P., & Shamshirband, S. (2019). Snow avalanche hazard prediction using machine learning methods [Place: Amsterdam Publisher: Elsevier WOS:000488304300008]. *Journal of Hydrology*, *577*, 123929. https://doi.org/10.1016/j.jhydrol.2019.123929

Christensen, P. R., Bandfield, J. L., Hamilton, V. E., Ruff, S. W., Kieffer, H. H., Titus, T. N., Malin, M. C., Morris, R. V., Lane, M. D., Clark, R. L., Jakosky, B. M., Mellon, M. T., Pearl, J. C., Conrath, B. J., Smith, M. D., Clancy, R. T., Kuzmin, R. O., Roush, T., Mehall, G. L., ... Greenfield, M. (2001). Mars Global Surveyor Thermal Emission Spectrometer experiment: Investigation description and surface science results [_eprint: https://onlinelibrary.wiley.com/doi/pdf/10.1029/2000JE001370]. *Journal of Geophysical Research: Planets*, *106*(E10), 23823–23871. https://doi.org/10.1029/2000JE001370

Cloutier, P. A., Daniell, R. E., & Butler, D. M. (1974). Atmospheric ion wakes of Venus and Mars in the solar wind. *Planetary and Space Science*, *22*(6), 967–990. https://doi.org/10.1016/0032-0633(74)90166-4

Connerney, J. E. P., Acuña, M. H., Wasilewski, P. J., Ness, N. F., Rème, H., Mazelle, C., Vignes, D., Lin, R. P., Mitchell, D. L., & Cloutier, P. A. (1999). Magnetic Lineations in the Ancient Crust of Mars. *Science*, *284*(5415), 794–798. https://doi.org/10.1126/science.284.5415.794

Connerney, J. E. P., Espley, J., Lawton, P., Murphy, S., Odom, J., Oliversen, R., & Sheppard, D. (2015). The MAVEN Magnetic Field Investigation. *Space Science Reviews*, *195*(1), 257–291. https://doi.org/10.1007/s11214-015-0169-4

Cranmer, S. R. (2005). Why is the Fast Solar Wind Fast and the Slow Solar Wind Slow? A Survey of Geometrical Models [arXiv: astro-ph/0506508]. *arXiv:astro-ph/0506508*.

Cravens, T. E., Rahmati, A., Fox, J. L., Lillis, R., Bougher, S., Luhmann, J., Sakai, S., Deighan, J., Lee, Y., Combi, M., & Jakosky, B. (2017). Hot oxygen escape from Mars: Simple scaling with solar EUV irradiance [WOS:000395655800077]. *Journal of Geophysical Research-Space Physics*, *122*(1), 1102–1116. https://doi.org/10.1002/2016JA023461

Cruz, J. A., & Wishart, D. S. (2006). Applications of Machine Learning in Cancer Prediction and Prognosis [Publisher: SAGE Publications Ltd STM]. *Cancer Informatics*, *2*, 117693510600200030. https://doi.org/10.1177/117693510600200030

Curry, S. M., Luhmann, J., Ma, Y., Liemohn, M., Dong, C., & Hara, T. (2015). Comparative pick-up ion distributions at Mars and Venus: Consequences for

atmospheric deposition and escape. *Planetary and Space Science*, *115*, 35–47. https://doi.org/10.1016/j.pss.2015.03.026

Dahl, G. E., Sainath, T. N., & Hinton, G. E. (2013). Improving deep neural networks for LVCSR using rectified linear units and dropout [ISSN: 2379-190X]. *2013 IEEE International Conference on Acoustics, Speech and Signal Processing*, 8609–8613. https://doi.org/10.1109/ICASSP.2013.6639346

Dandouras, I., Blanc, M., Fossati, L., Gerasimov, M., Guenther, E., Kislyakova, K., Lammer, H., Lin, Y., Marty, B., Mazelle, C., Rugheimer, S., Scherf, M., Sotin, C., Sproß, L., Tachibana, S., Wurz, P., & Yamauchi, M. (2020). Future Missions Related to the Determination of the Elemental and Isotopic Composition of Earth, Moon and the Terrestrial Planets. *Space Science Reviews*, *216*, 121. https://doi.org/10.1007/s11214-020-00736-0

Dempster, A. P., Laird, N. M., & Rubin, D. B. (1977). Maximum likelihood from incomplete data via the EM algorithm. *Journal of the Royal Statistical Society, Series B*, *39*(1), 1–38.

DiBraccio, G. A., Espley, J. R., Gruesbeck, J. R., Connerney, J. E. P., Brain, D. A., Halekas, J. S., Mitchell, D. L., McFadden, J. P., Harada, Y., Livi, R., Collinson, G., Hara, T., Mazelle, C., & Jakosky, B. M. (2015). Magnetotail dynamics at Mars: Initial MAVEN observations. *Geophysical Research Letters*, *42*(21), 8828–8837. https://doi.org/10.1002/2015GL065248

Dieval, C., Morgan, D. D., Nemec, F., & Gurnett, D. A. (2014). MARSIS observations of the Martian nightside ionosphere dependence on solar wind conditions [WOS:000337622100060]. *Journal of Geophysical Research-Space Physics*, *119*(5), 4077–4093. https://doi.org/10.1002/2014JA019788

Dong, Y., Fang, X., Brain, D. A., McFadden, J. P., Halekas, J. S., Connerney, J. E., Curry, S. M., Harada, Y., Luhmann, J. G., & Jakosky, B. M. (2015). Strong plume fluxes at Mars observed by MAVEN: An important planetary ion escape channel [_eprint: https://onlinelibrary.wiley.com/doi/pdf/10.1002/2015GL065346]. *Geophysical Research Letters*, *42*(21), 8942–8950. https://doi.org/10.1002/2015GL065346

Dong, Y., Fang, X., Brain, D. A., McFadden, J. P., Halekas, J. S., Connerney, J. E. P., Eparvier, F., Andersson, L., Mitchell, D., & Jakosky, B. M. (2017). Seasonal vari-

ability of Martian ion escape through the plume and tail from MAVEN observations [_eprint: https://onlinelibrary.wiley.com/doi/pdf/10.1002/2016JA023517]. *Journal of Geophysical Research: Space Physics*, *122*(4), 4009–4022. https://doi.org/10.1002/2016JA023517

Dubinin, E., Fraenz, M., Pätzold, M., McFadden, J., Halekas, J. S., Connerney, J. E. P., Jakosky, B. M., Vaisberg, O., & Zelenyi, L. (2018). Martian ionosphere observed by MAVEN. 3. Influence of solar wind and IMF on upper ionosphere. *Planetary and Space Science*, *160*, 56–65. https://doi.org/10.1016/j.pss.2018.03.016

Dubinin, E., Fraenz, M., Pätzold, M., McFadden, J., Halekas, J. S., DiBraccio, G. A., Connerney, J. E. P., Eparvier, F., Brain, D., Jakosky, B. M., Vaisberg, O., & Zelenyi, L. (2017). The Effect of Solar Wind Variations on the Escape of Oxygen Ions From Mars Through Different Channels: MAVEN Observations [_eprint: https://onlinelibrary.wiley.com/doi/pdf/10.1002/2017JA024741]. *Journal of Geophysical Research: Space Physics*, *122*(11), 11, 285–11, 301. https://doi.org/10.1002/2017JA024741

Dubinin, E., Franz, M., Woch, J., Roussos, E., Barabash, S., Lundin, R., Winningham, J. D., Frahm, R. A., & Acuna, M. (2006). Plasma morphology at mars. Aspera-3 observations [Place: Dordrecht Publisher: Springer WOS:000245889300009]. *Space Science Reviews*, *126*(1-4), 209–238. https://doi.org/10.1007/s11214-006-9039-4

Dušík, Š., Granko, G., Šafránková, J., Němeček, Z., & Jelínek, K. (2010). IMF cone angle control of the magnetopause location: Statistical study: CONE ANGLE AND MAGNETOPAUSE LOCATION. *Geophysical Research Letters*, *37*(19), n/a–n/a. https://doi.org/10.1029/2010GL044965

Fang, X., Liemohn, M. W., Nagy, A. F., Ma, Y., De Zeeuw, D. L., Kozyra, J. U., & Zurbuchen, T. H. (2008). Pickup oxygen ion velocity space and spatial distribution around Mars [_eprint: https://onlinelibrary.wiley.com/doi/pdf/10.1029/2007JA012736]. *Journal of Geophysical Research: Space Physics*, *113*(A2). https://doi.org/10.1029/2007JA012736

Fang, X., Ma, Y., Luhmann, J., Dong, Y., Brain, D., Hurley, D., Dong, C., Lee, C. O., & Jakosky, B. (2018). The Morphology of the Solar Wind Magnetic Field Draping

on the Dayside of Mars and Its Variability [WOS:000435745500006]. *Geophysical Research Letters*, *45*(8), 3356–3365. https://doi.org/10.1002/2018GL077230

Fox, J. (1993). The Production and Escape of Nitrogen-Atoms on Mars [WOS:A1993KX58700018]. *Journal of Geophysical Research-Planets*, *98*(E2), 3297–3310. https://doi.org/10.1029/92JE02289

Fraley, C., & Raftery, A. E. (1998). How Many Clusters? Which Clustering Method? Answers Via Model-Based Cluster Analysis. *The Computer Journal*, *41*(8), 578–588. https://doi.org/10.1093/comjnl/41.8.578

Friedberg, R. M. (1958). A Learning Machine: Part I [Conference Name: IBM Journal of Research and Development]. *IBM Journal of Research and Development*, *2*(1), 2–13. https://doi.org/10.1147/rd.21.0002

Ganapathiraju, A., Hamaker, J. E., & Picone, J. (2004). Applications of support vector machines to speech recognition [Place: Piscataway Publisher: Ieee-Inst Electrical Electronics Engineers Inc WOS:000222760500018]. *Ieee Transactions on Signal Processing*, *52*(8), 2348–2355. https://doi.org/10.1109/TSP.2004.831018

Gentile, M. C., Danks, D., & Harrell, M. (2022). Case Study: Does Facial Recognition Tech Enhance Security? [Section: Business and society]. *Harvard Business Review*.

Girazian, Z., Mahaffy, P. R., Lillis, R. J., Benna, M., Elrod, M., & Jakosky, B. M. (2017). Nightside ionosphere of Mars: Composition, vertical structure, and variability. *Journal of Geophysical Research: Space Physics*, *122*(4), 2016JA023508. https://doi.org/10.1002/2016JA023508

Gnevyshev, M. N., & Ohl, A. I. (1948). On the 22-year cycle of solar activity. *Astron. Zh*, *25*(1), 18.

Goldberg, D. E., & Holland, J. H. (1988). Genetic Algorithms and Machine Learning. *Machine Learning*, *3*, 5.

Greicius, T. (2015). Mars Exploration Past Missions.

Gurnett, D. A., Huff, R. L., Morgan, D. D., Persoon, A. M., Averkamp, T. F., Kirchner, D. L., Duru, F., Akalin, F., Kopf, A. J., Nielsen, E., Safaeinili, A., Plaut, J. J., & Picardi, G. (2008). An overview of radar soundings of the martian ionosphere from the Mars Express spacecraft [WOS:000255568400001]. *Advances in Space Research*, *41*(9), 1335–1346. https://doi.org/10.1016/j.asr.2007.01.062

Halekas, J. S., Brain, D. A., Luhmann, J. G., DiBraccio, G. A., Ruhunusiri, S., Harada, Y., Fowler, C. M., Mitchell, D. L., Connerney, J. E. P., Espley, J. R., Mazelle, C., & Jakosky, B. M. (2017). Flows, Fields, and Forces in the Mars-Solar Wind Interaction [_eprint: https://agupubs.onlinelibrary.wiley.com/doi/pdf/10.1002/2017JA024772]. *Journal of Geophysical Research: Space Physics*, *122*(11), 11, 320–11, 341. https://doi.org/10.1002/2017JA024772

Halekas, J. S., Lillis, R. J., Mitchell, D. L., Cravens, T. E., Mazelle, C., Connerney, J. E. P., Espley, J. R., Mahaffy, P. R., Benna, M., Jakosky, B. M., Luhmann, J. G., McFadden, J. P., Larson, D. E., Harada, Y., & Ruhunusiri, S. (2015). MAVEN observations of solar wind hydrogen deposition in the atmosphere of Mars: HYDROGEN DEPOSITION AT MARS. *Geophysical Research Letters*, *42*(21), 8901–8909. https://doi.org/10.1002/2015GL064693

Halekas, J. S., Ruhunusiri, S., Harada, Y., Collinson, G., Mitchell, D. L., Mazelle, C., McFadden, J. P., Connerney, J. E. P., Espley, J. R., Eparvier, F., Luhmann, J. G., & Jakosky, B. M. (2017). Structure, dynamics, and seasonal variability of the Mars-solar wind interaction: MAVEN Solar Wind Ion Analyzer in-flight performance and science results. *Journal of Geophysical Research: Space Physics*, *122*(1), 547–578. https://doi.org/10.1002/2016JA023167

Hall, B. E. S., Sanchez-Cano, B., Wild, J. A., Lester, M., & Holmstrom, M. (2019). The Martian Bow Shock Over Solar Cycle 23-24 as Observed by the Mars Express Mission [Place: Washington Publisher: Amer Geophysical Union WOS:000477723100059]. *Journal of Geophysical Research-Space Physics*, *124*(6), 4761–4772. https://doi.org/10.1029/2018JA026404

Harada, Y., Halekas, J. S., McFadden, J. P., Espley, J., DiBraccio, G. A., Mitchell, D. L., Mazelle, C., Brain, D. A., Andersson, L., Ma, Y. J., Larson, D. E., Xu, S., Hara, T., Ruhunusiri, S., Livi, R., & Jakosky, B. M. (2017). Survey of magnetic reconnection signatures in the Martian magnetotail with MAVEN. *Journal of Geophysical Research: Space Physics*, *122*(5), 2017JA023952. https://doi.org/10.1002/2017JA023952

Hathaway, D. H., Wilson, R. M., & Reichmann, E. J. (2002). Group Sunspot Numbers: Sunspot Cycle Characteristics. *Solar Physics*, *211*(1), 357–370. https://doi.org/10.1023/A:1022425402664

Heber, B., Sanderson, T. R., & Zhang, M. (1999). Corotating interaction regions. *Advances in Space Research*, *23*(3), 567–579. https://doi.org/10.1016/S0273-1177(99)80013-1

Huang, W., Nakamori, Y., & Wang, S. Y. (2005). Forecasting stock market movement direction with support vector machine [Place: Oxford Publisher: Pergamon-Elsevier Science Ltd WOS:000228207700003]. *Computers & Operations Research*, *32*(10), 2513–2522. https://doi.org/10.1016/j.cor.2004.03.016

Huddleston, D. E., Johnstone, A. D., & Coates, A. J. (1990). Determination of comet Halley Gas emission characteristics from mass loading of the solar wind [_eprint: https://onlinelibrary.wiley.com/doi/pdf/10.1029/JA095iA01p00021]. *Journal of Geophysical Research: Space Physics*, *95*(A1), 21–30. https://doi.org/10.1029/JA095iA01p00021

Hüllermeier, E., & Waegeman, W. (2021). Aleatoric and epistemic uncertainty in machine learning: An introduction to concepts and methods. *Machine Learning*, *110*(3), 457–506. https://doi.org/10.1007/s10994-021-05946-3

Intriligator, D. S. (1980). Transient Phenomena Originating at the Sun — An Interplanetary View. In M. Dryer & E. Tandberg-Hanssen (Eds.), *Solar and Interplanetary Dynamics* (pp. 357–374). Springer Netherlands. https://doi.org/10.1007/978-94-009-9100-2_57

Jakosky, B. M., Lin, R. P., Grebowsky, J. M., Luhmann, J. G., Mitchell, D. F., Beutelschies, G., Priser, T., Acuna, M., Andersson, L., Baird, D., Baker, D., Bartlett, R., Benna, M., Bougher, S., Brain, D., Carson, D., Cauffman, S., Chamberlin, P., Chaufray, J.-Y., . . . Zurek, R. (2015). The Mars Atmosphere and Volatile Evolution (MAVEN) Mission [WOS:000365729700002]. *Space Science Reviews*, *195*(1-4), 3–48. https://doi.org/10.1007/s11214-015-0139-x

Jarvinen, R., Brain, D. A., & Luhmann, J. G. (2016). Dynamics of planetary ions in the induced magnetospheres of Venus and Mars. *Planetary and Space Science*, *127*, 1–14. https://doi.org/10.1016/j.pss.2015.08.012

Jung, S.-M., Park, S., Jung, S.-W., & Hwang, E. (2020). Monthly Electric Load Forecasting Using Transfer Learning for Smart Cities [Number: 16 Publisher: Multidisciplinary Digital Publishing Institute]. *Sustainability*, *12*(16), 6364. https://doi.org/10.3390/su12166364

Kallio, E., & Barabash, S. (2012). Magnetized Mars: Spatial distribution of oxygen ions [Number: 2 Publisher: SpringerOpen]. *Earth, Planets and Space*, *64*(2), 149–156. https://doi.org/10.5047/eps.2011.07.008

Kashinath, K., Mustafa, M., Albert, A., Wu, J.-L., Jiang, C., Esmaeilzadeh, S., Azizzadenesheli, K., Wang, R., Chattopadhyay, A., Singh, A., Manepalli, A., Chirila, D., Yu, R., Walters, R., White, B., Xiao, H., Tchelepi, H. A., Marcus, P., Anandkumar, A., ... Prabhat, n. (2021). Physics-informed machine learning: Case studies for weather and climate modelling [Publisher: Royal Society]. *Philosophical Transactions of the Royal Society A: Mathematical, Physical and Engineering Sciences*, *379*(2194), 20200093. https://doi.org/10.1098/rsta.2020.0093

Kingma, D. P., & Ba, L. J. (2015). Adam: A Method for Stochastic Optimization [Publisher: Ithaca, NYarXiv.org].

Kopf, A. J., Gurnett, D. A., DiBraccio, G. A., Morgan, D. D., & Halekas, J. S. (2017). The transient topside layer and associated current sheet in the ionosphere of Mars [WOS:000403912500049]. *Journal of Geophysical Research-Space Physics*, *122*(5), 5579–5590. https://doi.org/10.1002/2016JA023591

Krizhevsky, A., Sutskever, I., & Hinton, G. E. (2017). ImageNet Classification with Deep Convolutional Neural Networks [Place: New York Publisher: Assoc Computing Machinery WOS:000402555400026]. *Communications of the Acm*, *60*(6), 84–90. https://doi.org/10.1145/3065386

Krymskii, A. M., Breus, T. K., Ness, N. F., Hinson, D. P., & Bojkov, D. I. (2003). Effect of crustal magnetic fields on the near terminator ionosphere at Mars: Comparison of in situ magnetic field measurements with the data of radio science experiments on board Mars Global Surveyor [_eprint: https://onlinelibrary.wiley.com/doi/pdf/10.1029/2002 *Journal of Geophysical Research: Space Physics*, *108*(A12). https://doi.org/10.1029/2002JA009662

Kumar, D. T. S. (2020). Video based Traffic Forecasting using Convolution Neural Network Model and Transfer Learning Techniques. (03), 7.

Kwon, H.-H., Brown, C., & Lall, U. (2008). Climate informed flood frequency analysis and prediction in Montana using hierarchical Bayesian modeling

[_eprint: https://onlinelibrary.wiley.com/doi/pdf/10.1029/2007GL032220]. *Geophysical Research Letters*, *35*(5). https://doi.org/10.1029/2007GL032220

Larson, D. E., Lillis, R. J., Lee, C. O., Dunn, P. A., Hatch, K., Robinson, M., Glaser, D., Chen, J., Curtis, D., Tiu, C., Lin, R. P., Luhmann, J. G., & Jakosky, B. M. (2015). The MAVEN Solar Energetic Particle Investigation [Place: Dordrecht Publisher: Springer WOS:000365729700006]. *Space Science Reviews*, *195*(1-4), 153–172. https://doi.org/10.1007/s11214-015-0218-z

Lean, J. (1990). Evolution of the 155 day periodicity in sunspot areas during solar cycles 12 to 21. *The Astrophysical Journal*, *363*, 718–727. https://doi.org/10.1086/169378

LeCun, Y., Bengio, Y., & Hinton, G. (2015). Deep learning [Bandiera_abtest: a Cg_type: Nature Research Journals Number: 7553 Primary_atype: Reviews Publisher: Nature Publishing Group Subject_term: Computer science;Mathematics and computing Subject_term_id: computer-science;mathematics-and-computing]. *Nature*, *521*(7553), 436–444. https://doi.org/10.1038/nature14539

Ledvina, S. A., Brecht, S. H., Brain, D. A., & Jakosky, B. M. (2017). Ion escape rates from Mars: Results from hybrid simulations compared to MAVEN observations [_eprint: https://onlinelibrary.wiley.com/doi/pdf/10.1002/2016JA023521]. *Journal of Geophysical Research: Space Physics*, *122*(8), 8391–8408. https://doi.org/10.1002/2016JA023521

Lillis, R. J., Deighan, J., Fox, J. L., Bougher, S. W., Lee, Y., Combi, M. R., Cravens, T. E., Rahmati, A., Mahaffy, P. R., Benna, M., Elrod, M. K., McFadden, J. P., Ergun, R. E., Andersson, L., Fowler, C. M., Jakosky, B. M., Thiemann, E., Eparvier, F., Halekas, J. S., ... Chaufray, J.-Y. (2017). Photochemical escape of oxygen from Mars: First results from MAVEN in situ data [_eprint: https://onlinelibrary.wiley.com/doi/pdf/10.1002/2016JA023525]. *Journal of Geophysical Research: Space Physics*, *122*(3), 3815–3836. https://doi.org/10.1002/2016JA023525

Liu, D., Rong, Z., Gao, J., He, J., Klinger, L., Dunlop, M., Yan, L., Fan, K., & Wei, Y. (2021). Statistical Properties of Solar Wind Upstream of Mars: MAVEN Observations. *The Astrophysical Journal*, *911*, 113. https://doi.org/10.3847/1538-4357/abed50

Liu, K., Hao, X., Li, Y., Zhang, T., Pan, Z., Chen, M., Hu, X., Li, X., Shen, C., & Wang, Y. (2020). Mars Orbiter magnetometer of China's First Mars Mission Tianwen-1 [Publisher: Science China Press]. *Earth and Planetary Physics*, *4*(4), 384–389. https://doi.org/10.26464/epp2020058

Luhmann, J. G., & Schwingenschuh, K. (1990). A model of the energetic ion environment of Mars [_eprint: https://onlinelibrary.wiley.com/doi/pdf/10.1029/JA095iA02p00939]. *Journal of Geophysical Research: Space Physics*, *95*(A2), 939–945. https://doi.org/10.1029/JA095iA02p00939

Luhmann, J., & Brace, L. (1991). Near-Mars Space [WOS:A1991FL55900001]. *Reviews of Geophysics*, *29*(2), 121–140. https://doi.org/10.1029/91RG00066

Luhmann, J., Russell, C., Schwingenschuh, K., & Yeroshenko, Y. (1991). A Comparison of Induced Magnetotails of Planetary Bodies - Venus, Mars, and Titan [WOS:A1991FW17100017]. *Journal of Geophysical Research-Space Physics*, *96*(A7), 11199–11208. https://doi.org/10.1029/91JA00086

Mahaffy, P. R., Benna, M., Elrod, M., Yelle, R. V., Bougher, S. W., Stone, S. W., & Jakosky, B. M. (2015). Structure and composition of the neutral upper atmosphere of Mars from the MAVEN NGIMS investigation [WOS:000368336800020]. *Geophysical Research Letters*, *42*(21), 8951–8957. https://doi.org/10.1002/2015GL065329

Mahaffy, P. R., Benna, M., King, T., Harpold, D. N., Arvey, R., Barciniak, M., Bendt, M., Carrigan, D., Errigo, T., Holmes, V., Johnson, C. S., Kellogg, J., Kimvilakani, P., Lefavor, M., Hengemihle, J., Jaeger, F., Lyness, E., Maurer, J., Melak, A., ... Nolan, J. T. (2015). The Neutral Gas and Ion Mass Spectrometer on the Mars Atmosphere and Volatile Evolution Mission [Place: Dordrecht Publisher: Springer WOS:000365729700003]. *Space Science Reviews*, *195*(1-4), 49–73. https://doi.org/10.1007/s11214-014-0091-1

Marquette, M. L., Lillis, R. J., Halekas, J. S., Luhmann, J. G., Gruesbeck, J. R., & Espley, J. R. (2018). Autocorrelation Study of Solar Wind Plasma and IMF Properties as Measured by the MAVEN Spacecraft. *Journal of Geophysical Research: Space Physics*, *123*(4), 2493–2512. https://doi.org/10.1002/2018JA025209

McClintock, W. E., Schneider, N. M., Holsclaw, G. M., Clarke, J. T., Hoskins, A. C., Stewart, I., Montmessin, F., Yelle, R. V., & Deighan, J. (2015). The Imaging Ultraviolet Spectrograph (IUVS) for the MAVEN Mission [Place: Dordrecht Publisher: Springer WOS:000365729700004]. *Space Science Reviews*, *195*(1-4), 75–124. https://doi.org/10.1007/s11214-014-0098-7

McFadden, J. P., Kortmann, O., Curtis, D., Dalton, G., Johnson, G., Abiad, R., Sterling, R., Hatch, K., Berg, P., Tiu, C., Gordon, D., Heavner, S., Robinson, M., Marckwordt, M., Lin, R., & Jakosky, B. (2015). MAVEN SupraThermal and Thermal Ion Compostion (STATIC) Instrument [Place: Dordrecht Publisher: Springer WOS:000365729700008]. *Space Science Reviews*, *195*(1-4), 199–256. https://doi.org/10.1007/s11214-015-0175-6

Mitchell, D. L., Lillis, R. J., Lin, R. P., Connerney, J. E. P., & Acuña, M. H. (2007). A global map of Mars' crustal magnetic field based on electron reflectometry [_eprint: https://onlinelibrary.wiley.com/doi/pdf/10.1029/2005JE002564]. *Journal of Geophysical Research: Planets*, *112*(E1). https://doi.org/10.1029/2005JE002564

Mitchell, D. L., Lin, R. P., Mazelle, C., Rème, H., Cloutier, P. A., Connerney, J. E. P., Acuña, M. H., & Ness, N. F. (2001). Probing Mars' crustal magnetic field and ionosphere with the MGS Electron Reflectometer [_eprint: https://onlinelibrary.wiley.com/doi/pdf/10.1029/2000JE001435]. *Journal of Geophysical Research: Planets*, *106*(E10), 23419–23427. https://doi.org/10.1029/2000JE001435

Mitchell, D. L., Mazelle, C., Sauvaud, J.-A., Thocaven, J.-J., Rouzaud, J., Fedorov, A., Rouger, P., Toublanc, D., Taylor, E., Gordon, D., Robinson, M., Heavner, S., Turin, P., Diaz-Aguado, M., Curtis, D. W., Lin, R. P., & Jakosky, B. M. (2016). The MAVEN Solar Wind Electron Analyzer [Place: Dordrecht Publisher: Springer WOS:000376077700009]. *Space Science Reviews*, *200*(1-4), 495–528. https://doi.org/10.1007/s11214-015-0232-1

Modolo, R., Chanteur, G. M., Dubinin, E., & Matthews, A. P. (2005). Influence of the solar EUV flux on the Martian plasma environment. *Annales Geophysicae*, *23*(2), 433–444. https://doi.org/https://doi.org/10.5194/angeo-23-433-2005

Nagy, A. F., Winterhalter, D., Sauer, K., Cravens, T. E., Brecht, S., Mazelle, C., Crider, D., Kallio, E., Zakharov, A., Dubinin, E., Verigin, M., Kotova, G., Axford, W. I., Bertucci, C., & Trotignon, J. G. (2004). The plasma environment of Mars [WOS:000222233800002]. *Space Science Reviews*, *111*(1-2), 33–114. https://doi.org/10.1023/B:SPAC.0000032718.47512.92

Najib, D., Nagy, A. F., Tóth, G., & Ma, Y. (2011). Three-dimensional, multifluid, high spatial resolution MHD model studies of the solar wind interaction with Mars [_eprint: https://onlinelibrary.wiley.com/doi/pdf/10.1029/2010JA016272]. *Journal of Geophysical Research: Space Physics*, *116*(A5). https://doi.org/10.1029/2010JA016272

Němeček, Z., Ďurovcová, T., Šafránková, J., Richardson, J. D., Šimůnek, J., & Stevens, M. L. (2020). (Non)radial Solar Wind Propagation through the Heliosphere [Publisher: The American Astronomical Society]. *The Astrophysical Journal Letters*, *897*(2), L39. https://doi.org/10.3847/2041-8213/ab9ff7

Neugebauer, M., & Snyder, C. W. (1966). Mariner 2 observations of the solar wind: 1. Average properties [_eprint: https://onlinelibrary.wiley.com/doi/pdf/10.1029/JZ071i019p04469 *Journal of Geophysical Research (1896-1977)*, *71*(19), 4469–4484. https://doi.org/10.1029/JZ071i019p04469

Nishizuka, N., Kubo, Y., Sugiura, K., Den, M., & Ishii, M. (2021). Operational solar flare prediction model using Deep Flare Net. *Earth, Planets and Space*, *73*(1), 64. https://doi.org/10.1186/s40623-021-01381-9

Noé, F., Tkatchenko, A., Müller, K.-R., & Clementi, C. (2020). Machine Learning for Molecular Simulation [_eprint: https://doi.org/10.1146/annurev-physchem-042018-052331]. *Annual Review of Physical Chemistry*, *71*(1), 361–390. https://doi.org/10.1146/annurev-physchem-042018-052331

Parish, H. F., Schubert, G., Hickey, M. P., & Walterscheid, R. L. (2009). Propagation of tropospheric gravity waves into the upper atmosphere of Mars [Num Pages: 10 Place: San Diego Publisher: Academic Press Inc Elsevier Science Web of Science ID: WOS:000277902900004]. *ICARUS*, *203*(1), 28–37. https://doi.org/10.1016/j.icarus.2009.04.031

Parker, E. (1958). Dynamics of the Interplanetary Gas and Magnetic Fields [WOS:A1958WC90100017] *Astrophysical Journal*, *128*(3), 664–676. https://doi.org/10.1086/146579

Patzold, M., Tellman, S., Hausler, B., Hinson, D., Schaa, R., & Tyler, G. L. (2005). A sporadic third layer in the ionosphere of Mars [WOS:000233121800040]. *Science*, *310*(5749), 837–839. https://doi.org/10.1126/science.1117755

Peter, K., Pätzold, M., Molina-Cuberos, G. J., González-Galindo, F., Witasse, O., Tellmann, S., Häusler, B., & Bird, M. K. (2021). The lower dayside ionosphere of Mars from 14 years of MaRS radio science observations. *Icarus*, *359*, 114213. https://doi.org/10.1016/j.icarus.2020.114213

Puh, M., & Brkic, L. (2019). *Detecting Credit Card Fraud Using Selected Machine Learning Algorithms* (M. Koricic, Z. Butkovic, K. Skala, Z. Car, M. CicinSain, S. Babic, V. Sruk, D. Skvorc, S. Ribaric, S. Gros, B. Vrdoljak, M. Mauher, E. Tijan, P. Pale, D. Huljenic, T. G. Grbac, & M. Janjic, Eds.) [Pages: 1250-1255 Publication Title: 2019 42nd International Convention on Information and Communication Technology, Electronics and Microelectronics (mipro) WOS:000484544500223]. Ieee.

Rahmati, A., Larson, D. E., Cravens, T. E., Lillis, R. J., Halekas, J. S., McFadden, J. P., Mitchell, D. L., Thiemann, E. M. B., Connerney, J. E. P., Dunn, P. A., Lee, C. O., Eparvier, F. G., DiBraccio, G. A., Espley, J. R., Luhmann, J. G., Mazelle, C., & Jakosky, B. M. (2018). Seasonal Variability of Neutral Escape from Mars as Derived From MAVEN Pickup Ion Observations. *Journal of Geophysical Research: Planets*, *123*(5), 1192–1202. https://doi.org/10.1029/2018JE005560

Rickett, B. J., & Coles, W. A. (1991). Evolution of the solar wind structure over a solar cycle: Interplanetary scintillation velocity measurements compared with coronal observations [_eprint: https://onlinelibrary.wiley.com/doi/pdf/10.1029/90JA01528]. *Journal of Geophysical Research: Space Physics*, *96*(A2), 1717–1736. https://doi.org/10.1029/90JA01528

Romanelli, N., Bertucci, C., Gómez, D., & Mazelle, C. (2015). Dependence of the location of the Martian magnetic lobes on the interplanetary magnetic field direction: Observations from Mars Global Surveyor. *Journal of Geophysical Research: Space Physics*, *120*(9), 7737–7747. https://doi.org/10.1002/2015JA021359

Romanelli, N., Mazelle, C., Chaufray, J. Y., Meziane, K., Shan, L., Ruhunusiri, S., Connerney, J. E. P., Espley, J. R., Eparvier, F., Thiemann, E., Halekas, J. S.,

Mitchell, D. L., McFadden, J. P., Brain, D., & Jakosky, B. M. (2016). Proton cyclotron waves occurrence rate upstream from Mars observed by MAVEN: Associated variability of the Martian upper atmosphere [_eprint: https://onlinelibrary.wiley.com/doi/pdf/10.1002/2016JA023270]. *Journal of Geophysical Research: Space Physics*, *121*(11), 11, 113–11, 128. https://doi.org/10.1002/2016JA023270

Romanelli, N., Modolo, R., Leblanc, F., Chaufray, J.-Y., Hess, S., Brain, D., Connerney, J., Halekas, J., Mcfadden, J., & Jakosky, B. (2018). Effects of the Crustal Magnetic Fields and Changes in the IMF Orientation on the Magnetosphere of Mars: MAVEN Observations and LatHyS Results. *Journal of Geophysical Research: Space Physics*, *123*(7), 5315–5333. https://doi.org/10.1029/2017JA025155

Ruhunusiri, S., Halekas, J. S., Espley, J. R., Eparvier, F., Brain, D., Mazelle, C., Harada, Y., DiBraccio, G. A., Dong, Y., Ma, Y., Thiemann, E. M. B., Mitchell, D. L., & Jakosky, B. M. (2018). An Artificial Neural Network for Inferring Solar Wind Proxies at Mars. *Geophysical Research Letters*, *45*(20), 10, 855–10, 865. https://doi.org/10.1029/2018GL079282

Samuel, A. L. (1959). Some Studies in Machine Learning Using the Game of Checkers [Conference Name: IBM Journal of Research and Development]. *IBM Journal of Research and Development*, *3*(3), 210–229. https://doi.org/10.1147/rd.33.0210

Shah, B., & Bhavsar, H. (2022). Time Complexity in Deep Learning Models. *Procedia Computer Science*, *215*, 202–210. https://doi.org/10.1016/j.procs.2022.12.023

Shallue, C. J., & Vanderburg, A. (2018). Identifying Exoplanets with Deep Learning: A Five-planet Resonant Chain around Kepler-80 and an Eighth Planet around Kepler-90 [Publisher: American Astronomical Society]. *The Astronomical Journal*, *155*(2), 94. https://doi.org/10.3847/1538-3881/aa9e09

Shane, A. D., Xu, S., Liemohn, M. W., & Mitchell, D. L. (2016). Mars nightside electrons over strong crustal fields. *Journal of Geophysical Research: Space Physics*, *121*(4), 3808–3823. https://doi.org/10.1002/2015JA021947

Siddlea, A. G., Mueller-Wodarg, I. C. F., Stone, S. W., & Yelle, R. (2019). Global characteristics of gravity waves in the upper atmosphere of Mars as measured by MAVEN/NGIMS [Num Pages: 10 Place: San Diego Publisher: Academic Press

Inc Elsevier Science Web of Science ID: WOS:000481566200002]. *ICARUS*, *333*, 12–21. https://doi.org/10.1016/j.icarus.2019.05.021

Singh, S. A., Meitei, T. G., & Majumder, S. (2020). 6 - Short PCG classification based on deep learning. In B. Agarwal, V. E. Balas, L. C. Jain, R. C. Poonia, & Manisha (Eds.), *Deep Learning Techniques for Biomedical and Health Informatics* (pp. 141–164). Academic Press. https://doi.org/10.1016/B978-0-12-819061-6.00006-9

Smith, D. E., Zuber, M. T., Frey, H. V., Garvin, J. B., Head, J. W., Muhleman, D. O., Pettengill, G. H., Phillips, R. J., Solomon, S. C., Zwally, H. J., Banerdt, W. B., Duxbury, T. C., Golombek, M. P., Lemoine, F. G., Neumann, G. A., Rowlands, D. D., Aharonson, O., Ford, P. G., Ivanov, A. B., ... Sun, X. (2001). Mars Orbiter Laser Altimeter: Experiment summary after the first year of global mapping of Mars [_eprint: https://onlinelibrary.wiley.com/doi/pdf/10.1029/2000JE001364]. *Journal of Geophysical Research: Planets*, *106*(E10), 23689–23722. https://doi.org/10.1029/2000JE001364

Song, Y., Zhang, L., & Giles, C. L. (2011). Automatic tag recommendation algorithms for social recommender systems. *ACM Transactions on the Web*, *5*(1), 4:1–4:31. https://doi.org/10.1145/1921591.1921595

Stone, S. W., Yelle, R. V., Benna, M., Elrod, M. K., & Mahaffy, P. R. (2018). Thermal Structure of the Martian Upper Atmosphere From MAVEN NGIMS [Publisher: John Wiley & Sons, Ltd]. *Journal of Geophysical Research: Planets*, *123*(11), 2842–2867. https://doi.org/10.1029/2018JE005559

Sullivan, W. (1965). FIRST MARS PHOTO IS TRANSMITTED; MARINER SIGNALS INDICATE PLANET LACKS A LIQUID CORE LIKE EARTH'S; OTHER DATA SENT. *The New York Times*.

Sutton, R. S., & Barto, A. G. (2018). *Reinforcement Learning: An Introduction, 2nd Edition* [Pages: 1-526 Publication Title: Reinforcement Learning: An Introduction, 2nd Edition WOS:000481873900019]. Mit Press.

Tao, C., Kataoka, R., Fukunishi, H., Takahashi, Y., & Yokoyama, T. (2005). Magnetic field variations in the Jovian magnetotail induced by solar wind dynamic pressure enhancements [_eprint: https://onlinelibrary.wiley.com/doi/pdf/10.1029/2004JA010959].

Journal of Geophysical Research: Space Physics, *110*(A11). https://doi.org/10.1029/2004JA010959

Trainer, M. G., Wong, M. H., McConnochie, T. H., Franz, H. B., Atreya, S. K., Conrad, P. G., Lefèvre, F., Mahaffy, P. R., Malespin, C. A., Manning, H. L., Martín-Torres, J., Martínez, G. M., McKay, C. P., Navarro-González, R., Vicente-Retortillo, Á., Webster, C. R., & Zorzano, M.-P. (2019). Seasonal Variations in Atmospheric Composition as Measured in Gale Crater, Mars [_eprint: https://onlinelibrary.wiley.com/doi/pdf/10.1029/2019JE006175]. *Journal of Geophysical Research: Planets*, *124*(11), 3000–3024. https://doi.org/10.1029/2019JE006175

Ulrich, R. K., & Tran, T. (2013). THE GLOBAL SOLAR MAGNETIC FIELD—IDENTIFICATION OF TRAVELING, LONG-LIVED RIPPLES [Publisher: American Astronomical Society]. *The Astrophysical Journal*, *768*(2), 189. https://doi.org/10.1088/0004-637X/768/2/189

Vignes, D., Mazelle, C., Rme, H., Acuña, M. H., Connerney, J. E. P., Lin, R. P., Mitchell, D. L., Cloutier, P., Crider, D. H., & Ness, N. F. (2000). The solar wind interaction with Mars: Locations and shapes of the bow shock and the magnetic pile-up boundary from the observations of the MAG/ER Experiment onboard Mars Global Surveyor. *Geophysical Research Letters*, *27*(1), 49–52. https://doi.org/10.1029/1999GL010703

Volwerk, M., Richter, I., Tsurutani, B., Götz, C., Altwegg, K., Broiles, T., Burch, J., Carr, C., Cupido, E., Delva, M., Dósa, M., Edberg, N. J. T., Eriksson, A., Henri, P., Koenders, C., Lebreton, J.-P., Mandt, K. E., Nilsson, H., Opitz, A., … Glassmeier, K.-H. (2016). Mass-loading, pile-up, and mirror-mode waves at comet 67P/Churyumov-Gerasimenko [Publisher: Copernicus GmbH]. *Annales Geophysicae*, *34*(1), 1–15. https://doi.org/10.5194/angeo-34-1-2016

Waldmann, I. P., & Griffith, C. A. (2019). Mapping Saturn using deep learning. *Nature Astronomy*, *3*(7), 620–625. https://doi.org/10.1038/s41550-019-0753-8

Wang, Y.-M., & N. R. Sheeley, J. (2003). On the Fluctuating Component of the Sun's Large-Scale Magnetic Field [Publisher: IOP Publishing]. *The Astrophysical Journal*, *590*(2), 1111. https://doi.org/10.1086/375026

Wernick, M. N., Yang, Y., Brankov, J. G., Yourganov, G., & Strother, S. C. (2010). Machine Learning in Medical Imaging [Place: Piscataway Publisher: Ieee-Inst Electrical Electronics Engineers Inc WOS:000278813700006]. *Ieee Signal Processing Magazine*, *27*(4), 25–38. https://doi.org/10.1109/MSP.2010.936730

Wilson, R. M. (1988). On the long-term secular increase in sunspot number. *Solar Physics*, *115*(2), 397–408. https://doi.org/10.1007/BF00148736

Withers, P. (2009). A review of observed variability in the dayside ionosphere of Mars [WOS:000268360900001]. *Advances in Space Research*, *44*(3), 277–307. https://doi.org/10.1016/j.asr.2009.04.027

Ye, R., & Dai, Q. (2018). A novel transfer learning framework for time series forecasting. *Knowledge-Based Systems*, *156*, 74–99. https://doi.org/10.1016/j.knosys.2018.05.021

Zhang, C., Zhang, Y., Gao, J., & Li, Y. (2020). SNR enhancement for the second harmonics in fluxgate sensor [Publisher: IOP Publishing]. *IOP Conference Series: Earth and Environmental Science*, *571*(1), 012122. https://doi.org/10.1088/1755-1315/571/1/012122

Zhang, M., Luhmann, J., Nagy, A., Spreiter, J., & Stahara, S. (1993). Oxygen Ionization Rates at Mars and Venus - Relative Contributions of Impact Ionization and Charge-Exchange [WOS:A1993KX58700019]. *Journal of Geophysical Research-Planets*, *98*(E2), 3311–3318. https://doi.org/10.1029/92JE02229

Zuber, M. T. (2001). The crust and mantle of Mars. *Nature*, *412*(6843), 220–227. https://doi.org/10.1038/35084163